

**University of Miami
Scholarly Repository**

Open Access Dissertations

Electronic Theses and Dissertations

2016-04-18

Material Dispersion by Ocean Eddies and Waves

Peng Wang

University of Miami, pwangum@gmail.com

Follow this and additional works at: http://scholarlyrepository.miami.edu/oa_dissertations

Recommended Citation

Wang, Peng, "Material Dispersion by Ocean Eddies and Waves" (2016). *Open Access Dissertations*. Paper 1653.

This Open access is brought to you for free and open access by the Electronic Theses and Dissertations at Scholarly Repository. It has been accepted for inclusion in Open Access Dissertations by an authorized administrator of Scholarly Repository. For more information, please contact repository.library@miami.edu.

UNIVERSITY OF MIAMI

MATERIAL DISPERSION BY OCEAN EDDIES AND WAVES

By
Peng Wang

A DISSERTATION

Submitted to the Faculty
of the University of Miami
in partial fulfillment of the requirements for
the degree of Doctor of Philosophy

Coral Gables, Florida
May 2016

©2016
Peng Wang
All Rights Reserved

UNIVERSITY OF MIAMI

A dissertation submitted in partial fulfillment of
the requirements for the degree of
Doctor of Philosophy

MATERIAL DISPERSION BY OCEAN EDDIES AND WAVES

Peng Wang

Approved:

Tamay M. Özgökmen, Ph.D.
Professor of Ocean Sciences

Igor Kamenkovich, Ph.D.
Associate Professor of Ocean Sciences

Mohamed Iskandarani, Ph.D.
Associate Professor of Ocean Sciences

Guillermo Prado, Ph.D.
Dean of the Graduate School

Larry J. Pratt, Ph.D.
Senior Scientist of Physical Oceanography
Woods Hole Oceanographic Institution
Woods Hole, Massachusetts

WANG, PENG
Material Dispersion by
Ocean Eddies and Waves

(Ph.D., Meteorology and Physical Oceanography)
(May 2016)

Abstract of a dissertation at the University of Miami.

Dissertation supervised by Professor Tamay M. Özgökmen.
No. of pages in text. (144)

Material dispersion in the ocean, such as the dispersion of natural and anthropogenic tracers (*e.g.* nutrients, dissolved gases, pollutants), is important in understanding processes at a variety of scales, ranging from plankton production to climate variability. Material dispersion is controlled by many dynamic processes; the present research focuses on the 3D material dispersion by ocean eddies and waves (inertial waves and internal gravity waves).

Ocean eddies may suffer various hydrodynamic instabilities, such as barotropic instability, inertial instability and 3D instability. In this work, I investigate how instabilities impact the 3D material dispersion by ocean eddies, using analytical methods and numerical simulations. I discover for the first time that material can be exchanged through 3D pathways which link a family of vortices generated by the instabilities of a single, initially unstable eddy. I also show that instabilities can increase the magnitude of vertical velocity and mixing rate. Besides, I find that instabilities can cause the kinetic energy wavenumber spectrum to have a power-law regime different with the classic regimes of $k^{-5/3}$ and k^{-3} , and propose a new energy spectrum to interpret the non-classic regime.

Inertial waves can arise in rotating homogeneous fluids. By numerically simulating an initially unstable eddy, I discover for the first time a special kind of inertial waves, which are emitted in a spiral manner from the eddies; I refer to these

waves as spiral inertial waves (SIWs). SIWs appear at small Rossby numbers ($0.01 \leq Ro \leq 1$) according to our parameter sweep experiments; the amplitude, wavelength and frequency of SIWs are sensitive to Rossby numbers. I extend the theory of Lighthill-Ford radiation into inertial waves, and propose an indicator for the emission of inertial waves; this indicator may be adopted into general circulation models to parameterize inertial waves. Additionally, when releasing passive tracers into the wave field, SIWs organize tracers into spirals, and modify the tracer's local rate of change by advecting tracers vertically. Further, the spirals of SIWs resemble some spiral features observed in the ocean and atmosphere, for example, spiral ocean eddies and spiral hurricane rainbands; thus, SIWs may offer another mechanism to form spiral eddies and rainbands. Since no density anomaly is required to generate the spirals of SIWs, I infer that the density anomaly, hence the baroclinic or frontal instability, is unlikely to be the key factor in the formation of these spiral features.

Internal gravity waves are ubiquitous in the ocean; they can transport nutrients, pollutants, sediments, *etc.* Using numerical simulations of internal waves that are initialized with the Garrett-Munk spectrum, I investigate the material dispersion by internal waves; the dispersion regimes are identified in terms of two metrics, the relative dispersion and finite-scale Lyapunov exponent (FSLE). The metric of relative dispersion reveals that dispersion regime by internal waves is between ballistic and diffusive regimes; while, the metric of FSLE indicates that the regime is ballistic. Besides, I show that internal waves below an upper mixed layer can generate flows in the mixed layer, leading to material dispersion. The dispersion produced by both internal waves and mixed layer eddies is also examined.

To my parents,
WANG Yuzhi and CHI Ruiqin.

Acknowledgments

I would like to express my sincere gratitude to many people who helped me to finish my dissertation and to accomplish my Ph.D.

First of all, I am very grateful to my advisor, Tamay M. Özgökmen, who gives me academic freedom as much as possible; hence, I can explore the scientific questions in which I am really interested. Tamay often encourages me, and affirms my merits; all his encouragements, patience and trust remarkably build my confidence in the Ph.D. study.

Meanwhile, I would like to extend my great thanks to my committee, Mohamed Iskandarani, Igor Kamenkovich and Larry J. Pratt. Mohamed's expertise on numerics helped me a lot in numerical simulations; Igor inspired me to explore the beautiful quasi-geostrophic fluid dynamics; Larry's brilliant model of rotating tank became the base model in my Ph.D. research; Larry wrote a nice paper published on *Journal of Fluid Mechanics* with me co-authored, becoming my first ever paper.

Also, I owe my gratitude to David S. Nolan and Angelique C. Haza. David guided me into the field of vortex dynamics, an amazing world of fluid dynamics; Angelique taught me her expertise on the dispersion of Lagrangian particles. Besides, I am glad that I am in a great research group (Gustavo M. Marques, Jean A. Mensa, Guillaume Novelli, Edward H. Ryan, etc.); our group meetings expanded my views in science, economics, human psychology, *etc.*

In the past four and half years, I was lucky to make many amazing friends and to experience different lives, such as fishing with Matt Onderlinde; swimming with Teddy Allen; snorkeling and tennis with Honghai Zhang; gardening with Kieran Bhatia; road trip with Jianhao Zhang, Jing Wang, Yue Pan, Chuntao Lu, Yemi Adebiyi, Xiaoqin Zang and Zhen Guo; camping with Shitao Wang and Xing Lv; ping pong with Jie He, Yi Dai, Ming Shao and Wei Zhang; badminton with Shuangyu Ge; board game with Greta Leber and Milan Curcic; hurricane monitoring with Falko Judt; tasting desserts made by Ajda Savarin; plentiful and generous help from Zhixuan Feng, Xiaoqin Zang, Andrés Rivera, Changhen Chen and Yan Wang making my living abroad much easier; *etc.* Needless to say, all of these friends and experiences have become an important part of my invaluable memory of Miami.

Last, I want to send my deepest gratitude to my parents, Yuzhi Wang and Ruiqin Chi, who are always there encouraging me; their patient listening, innermost understanding and unconditional care, endow me tremendous power to pursue my life goals. In particular, through my dad, I met a special girl, Fei Li, who brought a totally new feeling to me; since then, my happiest thing has been the chatting with her every morning, sharing the experiences of our daily life and witnessing the growth of ourselves. All in all, accompanied by the forever love from my family, I am moving forward to my goals, closer and closer!

This research is supported by the Multidisciplinary University Research Initiatives (MURI) program, which is sponsored by the U.S. Department of Defense; the MURI grant (*N000141110087*) is administered by the Office of Naval Research.

Contents

List of Figures	viii
List of Tables	xvi
1 Introduction	1
1.1 Instabilities of geophysical vortices	2
1.2 Inertial waves	5
1.3 Dispersion regimes in Lagrangian framework	6
1.4 Scientific questions	9
2 Unstable ocean eddies	12
2.1 Overview	12
2.2 Numerical model	12
2.3 Analysis of instabilities	18
2.3.1 Barotropic instability	18
2.3.2 Inertial instability	22
2.3.3 Three-dimensional instability	26
2.4 Joint impacts of instabilities on transport	31
2.4.1 Evolution of an unstable vortex	31
2.4.2 Overturning transport by the secondary circulation	32
2.4.3 Rates of the vertical exchange and mixing	40

2.4.4	A new thinking on the energy transfer	43
2.5	Discussion	48
2.5.1	Linear instability analysis of geophysical vortices	48
2.5.2	Nonlinear evolution and transport in geophysical vortices . . .	51
3	Spiral inertial waves	56
3.1	Overview	56
3.2	Numerical model	57
3.3	Results	61
3.3.1	Emission of SIWs	61
3.3.2	Dependence of SIWs on Rossby number	71
3.3.3	Source of SIWs	77
3.3.4	Effects of SIWs on material dispersion	85
3.4	Discussion	89
4	Lagrangian dispersion by ocean internal gravity waves	98
4.1	Overview	98
4.2	Method	99
4.2.1	Numerical model	99
4.2.2	Initialization of Garrett-Munk internal waves	100
4.3	Analysis of material dispersion	104
4.3.1	Experiment with linear stratification (Exp.-1)	108
4.3.2	Experiment with mixed layer (Exp.-2)	115
4.3.3	Experiment with front in mixed layer (Exp.-3)	119
5	Conclusions	126
References		131

List of Figures

2.1	The cylindrical domain of numerical experiments.	14
2.2	(a) Initial velocity profiles of the control and target experiments. Initial vorticity fields at mid-depth horizontal plane in (b) the target experiment and (c) the control experiment.	16
2.3	An example of the numerical convergence check (from the target experiment T1). N is the order of Legendre polynomials for numerical solutions.	17
2.4	Contours of normalized growth rates in $\delta-\varepsilon$ space for different azimuthal wavenumber m and length ratio F ; left column: $m = 1$, right column: $m = 2, 3, 4$; (a, b) $F = 0.5$, (c, d) $F = 1$, (e, f) $F = 2$. Closed regions have nonzero growth rate; contours in the right column depict level 0.001.	23
2.5	Vertical vorticity at mid-depth horizontal plane from the target experiment T2, showing the asymmetric effect of azimuthal wavenumber-1 instability that shifts the central vortex off center, towards one of the two satellite vortices.	24
2.6	The generation of toroidal/rib vortices by inertial instability from the target experiment T4, visualized by the isosurface of vertical vorticity equal to -1 at (a) time = 0 and (b) time = 8.	27

2.7	Growth rates of 3D instability for different azimuthal and vertical wavenumber pairs (m, k).	29
2.8	The helical structure of 3D instability from the target experiment T1, visualized by the isosurface of vertical vorticity equal to 1.	31
2.9	Vertical vorticity field at mid-depth horizontal plane in the target experiment T1 at (a) time = 17 (b) time = 19 (c) time = 65 and (d) time = 195.	33
2.10	3D structures of vortices, visualized by the isosurface of vertical vorticity, correspond to the vortex shown in (a) Fig. 2.9b and (b) Fig. 2.9d.	34
2.11	(a, b) Vertical velocity fields and (c, d) horizontal velocity vectors at mid-depth horizontal plane at time = 195; color denotes the magnitude of velocity; left column: the control experiment C1; right column: the target experiment T1.	35
2.12	Tracer evolution in the control experiment C1, visualized by the tracer isosurface of 0.0006 at (a) time = 0 (b) time = 76 (c) time = 95 and (d) time = 399. A particle trajectory is imposed on (b)–(d) with the blue sphere denoting the initial position of the particle. (Readers may refer to the animation at http://youtu.be/qm7i0bVv41s .)	36
2.13	Tracer evolution in the target experiment T1, visualized by the tracer isosurface of 0.0006 at (a) time = 0 (b) time = 65 (c) time = 90 (d) time = 116 (e) time = 256 and (f) time = 399. Similar to Fig. 2.12, a particle trajectory is imposed on (b)–(f), too. (Readers may refer to the animation at http://youtu.be/ZJYpLcSLGSc .)	38

2.14 Streamlines over a horizontal slice of the vertical vorticity field at mid depth in (a) the control experiment C1 and (b) the target experiment T1 at time = 195. Two sets of streamline are coloured by white and black. Positive (negative) vorticity is coloured by red (blue).	39
2.15 (a) FTLE field at mid-depth horizontal plane in the target experiment T1 at time = 195, with trajectories of 1,283,202 particles being integrated for a period of 80 (forward-in-time). (b) Okubo-Weiss field at mid-depth horizontal plane in the target experiment T1 at time = 195.	40
2.16 Evolution of the RMS vertical velocity in the control experiment C1 and target experiment T1.	41
2.17 Vertical gradients of the vertical tracer flux across mid-depth horizontal plane at (a, b) time = 65 and (c, d) time = 195; left column: the control experiment C1; right column: the target experiment T1.	42
2.18 (a) Evolution of the domain-averaged tracer field with mixing rate Γ being labelled; (b) evolution of the RMS gradient of tracer fields. The period of instability growth is labelled.	44
2.19 Evolution of the domain-averaged tracer field with mixing rate Γ being labelled for the (a) higher diffusivity, $Pe = 10^4$ and (b) lower diffusivity, $Pe = 10^6$. The period of instability growth is labelled. (Note the different scaling of the panels.)	45
2.20 Kinetic energy wavenumber spectrum at the initial and final state of the flow in (a) the control experiment C1 and (b) the target experiment T1.	46

2.21 Kinetic energy wavenumber spectrum at the final state of the flow in the target experiment T3.	47
2.22 (a) Temperature field and (b) pressure field at the surface in the target experiment T1 at time = 195.	51
3.1 The cylindrical domain used in the numerical experiments.	58
3.2 Azimuthal velocity profiles of the initial vortex.	59
3.3 The evolutions of kinetic energy of Exp. T1 with different mesh resolutions and Reynolds numbers.	61
3.4 Vertical vorticity fields (left column) and vertical velocity fields (right column) from Exp. T1 (initially cyclonic); both fields are plotted at mid-depth horizontal plane at (a, b) time = 6; (c, d) time = 30 and (e, f) time = 204. (The https://youtu.be/Vw564T17pk4 links the wave animation.)	64
3.5 Vertical velocity along the circle of radius $r = 2.5$ at the mid-depth in Exp. T1. (a) SIW-4 phase at time = 30 and (b) SIW-2 phase at time = 204 (dashed lines outlining the wave envelope).	65
3.6 (a) Hovmöller diagram of vertical velocity on mid-depth horizontal plane, shown in the radius–time section. (b) and (c) show the zoom-in views of regions denoted by the boxes in (a), for phases SIW-4 and SIW-2, respectively. The blue arrows show the direction of phase speed and the red arrows point the direction of group velocity.	67
3.7 Upper panel: vertical velocity fields at the mid-depth horizontal plane, from Exp. T9, at (a) time = 30 and (b) time = 204. Lower panel: the corresponding vertical velocity along the circle of radius $r = 6$ for phase (c) SIW-4 and (d) SIW-2 (dashed lines outlining the wave envelope).	68

3.8	Vertical vorticity fields (left column) and vertical velocity fields (right column) from Exp. T10; both fields are plotted at mid-depth horizontal plane at (a, b) time = 6; (c, d) time = 26 and (e, f) time = 205.	69
3.9	Vertical vorticity fields (left column) and vertical velocity fields (right column) from Exp. C1; both fields are plotted at mid-depth horizontal plane at (a,b) time = 10 and (c, d) time = 296.	70
3.10	Phases SIW-4 and SIW-2 of (a,c) Exp. T11 and (b,d) Exp. T12 at the mid-depth horizontal plane. [The vertical velocities are sampled along the circle of radius = 2.5 to show the four complete waves and two wave packets; dashed lines represent wave envelopes.]	72
3.11	Snapshots of vertical vorticity fields (left column) and the corresponding vertical velocity fields (right column) at mid-depth horizontal plane for target experiments (a,b) T2; (c,d) T3; (e,f) T4; (g,h) T5; (i,j) T6; (k,l) T7; (m,n) T8. (Note the change of magnitude of vertical velocity.)	74
3.12	The change of (a) SIWs amplitude and (b) ratio Q with Rossby number. (Wave amplitudes are recorded at the final stage of vortex evolution.)	76
3.13	Wave source fields S in Exp. T1 (left column) at (a) time = 6, (c) time = 204; the fields in Exp. C1 (right column) at (b) time = 10, (d) time = 296, at mid-depth horizontal plane. (Note the change of magnitude of wave source.)	81
3.14	Snapshots of the wave source fields S in Exps. (a) T10 (b) T2 (c) T5 and (d) T7 at mid-depth horizontal plane. (The time stamps are the same to that of the corresponding wave fields shown in Figs. 3.8f, 3.11b, 3.11h and 3.11l, respectively.)	82

3.15 Frequency spectra of the wave source S inside the vortex in Exps. (a) T2 (b) T3 (c) T4 (d) T1 (e) T5 and (f) T8. (Note that the maximum frequency of inertial waves is 2 according to Eq. 3.4.)	84
3.16 The change of source intensity with Rossby number. (Source intensities are computed at the final stage of vortex evolution.)	85
3.17 Tracer fields at mid-depth horizontal plane in (a) Exp. T1 and (b) Exp. C1 at time = 30. (The central regions occupied by the vortices are clipped to emphasize the outside wave field.)	86
3.18 Snapshots of the vertical tracer advection by SIWs ($w \frac{\partial C}{\partial z}$), across mid-depth horizontal plane of (a,b) Exp. T1 and (c,d) Exp. T7; left column: $Pe = 10^4$, right column: $Pe = 10^5$. (The central regions occupied by the vortices are clipped to emphasize the outside wave field.)	87
3.19 (a) Initial positions of particle groups A,B,C at the wave field of Exp. T7. (b,c,d) Evolutions of the absolute dispersion of particle groups A,B,C, respectively.	88
3.20 Snapshots of the square of horizontal strain rate on mid-depth horizontal plane in Exps. (a) T7 (b) T4 (c) T3 and (d) T2.	92
3.21 Vertical velocity in the wave field on the (a) $\theta = 0$ and (b) $\theta = \pi/2$ section (θ is the angle coordinate of the cylindrical frame) at mid-depth in Exps. T1 and T10, at the final stage of vortex evolution.	96
4.1 The cylindrical domain used in the numerical experiments. (Vertically stretched image)	101
4.2 The frequency spectrum of the initial internal waves.	104

4.3	(a) Vertical profiles of the initial density field in Exp.-1 and Exp.-2. The 3D distribution of initial density field in (b) Exp.-1 with a linear stratification, (c) Exp.-2 with an upper mixed layer, and (d) Exp.-3 with a circular front inside the upper mixed layer.	105
4.4	Isosurface of density in (a) Exp.-1, (b) Exp.-2 and (c) Exp.-3 at one day after initialization.	107
4.5	(a) Particles released at three depths. (b) Particle distribution at each depth; the circle represents the domain boundary.	109
4.6	Positions of particles in Exp.-1 at 6.3 days after the release at mid-depth (1300 m), with (a) 2D view and (b) 3D view; also, positions of particles released at (c) upper layer (208 m) and (d) sub-surface (65 m) in 2D view.	110
4.7	Relative dispersion for Exp.-1: (a) at the middle fluid depth (log-log frame), five curves of relative dispersion is computed from five particle groups; the thick black curve is the average relative dispersion over all particle pairs of five groups. Average relative dispersion for each of three depths is shown in (b) semi-log frame and (c) log-log frame. The black thin line in (b) indicates the exponential regime of $D^2 \propto e^{12t}$. . .	112
4.8	FSLE curves in Exp.-1: (a) FSLE calculated using 3D-advection trajectories of the five particle groups at the middle fluid depth; the thick black curve is the average FSLE over the five groups. (b) Average FSLE at three depths, from 3D-advection particles trajectories. (c) Average FSLE at middle fluid depth, from particles trajectories advected by 3D full velocity, 2D horizontal velocity, and 1D vertical velocity.	114

4.9 Positions of particles in Exp.-2 at 7.4 days after the release at (a) mid-depth (1300 m), (b) pycnocline (208 m) and (c) mixed layer (65 m) in 2D view.	116
4.10 Relative dispersion in Exp.-2 at three depths in the (a) semi-log frame and (b) log-log frame, along with (c) FSLE curves at three depths in Exp.-2. Each curve in (a,b,c) represent the average over all the five particle groups released at the same depth.	118
4.11 Velocity magnitude at the surface in Exp.-3 at (a) 0.5 days and (b) 7.4 days. Density field at the surface at (c) 0.5 days and (d) 7.4 days.	120
4.12 Positions of particles in Exp.-3 at 7.4 days after the release at (a) mid-depth (1300 m), (b) pycnocline (208 m) and (c) mixed layer (65 m) in 2D view.	121
4.13 Relative dispersion from each particle group released (a) at the middle depth, with the black curve indicating the average over all the five groups (A-E), and (b) at the pycnocline, with the black curve representing the average over the four surrounding groups (B-E). Relative dispersion at the pycnocline in (c) semi-log frame and (d) log-log frame. Relative dispersion at the mixed layer in (e) semi-log frame and (f) log-log frame. In (c,d,e,f), the black thick curves represent the average of the four surrounding groups (B-E).	123
4.14 FSLE curves in Exp.-3: (a) At the mid-depth; the black curve represents the average over all the five groups (A-E). (b) At the pycnocline, and (c) at the mixed layer; the black curves in (b,c) represent the average over the four surrounding groups (B-E).	125

List of Tables

2.1	List of the target (T) and control (C) experiments. Note that the initial vortex in the target experiment T4 is anticyclonic, denoted by “–Eq. (2.3a)”; that is, its flow direction is opposite to that of the flow given by Eq. (2.3a).	17
3.1	List of the numerical experiments. The vortices initialized by Eq. (3.3a) and Eq. (3.3b) are designated as target (T) and control (C) experiments, respectively. The initial vortex in Exp. T10 is anticyclonic, denoted by –Eq. (3.3a).	60
3.2	List of the most energetic mode and frequency of SIWs.	77
4.1	Parameters used in the GM spectrum.	102
4.2	(Dimensionless) Internal wave kinetic energy at different depths, one day after initialization.	106
5.1	List of the major dispersion regimes in terms of relative dispersion ($D \propto e^{\gamma t}$ and $D^2 \propto t^\alpha$) for all the experiments. The stack of dispersion regimes indicates the regime transition from the top to bottom.	128
5.2	List of the major dispersion regimes in terms of FSLE ($\lambda \propto \delta^\beta$) for all the experiments. The stack of dispersion regimes indicates the regime transition from the top to bottom.	128

Chapter 1

Introduction

Material dispersion in the ocean, such as the dispersion of natural and anthropogenic tracers (*e.g.* nutrients, dissolved gases, pollutants), is traditionally conceptualized as a two-stage process (*e.g.* Eckart 1948; Garrett 2006; Shcherbina, *et al.* 2015). At the first stage, tracer patches are stirred by water motions like currents, eddies and nonlinear waves; the stirring process stretches tracer patches into streaks and folds the streaks again. Under the recurring stretching and folding, tracer patches become convoluted filaments, increasing the overall tracer gradients (Ottino 1989). Then at the next stage, molecular diffusion smears out the gradients, resulting in mixing. In addition to the traditional two-stage process, other processes such as chemical reaction, biological activity and human response (*e.g.* burning and surfactants), also remarkably impact the dispersion of pollutants like oil (*e.g.* Özgökmen 2016).

In this dissertation, I focus on the first stage of material dispersion, *i.e.* the stirring by macro water motions, particularly by ocean eddies and nonlinear waves. In Chapter 2, I present the material dispersion by an initially-unstable eddy, which generate a family of eddies due to hydrodynamic instabilities; this family of eddies

are connected with each other in the sense of material being circulated among them. In Chapter 3, I discover for the first time a special kind of inertial waves that are emitted from eddies in a spiral manner; thus, they are referred to as spiral inertial waves. These waves can stir tracer fields, creating spiral streaks, which enhance the overall tracer gradients and thereby mixing. In Chapter 4, I examined the material dispersion by an internal gravity wave field that is initialized with the Garrett-Munk spectrum. Based on the trajectories of particles released in the internal wave field, I adopt the metric of finite-scale Lyapunov exponent to identify the dispersion regime by internal waves only. Last, I conclude this research in Chapter 5. It is worth noting that the contents of Chapter 2 and Chapter 3 have been published in two separate papers, *i.e.* Wang and Özgökmen (2015) and Wang and Özgökmen (2016).

1.1 Instabilities of geophysical vortices

The three-dimensional (3D) material dispersion by geophysical vortices (*e.g.* ocean eddies) is crucial in understanding biological primary productions, air-sea gas exchanges, global tracer budgets, ocean general circulation, and thereby, climate variability (*e.g.* Benitez-Nelson *et al.* 2007; Chelton *et al.* 2007; McGillicuddy *et al.* 2007; Small *et al.*, 2008; Klein and Lapeyre 2009; Viebahn and Eden, 2010; Siegel *et al.* 2011; Lévy *et al.* 2012; Mahadevan *et al.* 2012). Geophysical vortices may undergo hydrodynamic instabilities, such as the barotropic instability and inertial instability, that can significantly change the material dispersion by the vortices; however, it remains unclear what effects the instabilities can cause on the 3D material dispersion by vortices.

Barotropic instability in geophysical vortices has been extensively observed in laboratory experiments (*e.g.* Greenspan 1969; Kloosterziel and van Heijst 1991; Carnevale and Kloosterziel 1994; Flór and van Heijst 1996), from satellite/radar

images (*e.g.* Pingree and Le Cann 1992; Stapleton *et al.* 2002; Kossin and Schubert 2004; Montgomery *et al.* 2006), and by numerical simulations (*e.g.* Carton, Flierl and Polvani 1989; Carton and McWilliams 1989; Orlandi and van Heijst 1992; Kloosterziel and Carnevale 1999; Schubert *et al.* 1999; Nolan and Montgomery 2000, 2001). Barotropic instability receives well-known necessary conditions derived in inviscid parallel shear flows, including Rayleigh inflection-point criterion (Rayleigh 1880), Rayleigh-Kuo inflection-point criterion (Kuo 1949) and Fjørtoft's criterion (Fjørtoft 1950).

Centrifugal instability was explored in an inviscid swirling flow by Rayleigh (1917) who derived a necessary condition, known as Rayleigh circulation criterion. Later when studying inviscid flows between coaxial cylinders, Synge (1933) pointed out that the Rayleigh circulation criterion is also a sufficient condition if perturbations are axisymmetric. When background rotation is considered, centrifugal instability is regarded as inertial instability. Inertial instability can form vertically-stacked overturning cells of selective scales (*e.g.* Dunkerton 1982; Hua, Moore and Le Gentil 1997; Afanasyev and Peltier 1998; Orlandi and Carnevale 1999; Bourlès *et al.* 2003; Griffiths 2003a; Kloosterziel and Carnevale 2008), homogenize absolute linear/angular momentum (*e.g.* Griffiths 2003b; Kloosterziel, Carnevale and Orlandi 2007; Kloosterziel, Orlandi and Carnevale 2007; Carnevale, Kloosterziel and Orlandi 2013), and affect mixing of biogeochemical tracers (*e.g.* Richards and Banks 2002; Richards and Edwards 2003; d'Orgeville *et al.* 2004).

The Rayleigh circulation criterion is, however, invalid for non-axisymmetric perturbations, and still no general stability criterion is achieved (Drazin and Reid 2004). Non-axisymmetric perturbations of swirling flows (or asymmetric perturbations of parallel flows) can draw energy from background flows and lead to non-axisymmetric inertial instability (or asymmetric inertial instability). Here the

“non-axisymmetric” (or “asymmetric”) means that the swirling (or parallel) flow is not uniform in the azimuthal (or along-flow) direction; I refer to the non-axisymmetric (or asymmetric) inertial instability as 3D instability. Further, from the perspective of normal-mode analysis, this 3D instability can be viewed as the combination of barotropic and inertial instabilities. Regarding the growth rate of 3D instability, there is an unsolved argument on whether the non-axisymmetric/asymmetric perturbations can have higher growth rates than that of the axisymmetric/symmetric ones (*e.g.* Gallaire and Chomaz 2003; Billant and Gallaire 2005; Bouchut, Ribstein and Zeitlin 2011; Ribstein, Plougonven and Zeitlin 2014).

The literature contains many studies on the onset of hydrodynamic instabilities, but fewer studies on the long-term impacts of instabilities on 3D material dispersion by the flows. In fact, some studies have explored 3D material dispersion within geophysical vortices, for instance, Rogerson *et al.* (1999), Fountain *et al.* (2000), Miller *et al.* (2002), Branicki and Kirwan (2010) and Pratt *et al.* (2014); however, these studies ignored instabilities, which can significantly impact the associated material dispersion. Indeed, as stated by Lipphardt *et al.* (2008) while studying loop current rings in the Gulf of Mexico, these rings may fall apart due to instabilities, leading to material leakage.

In addition, the dynamical systems approach has been adopted to study the material dispersion in unsteady flows by introducing the concept of Lagrangian coherent structures (LCS), which are actually a set of special material curves/surfaces, acting as transport barriers (*e.g.* Aref 1984; Ottino 1989; Haller and Yuan 2000; Haller 2001; Mezić 2001; Wiggins 2005; Samelson and Wiggins 2006; Sturman, Ottino and Wiggins 2006; Aref *et al.* 2014). However, most geophysical LCS studies are restricted to two-dimensional (2D) flows, the result of which may not be applied to realistic 3D geophysical vortices under certain situations.

1.2 Inertial waves

Inertial waves can arise in rotating homogeneous fluids due to the Coriolis force (*e.g.* Greenspan 1969), and have been observed in different geometries, including the cylinder, sphere and cube (*e.g.* Fultz 1959; McEwan 1970; Zhang *et al.* 2001; Kelly *et al.* 2007; Messio *et al.* 2008; Lopez and Marques 2011; Boisson *et al.* 2012). Inertial waves are involved in geophysics, astrophysics and engineering, such as oceanic and atmospheric flows, liquid planet cores, and spacecraft fuel tanks (*e.g.* Aldridge and Lumb 1987; Manasseh 1992; Tilgner 2007; Noir *et al.* 2009; Cortet *et al.* 2010; Bordes *et al.* 2012).

The dispersion relation of inertial waves is $\omega^2 = f^2 m^2 / K^2$ expressed in Cartesian coordinates, where ω is the frequency, f is the Coriolis parameter, m is the vertical wavenumber and K is the total wavenumber; meanwhile, the dispersion relation of inertia-gravity waves is $\omega^2 = (f^2 m^2 + N^2 K_h^2) / K^2$, where N is the buoyancy frequency and K_h is the horizontal wavenumber. Clearly, the inertial wave is an extreme of inertia-gravity wave in the limit of ($N = 0$) zero buoyancy frequency (Gill 1982); consequently, I expect that the generation mechanisms of inertia-gravity waves may also fit inertial waves. Such mechanisms include the geostrophic/Rossby adjustment (*e.g.* Rossby 1938), Lighthill-Ford radiation (Lighthill 1952; Ford 1994a, 1994b; Ford *et al.* 2000, 2002; McIntyre 2009), spontaneous balance adjustment (*e.g.* O'Sullivan and Dunkerton 1995; Zhang *et al.* 2000, 2001; Zhang 2004; Wang and Zhang 2010), unbalanced instabilities (*e.g.* Griffiths *et al.* 1982; Molemaker *et al.* 2005; Plougonven *et al.* 2005; Pratt *et al.* 2008; Gula *et al.* 2009; Vanneste 2013). In addition, the Lighthill-Ford radiation theory was extended to a forced-dissipative unsteady jet (Sugimoto *et al.* 2007; Sugimoto *et al.* 2008) and a spherical domain (Sugimoto and Ishii 2012).

Material dispersions (*e.g.* pollution dispersion, nutrient exchange) are of particular interest in geophysical flows, and has been extensively studied by means of Lagrangian particles, passive tracers and dynamical system approaches (*e.g.* Ledwell *et al.* 2008; Özgökmen *et al.* 2011; Özgökmen *et al.* 2012; Ohlmann *et al.* 2012; Chabreyrie and Llewellyn Smith 2014; Rypina *et al.* 2014). In this study, I investigate whether material dispersions are affected by inertial waves.

1.3 Dispersion regimes in Lagrangian framework

A natural way to study the material dispersion is conducted in the Lagrangian framework, which involves the solutions of the following equation:

$$\frac{d\mathbf{r}}{dt} = \mathbf{v}(t) = \mathbf{u}(\mathbf{x}, t) , \quad (1.1)$$

where \mathbf{r} is the particle position vector, $\mathbf{v}(t)$ is the Lagrangian velocity along a particle's trajectory, and $\mathbf{u}(\mathbf{x}, t)$ is the corresponding Eulerian velocity field.

The Lagrangian metrics of studying dispersion can be divided into single-particle statistics and multiple-particle (pairs or groups) statistics (LaCasce 2008). In this study, I focus on the pairwise statistics, in particular, on the metrics of relative dispersion and finite-scale Lyapunov exponent (FSLE).

The relative dispersion is defined as

$$D^2(t) = \langle (\mathbf{r}_2(t) - \mathbf{r}_1(t))^2 \rangle , \quad (1.2)$$

where \mathbf{r}_1 and \mathbf{r}_2 are the position vectors of two particles; the angle brackets, $\langle \rangle$, indicate averaging over all particle pairs. In other words, the relative dispersion (D^2) quantify the mean square separation between particles in a pair. Tracing back, the concept of relative dispersion was initiated by Richardson (1926), who was trying to

explain the increase of relative diffusivity in the atmosphere, from the spatial scale of molecular diffusion to the scale of general circulation. Richardson found that the relative diffusivity is scale-dependent, and is proportional to $D^{4/3}$, now known as Richardson's law; moreover, the corresponding relative dispersion also obeys a power law of $D^2 \propto t^3$, now known as Richardson regime of relative dispersion. In addition to Richardson regime, other regimes are often observed, for instance, the ballistic regime ($D^2 \propto t^2$) and the diffusive regime ($D^2 \propto t$).

In fact, the dispersion regimes have been shown to be related with the kinetic energy wavenumber spectrum of the underlying velocity field (*e.g.* Batchelor 1950; Babiano et al. 1990). Generally, based on the spectral slope of the kinetic energy spectrum, $E(k) \propto k^{-\beta}$, the relative dispersion can be divided into two distinct regimes, *i.e.* the local and nonlocal regimes (Bennett 1984). For shallow spectra with $1 < \beta < 3$, the dispersion satisfies $D \propto t^{2/(3-\beta)}$, and is the local regime where the separation is dominated by fluid motions with scales comparable to the separation distance; when $\beta = 5/3$, it recovers the Richardson regime, which is an example of the local dispersion. For steep spectra with $\beta \geq 3$, the dispersion grows exponentially in time, *i.e.* $D \propto e^{\lambda t}$, and is the nonlocal regime where the separation is controlled by fluid motions with scales (energy-containing scales) much larger than the separation distance.

The relative dispersion is computed by averaging particle separations at fixed times; consequently, the relative dispersion mixes the separations occurring at all spatial scales, and is dominated by the largest separations. Thus, the metric of relative dispersion can be problematic, particularly in the local dispersion regime (LaCasce 2008). Then, in order to address the dispersion rate at various spatial scales, the scale-dependent FSLE is proposed (Artale et al. 1997; Aurell et al. 1997).

The definition of FSLE is given by

$$\lambda(\delta) = \frac{\ln(\alpha)}{\langle \tau(\delta) \rangle}, \quad (1.3)$$

where $\langle \tau(\delta) \rangle$ is the time required for a particle pair to separate from a distance of δ to $\alpha\delta$, and angle brackets, $\langle \rangle$, means averaging over all particle pairs; the factor α is typically in the range of $1 < \alpha < 2$ (Haza et al. 2008). The FSLE metric takes average of the separation times at given separation distances; hence, FSLE measures the dispersion rate as a function of spatial scales, and can isolate different dispersion regimes due to various spatial scales of the underlying flows.

Similar to relative dispersion, which has different power laws under different dispersion regimes, the FSLE metric also exhibits different power laws under different dispersion regimes (Boffetta et al. 2000): $\lambda(\delta) \propto \delta^{-2/3}$ for Richardson regime, $\lambda(\delta) \propto \delta^{-1}$ for ballistic regime, $\lambda(\delta) \propto \delta^{-2}$ for diffusive regime, and $\lambda(\delta) = const.$ for exponential regime. Although both relative dispersion metric and FSLE metric identify the same kinds of dispersion regimes, the regime identified by relative dispersion metric is not necessarily consistent with that identified by FSLE metric (*e.g.* LaCasce and Bower 2000; LaCasce 2008; van Sebille et al. 2015). The reason for this discrepancy between relative dispersion and FSLE roots in their different definitions; that is, relative dispersion metric divides the regime in terms of temporal scales, while FSLE metric separates the regime based on spatial scales. Additionally, the relative dispersion and FSLE have different sensitivities to the temporal resolution and spatial resolution of the underlying velocity field (Haza et al. 2008; LaCasce 2008); this different sensitivity may also cause discrepancies in identifying dispersion regimes based on relative dispersion and FSLE metrics. Nevertheless, the debate on the best usage of both metrics is still ongoing.

Dispersion regimes are related to the kinetic energy cascade of the underlying flows; thus, the dispersion regime can be used to infer the kinetic energy spectrum, $E(k) \propto k^{-\beta}$ (Bennett 1984). For instance, a local dispersion regime (*e.g.* Richardson regime) implies a shallow kinetic energy spectrum ($1 < \beta < 3$); while a nonlocal dispersion regime (*e.g.* exponential regime) indicates a steep kinetic energy spectrum ($\beta \geq 3$). In addition, after knowing the dispersion regime at sub-mesoscale oceanic flows (spatial scales ranging from $O(100$ m) to $O(10$ km), *e.g.* McWilliams 1985), we can determine whether or not the sub-mesoscale flows are important for material transport (Schroeder *et al.* 2011; Özgökmen *et al.* 2012). If the dispersion regime at sub-mesoscales is nonlocal, the sub-mesoscale flows are weak enough to be completely controlled by mesoscale flows, and thus are unimportant for transport; then, the present eddy-resolving ocean models and satellite altimeters with current spatial resolutions are sufficient to predict the ocean transport, without the need of capturing the sub-mesoscales. However, if the dispersion regime at sub-mesoscales is local, the sub-mesoscale flows play an important role in transport, controlling the material dispersion at their own scales; hence, to accurately predict the ocean transport, ocean models and satellite altimeters have to resolve all the sub-mesoscales.

1.4 Scientific questions

The upper ocean mixed layers involve many processes, such as the heating/cooling sea surface, atmospheric high/low pressures, Langmuir circulation, surface gravity waves, fronts, *etc..* These processes can potentially trigger the hydrodynamic instabilities of mixed-layer eddies, which play an important role in material dispersion; thus, understanding the effects of instabilities on mixed-layer eddies is necessary for better studying material dispersion.

Typically, mixed-layer eddies are not in geostrophic balance, containing significant ageostrophic motions. Previous studies (*e.g.* Ford 1994) show that the unbalanced eddies in rotating, stratified fluids can spontaneously emit internal-inertia-gravity waves; however, the mixed layers are vertically homogeneous and do not permit internal waves. From the aspect of dispersion relation, the internal-inertia-gravity waves degenerate to inertial waves, for the buoyancy frequency is zero in the mixed layers. Therefore, the inertial wave is another candidate that is responsible for material dispersion in mixed layers.

Nowadays, various regimes of material dispersion have been recognized under different oceanic flows by methods of field observations (*e.g.* LaCasce and Bower 2000; LaCasce 2008; Lumpkin and Eliot 2010; Poje et al. 2014; van Sebille et al. 2015) and numerical simulations (*e.g.* Haza et al. 2008; Özgökmen et al. 2012; Mensa et al. 2015). However, these dispersion regimes are usually associated with ocean currents, mesoscale and submesoscale eddies, and other processes like Langmuir circulations, convections, *etc.* The dispersion regime by internal waves only, to our knowledge, has not been well investigated.

Therefore, in this dissertation, I address the following scientific questions:

1. The normal thinking of the vertical material dispersion by an cyclonic ocean eddy is that material is transported upward by the upwelling inside the core of eddy and is advected downward by the downwelling outside the eddy core. However, when the eddy undergoes hydrodynamic instabilities, will this picture of vertical material dispersion be changed? Will new material transport pathways within the eddy be created? (Refer to Chapter 2)
2. Compared with inertia-gravity waves, inertial waves which are possible in ocean mixed layers are less studied in the society of oceanography. For instance, it remains unclear that under what conditions, ocean eddies can emit inertial waves? What

is/are the mechanism(s) for the emission of inertial waves? In the presence of inertial waves, do the waves have an effect on material dispersion? (Refer to Chapter 3)

3. Once generated, internal gravity waves can propagate away from their wave sources into various parts of the ocean. During their propagation, the internal waves inevitably affect the flows in the regions where they pass, and thereby the material dispersion by the flows. However, it is unclear which dispersion regime the internal waves can produce, particularly when only the internal waves are present. Besides, will the internal waves below the upper ocean mixed layers cause material dispersion in the mixed layer? If they can, which dispersion regime? (Refer to Chapter 4).

Chapter 2

Unstable ocean eddies

2.1 Overview

In this chapter, the hydrodynamic instabilities associated with geophysical vortices are examined using both analytical and numerical methods; here, three major types of hydrodynamic instability, *i.e.* barotropic, inertial and 3D instabilities, are studied. Further, this chapter documents the effects caused by the instabilities on material dispersion by vortices.

This chapter is organized as follows. In section 2.2, I outline the configurations of numerical experiments. In section 2.3, I analyze barotropic, inertial and 3D instabilities using normal-mode method, and reproduce the characteristics of these instabilities via numerical simulations. The impacts of instabilities on 3D material dispersion are presented in section 2.4, and are discussed in section 2.5.

2.2 Numerical model

Numerical simulations are used to study how instabilities develop and affect 3D material dispersion in geophysical vortices. The simulations are performed with NEK5000 which is a Navier-Stokes (N-S) solver based on the spectral element method

(*e.g.* Patera 1984; Maday and Patera 1990; Fischer 1997). NEK5000 has been used for investigating oceanic phenomena, including gravity currents, mixed-layer instabilities (*e.g.* Özgökmen *et al.* 2007, 2011) and, in a more relevant study to the present one, chaotic advection in an ocean eddy (Pratt *et al.* 2014). NEK5000 is adopted here for several reasons. First, its geometrical flexibility allows for a cylindrical domain that is natural for vortices. Second, it uses third-order semi-implicit time stepping and has high-order accuracy through spectral expansions. Last, NEK5000 can solve the 3D N-S equations without any ad-hoc parameterizations. In contrast, many ocean general circulation models are subject to the hydrostatic approximation, in which a reduced form of the vertical momentum equation is used and vertical advection of tracers is complicated because of the vertical coordinate system incorporated in these models (Chassignet *et al.* 2006). Also, many ocean models contain various parameterizations, particularly near the surface of the ocean; for instance, KPP (Large, McWilliams, Doney 1994) mixing scheme is a popular parameterization suite. Here I compromise with realism by adopting an idealized flow configuration (*i.e.* homogeneous density and isolation from the ambient flow), but benefit from a systematic study of this highly resolved 3D, non-hydrostatic flow.

NEK5000 is configured to solve the following dimensionless equations of motion (3.1):

$$\frac{\partial \mathbf{u}}{\partial t} + (\mathbf{u} \cdot \nabla) \mathbf{u} = -\nabla p - Ro^{-1} \hat{\mathbf{k}} \times \mathbf{u} + Re^{-1} \nabla^2 \mathbf{u}, \quad (2.1a)$$

$$\nabla \cdot \mathbf{u} = 0. \quad (2.1b)$$

In this system, the key parameters are Rossby number and Reynolds number. The Rossby number is $Ro = U/(fL)$, where U and L are characteristic horizontal velocity and length scales, and $f = 2\Omega$ is the Coriolis parameter with Ω being the angular

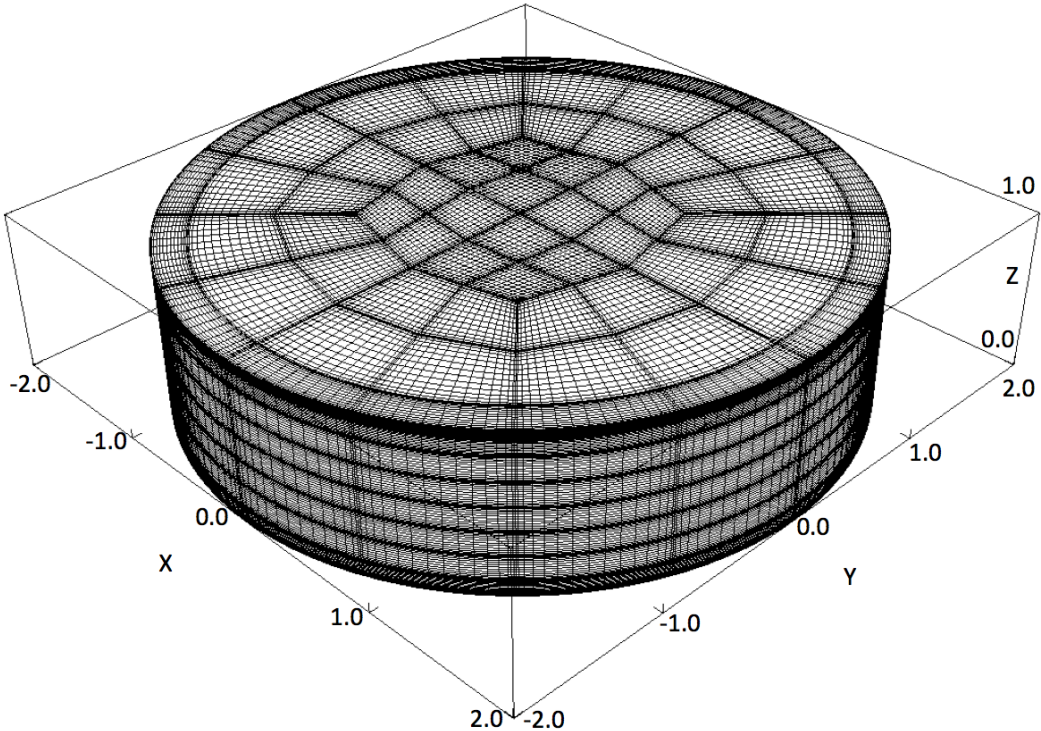


Figure 2.1: The cylindrical domain of numerical experiments.

velocity of the system rotating about its vertical axis. The Reynolds number is $Re = UL/\nu$, where ν is the kinematic viscosity. $\hat{\mathbf{k}}$ is the unit vector in the vertical direction. Based on parameter sensitivity tests, I use fixed $Re = 10^4$, which is large enough to permit the emergence of hydrodynamic instabilities without posing major challenges to capturing all degrees of freedom in the flow by the model resolution. In addition to Eq. (3.1), a passive scalar (tracer) C is used to visualize transport pathways, which requires the solution of:

$$\frac{\partial C}{\partial t} + (\mathbf{u} \cdot \nabla)C = Pe^{-1}\nabla^2C , \quad (2.2)$$

where $Pe = UR/\kappa$ is the Péclet number and κ is the diffusivity of passive scalar.

The numerical domain (Fig. 2.1) is a cylinder with diameter $D = 4$ and height $H = 1$, and is discretized into 640 elements with more grid points at boundaries to

better resolve thin boundary layers. Solutions on each element are represented by Legendre polynomials of order $N = 15$ (total 2,621,440 grid points). The domain is full of homogeneous fluid and rotates about its central axis at an angular velocity of Ω . At time = 0, a barotropic vortex is initialized in the center of the domain. The boundary conditions are free-slip on the sidewall, no-slip on the bottom, and prescribed velocity (Dirichlet) on the top. This Dirichlet boundary condition mimics a rotating disk which sustains the flow; the prescribed velocity has the same azimuthal profile with the initial vortex. As explained by Pratt *et al.* (2014), when a top and/or bottom Ekman layer has developed in a vortex, a secondary circulation will be created, driving a 3D overturning transport within the vortex.

To highlight the impacts of instabilities, I conduct two series of experiment listed in Table 3.1; one is called the target experiment in which the initial vortex is given by Eq. (2.3a), while the other is the control experiment in which the initial vortex is defined by Eq. (2.3b), shown in Fig. 2.2,

$$V(r) = 2r \exp(-12r^8), \quad (2.3a)$$

$$V(r) = 3.3r \exp(-2r^2). \quad (2.3b)$$

Both initial vortices are cyclonic with a core of positive vorticity and an annulus of negative vorticity outside the core, also known as the shielded vortex. The no-slip boundary condition at the bottom will interrupt the initial vortex, introducing perturbations into flows. With proper parameters (Ro, Re), the vortex in the target experiment supports the growth of perturbations to develop instabilities, whereas the vortex in the control experiment forbids instabilities.

The numerical model is integrated with a dimensionless time step of 10^{-3} for a total integration time of 500. For the experiments listed in Table 3.1, the flow's kinetic

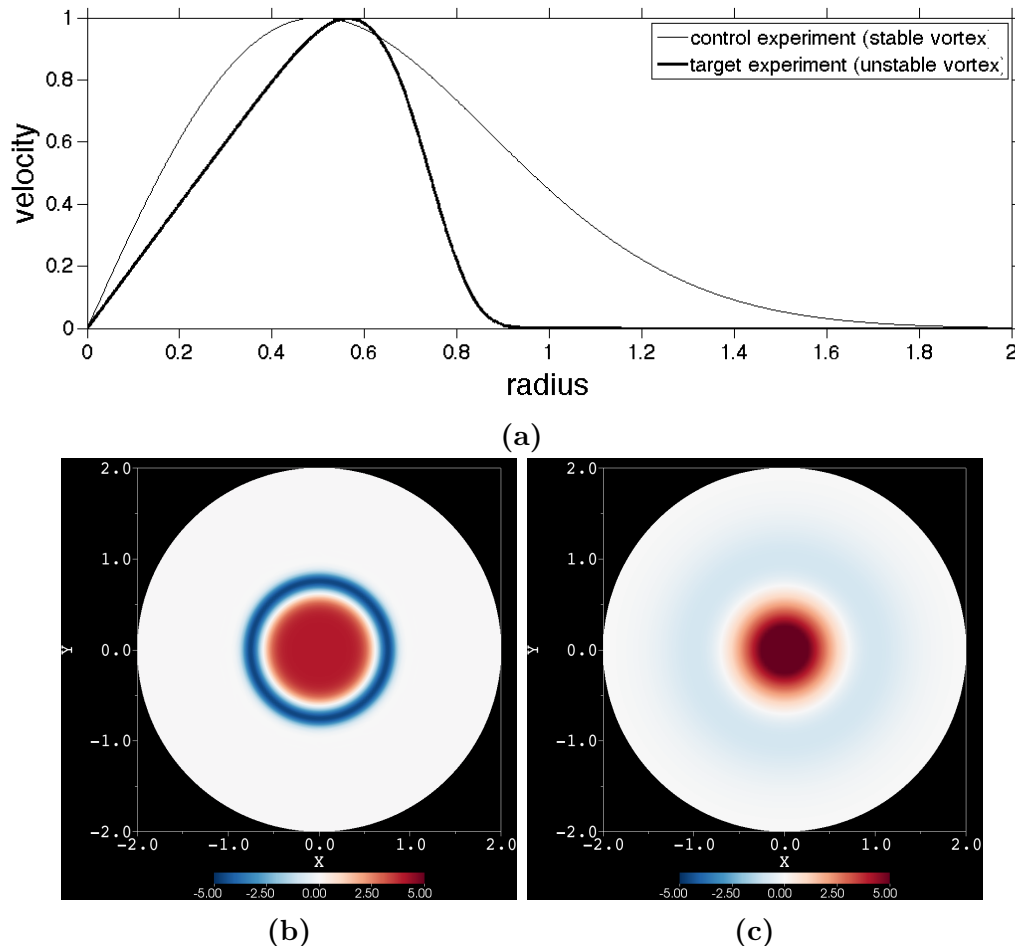


Figure 2.2: (a) Initial velocity profiles of the control and target experiments. Initial vorticity fields at mid-depth horizontal plane in (b) the target experiment and (c) the control experiment.

Table 2.1: List of the target (T) and control (C) experiments. Note that the initial vortex in the target experiment T4 is anticyclonic, denoted by “–Eq. (2.3a)”; that is, its flow direction is opposite to that of the flow given by Eq. (2.3a).

Experiment	Initial vortex profile	Ro	Re
T1	Eq. (2.3a)	0.2	10^4
T2	Eq. (2.3a)	0.04	10^4
T3	Eq. (2.3a)	1	10^4
T4	–Eq. (2.3a)	1	10^4
C1	Eq. (2.3b)	0.2	10^4

energy reaches quasi-equilibrium around a integration time of 200. Furthermore, convergence checks are performed in domains of a higher resolution with polynomial order $N = 25$ (total 11,248,640 grid points) and a lower resolution with $N = 11$ (total 1,105,920 grid points). The numerical convergence is confirmed by the convergence of kinetic energy (Fig. 2.3).

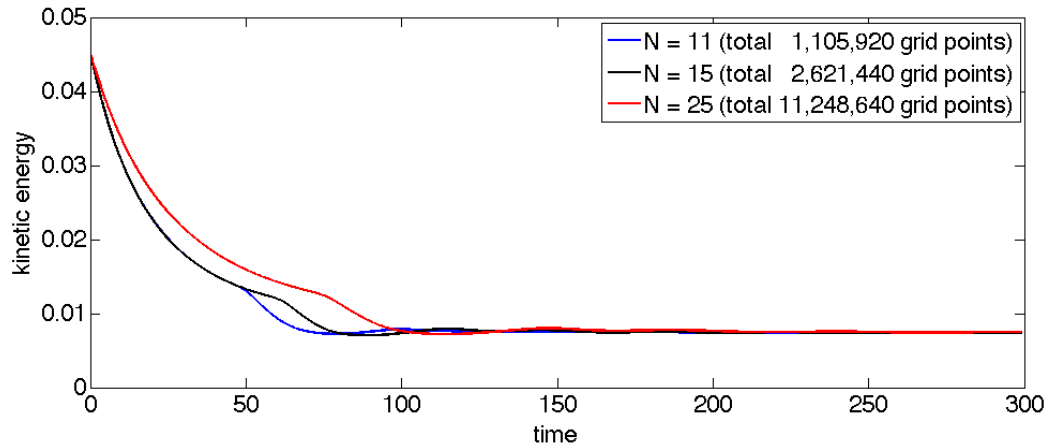


Figure 2.3: An example of the numerical convergence check (from the target experiment T1). N is the order of Legendre polynomials for numerical solutions.

It is worth mentioning that from the point of view of numerical configurations, the primary differences between our study and the one by Pratt *et al.* (2014) are

the Reynolds number and initial velocity profile. In the regime of low $Re \lesssim O(10^2)$, Pratt *et al.* (2014) carefully investigated 3D material dispersion inside a stable eddy. Another difference is that the initial vortex in our study is far away from domain sidewalls in order to weaken boundary effects.

2.3 Analysis of instabilities

2.3.1 Barotropic instability

Consider a circular-symmetric, inviscid vortex defined in a cylindrical coordinates (r, θ, z) . Its velocity components in the radial (r), azimuthal (θ) and vertical/axial (z) direction are denoted by u, v, w , respectively. I analyze its barotropic instability on an f -plane using the linearized equation of quasi-geostrophic potential vorticity in shallow water systems, *i.e.*

$$\frac{D}{Dt}(\nabla^2\psi' - \lambda^2\psi') = -u'\frac{\partial}{\partial r}(\nabla^2\bar{\psi} - \lambda^2\bar{\psi}) , \quad (2.4)$$

with deformation radius λ^{-1} and streamfunction $\psi(r, \theta, t) = \bar{\psi}(r) + \psi'(r, \theta, t)$, where $\bar{\psi}(r)$ is the basic-state streamfunction and $\psi'(r, \theta, t)$ represents small-amplitude perturbations. Define the perturbation of radial velocity $u' = -\frac{1}{r}\frac{\partial\psi'}{\partial\theta}$, basic-state angular velocity $\bar{\omega}(r) = \bar{v}/r$, Laplacian operator $\nabla^2 = \frac{1}{r}\left[\frac{\partial}{\partial r}\left(r\frac{\partial}{\partial r}\right) + \frac{\partial^2}{r\partial\theta^2}\right]$ and $\frac{D}{Dt} = \left(\frac{\partial}{\partial t} + \frac{\bar{v}}{r}\frac{\partial}{\partial\theta}\right)$.

Seek normal-mode solution in the form of $\psi'(r, \theta, t) = \text{Re}[\hat{\psi}(r)e^{i(m\theta-\sigma t)}]$, where $\text{Re}[\cdot]$ denotes “the real part of”, m is azimuthal wavenumber and $\sigma = \sigma_r + i\sigma_i$ is complex frequency; substituting it into Eq. (2.4), I obtain

$$(\sigma - m\bar{\omega})\left[r\frac{d}{dr}\left(r\frac{d\hat{\psi}}{dr}\right) - m^2\hat{\psi}\right] + \left(mr\frac{d\bar{\zeta}}{dr} - \lambda^2\sigma r^2\right)\hat{\psi} = 0 , \quad (2.5)$$

where $\bar{\omega}(r) = \bar{v}/r$ is angular velocity and $\bar{\zeta}(r) = \nabla^2\bar{\psi}$ is the vertical component of relative vorticity of basic-state flow.

Multiply Eq. (2.5) by $\hat{\psi}^*$ (the conjugate of $\hat{\psi}$) and integrate over domain with the condition $\hat{\psi} = 0$ at domain boundaries. Taking imaginary part of the above integral and assuming $\sigma - m\bar{\omega} \neq 0$, I get

$$\sigma_i \int \left(\frac{\frac{d\bar{\zeta}}{dr} - \lambda^2 \bar{v}}{|\sigma - m\bar{\omega}|^2} r^2 |\hat{\psi}|^2 \right) dr = 0 , \quad (2.6)$$

with

$$\frac{d\bar{\zeta}}{dr} - \lambda^2 \bar{v} = \frac{d}{dr} (\nabla^2 \bar{\psi} - \lambda^2 \bar{\psi}) . \quad (2.7)$$

That is,

$$\sigma_i \int \left(\frac{\frac{d}{dr} (\nabla^2 \bar{\psi} - \lambda^2 \bar{\psi})}{|\sigma - m\bar{\omega}|^2} r^2 |\hat{\psi}|^2 \right) dr = 0 . \quad (2.8)$$

Since growth rate $\sigma_i \neq 0$, the integral in Eq. (2.8) must be zero, yielding the necessary condition for barotropic instability; that is, the radial gradient of basic-state potential vorticity, *i.e.* $\frac{d}{dr} (\nabla^2 \bar{\psi} - \lambda^2 \bar{\psi})$, changes sign at least once within the domain. This condition recovers Rayleigh inflection-point criterion, if deformation radius is infinite ($\lambda = 0$).

To calculate growth rates, I choose piecewise-constant vorticity model (*e.g.* Michalke and Timme 1967; Flierl 1988; Schubert *et al.* 1999; Terwey and Montgomery 2002) as the basic-state relative vorticity, *i.e.*

$$\bar{\zeta}(r) = \nabla^2 \bar{\psi}(r) = \begin{cases} \zeta_1 + \zeta_2 & (0 < r < r_1) , \\ \zeta_2 & (r_1 < r < r_2) , \\ 0 & (r_2 < r < \infty) , \end{cases} \quad (2.9)$$

where ζ_1 , ζ_2 , r_1 and r_2 are constants. This vorticity model is discontinuous at inner radius r_1 and outer radius r_2 , and thus can generate edge waves to cause instability when they interact with each other (Vallis 2006). As stated by Smyth and McWilliams (1998), each unstable mode has at least one critical radius r_c at which phase speed is equal to the basic-state angular velocity ($\sigma_r - m\bar{\omega} = 0$), *i.e.* Doppler-shift frequency vanishes; thus I can simplify Eq. (2.5) at $r = r_c$ but with $r \neq r_1, r_2$, yielding Eq. (2.10),

$$\frac{d^2\hat{\psi}}{dr^2} + \frac{1}{r} \frac{d\hat{\psi}}{dr} - (\lambda^2 + \frac{m^2}{r^2})\hat{\psi} = 0 , \quad (2.10)$$

which is the modified Bessel equation of order m . (Note that here r is actually the critical radius r_c ; as the critical radius could be anywhere in the domain, r_c is also a variable, within the range of $[0, \infty]$; for clarity, we still keep r instead of r_c .) Since $\hat{\psi}(r)$ is bounded as $r \rightarrow 0$ and $r \rightarrow \infty$, and is continuous at r_1 and r_2 , I write the general solution of Eq. (2.10) as

$$\hat{\psi}(r) = \psi_1 B_m^{(1)}(r) + \psi_2 B_m^{(2)}(r) , \quad (2.11)$$

where ψ_1 and ψ_2 are constants. $B_m^{(1)}(r)$ and $B_m^{(2)}(r)$ are defined as

$$B_m^{(1)}(r) = \begin{cases} I_m(\lambda r)K_m(\lambda r_1) & (0 \leq r \leq r_1) , \\ I_m(\lambda r_1)K_m(\lambda r) & (r_1 \leq r \leq \infty) , \end{cases} \quad (2.12a)$$

$$B_m^{(2)}(r) = \begin{cases} I_m(\lambda r)K_m(\lambda r_2) & (0 \leq r \leq r_2) , \\ I_m(\lambda r_2)K_m(\lambda r) & (r_2 \leq r \leq \infty) , \end{cases} \quad (2.12b)$$

where $I_m(x)$ and $K_m(x)$ are modified Bessel functions of the first and second kind.

Then substitute solution (2.11) into the jump condition which is derived by integrating Eq. (2.5) across interface r_1 and r_2 , yielding

$$\begin{pmatrix} \sigma - m\bar{\omega}_1 + m\zeta_1 G_{11} & m\zeta_1 G_{12} \\ m\zeta_2 G_{12} & \sigma - m\bar{\omega}_2 + m\zeta_2 G_{22} \end{pmatrix} \begin{pmatrix} \psi_1 \\ \psi_2 \end{pmatrix} = \begin{pmatrix} 0 \\ 0 \end{pmatrix}, \quad (2.13)$$

where $\bar{\omega}_1$, $\bar{\omega}_2$, G_{11} , G_{22} and G_{12} are given by

$$\bar{\omega}_i = \bar{\omega}(\lambda r_i) \quad (i = 1, 2), \quad (2.14a)$$

$$G_{ij} = I_m(\lambda r_i) K_m(\lambda r_j) \quad (i, j = 1, 2). \quad (2.14b)$$

The determinant of coefficient matrix of Eq. (2.13) must be zero for nontrivial ψ_1 and ψ_2 , and I obtain the dispersion relation

$$\sigma = \frac{1}{2}(\sigma_1 + \sigma_2) \pm \frac{1}{2}\sqrt{(\sigma_1 - \sigma_2)^2 + 4m^2\zeta_1\zeta_2 G_{12}^2}, \quad (2.15)$$

where $\sigma_1 = m\bar{\omega}_1 - m\zeta_1 G_{11}$ and $\sigma_2 = m\bar{\omega}_2 - m\zeta_2 G_{22}$ are frequencies of non-interacting edge waves living at the interfaces $r = r_1, r_2$. This dispersion relation is essentially identical to that of Flierl (1988, his Eq. 3.4) who used a different method (contour dynamics method). Instability requires that σ has nonzero imaginary part, yielding the necessary condition, *i.e.* $\zeta_1\zeta_2 < 0$, for the piecewise-constant vorticity model given by Eq. (2.9). If deformation radius approaches infinity, I have the following equations

$$\lim_{\lambda \rightarrow 0} G_{11} = \frac{1}{2m}, \quad \lim_{\lambda \rightarrow 0} G_{22} = \frac{1}{2m}, \quad \lim_{\lambda \rightarrow 0} G_{12} = \left(\frac{r_1}{r_2}\right)^m \frac{1}{2m}. \quad (2.16)$$

Substituting Eqs. (2.16) into Eq. (2.15), I recover the dispersion relation which was derived by Schubert *et al.* (1999, their Eq. 2.10) and Terwey and Montgomery (2002, their Eq. 8) for purely 2D vortex flows. Furthermore, by defining $\delta = r_1/r_2$ and

$\varepsilon = -\zeta_2/\zeta_1$, and dividing the imaginary part of σ in Eq. (2.15) by $|\zeta_1|$, I get the normalized growth rate

$$\hat{\sigma}_i = \frac{\sigma_i}{|\zeta_1|} = \frac{1}{2}m\sqrt{-\left(\frac{1}{2} - G_{11} - \frac{1}{2}\delta^2 - \varepsilon G_{22}\right)^2 - 4\varepsilon G_{12}^2}. \quad (2.17)$$

As indicated by Fig. 2.4, the growth rate $\hat{\sigma}_i$ changes significantly with different length ratio $F = \lambda r_2$ which represents the ratio of flow horizontal length scale to Rossby deformation radius.

Besides, an example of barotropic instability shown in Fig. 2.5 demonstrates that azimuthal wavenumber $m = 2$ (wavenumber-2) instability can produce two satellite vortices (of negative vorticity), while wavenumber-1 instability distorts one of the satellite vortices by shifting the central vortex towards it.

2.3.2 Inertial instability

Consider a vortex with a basic-state swirling flow $[0, \bar{v}(r), 0]$ which is in gradient wind balance and in hydrostatic balance. I analyze its inertial instability on an f -plane in cylindrical coordinates using normal-mode method. Assume that the flow is axisymmetric ($\frac{\partial}{\partial\theta} \equiv 0$), inviscid and homogeneous. The linearized governing equations are (primes denoting perturbations)

$$\frac{\partial u'}{\partial t} - \frac{2\bar{v}v'}{r} - fv' = -\frac{1}{\rho}\frac{\partial p'}{\partial r}, \quad (2.18a)$$

$$\frac{\partial v'}{\partial t} + u'\frac{\partial \bar{v}}{\partial r} + \frac{\bar{v}u'}{r} + fu' = 0, \quad (2.18b)$$

$$\frac{\partial w'}{\partial t} = -\frac{1}{\rho}\frac{\partial p'}{\partial z}, \quad (2.18c)$$

$$\frac{1}{r}\frac{\partial(ru')}{\partial r} + \frac{\partial w'}{\partial z} = 0. \quad (2.18d)$$

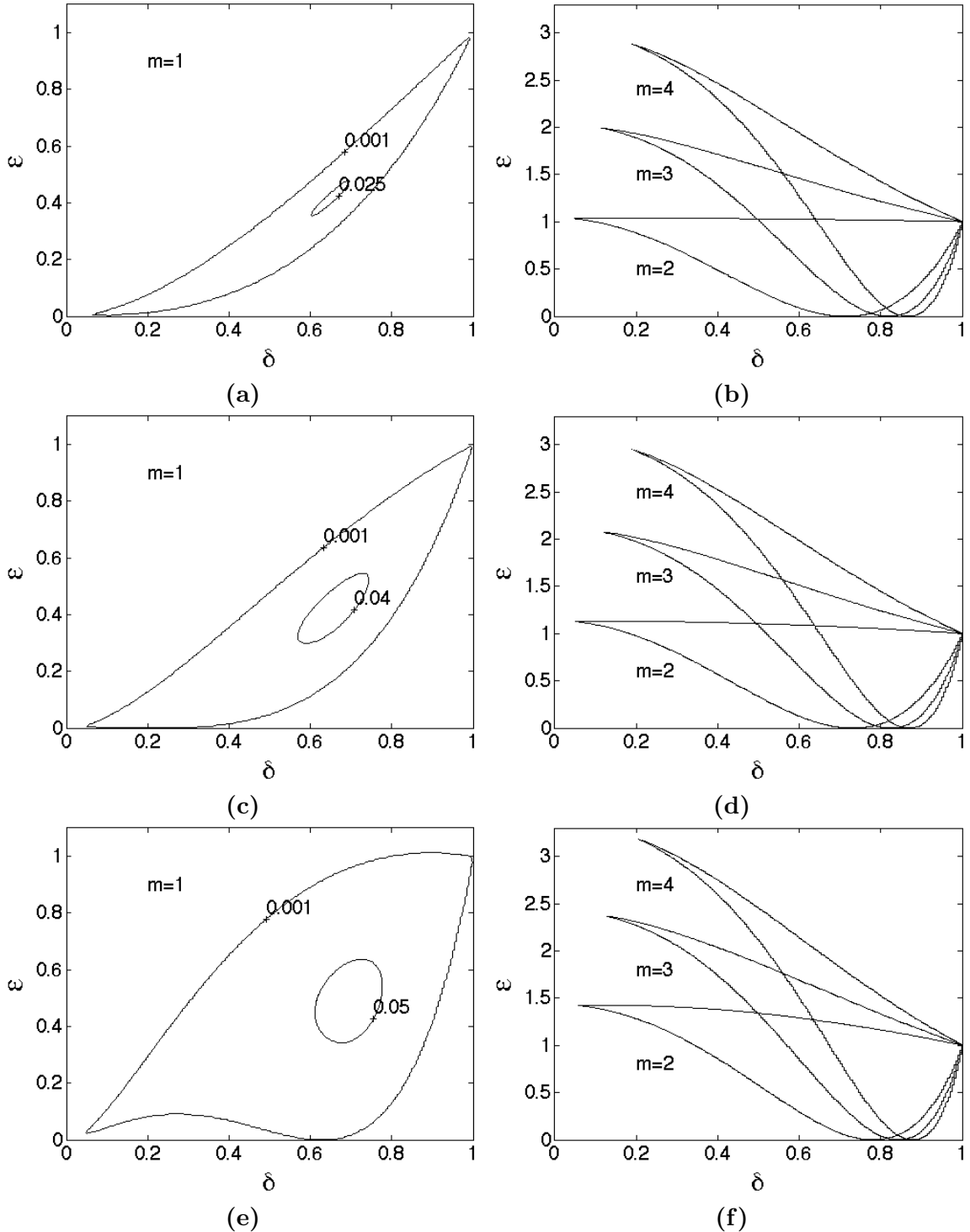


Figure 2.4: Contours of normalized growth rates in δ - ε space for different azimuthal wavenumber m and length ratio F ; left column: $m = 1$, right column: $m = 2, 3, 4$; (a, b) $F = 0.5$, (c, d) $F = 1$, (e, f) $F = 2$. Closed regions have nonzero growth rate; contours in the right column depict level 0.001.

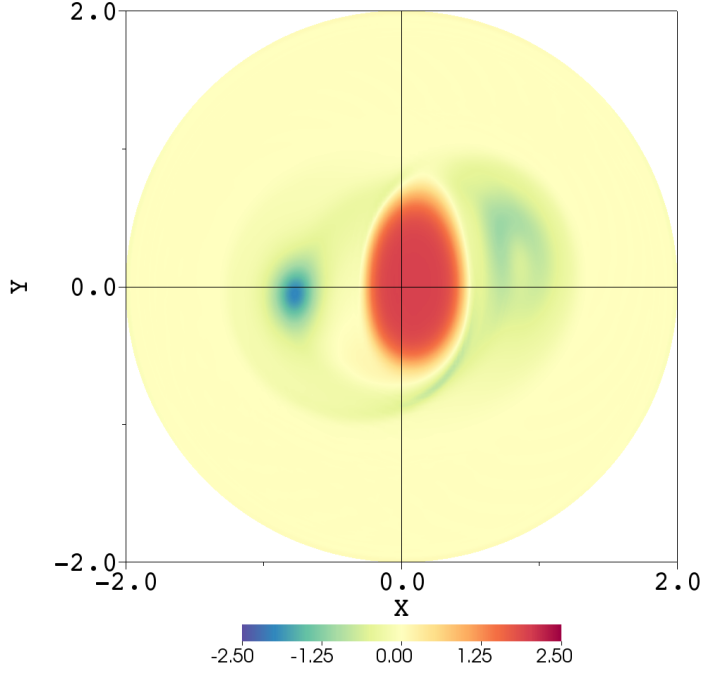


Figure 2.5: Vertical vorticity at mid-depth horizontal plane from the target experiment T2, showing the asymmetric effect of azimuthal wavenumber-1 instability that shifts the central vortex off center, towards one of the two satellite vortices.

Using equations (2.18a)–(2.18c), I obtain the equation of perturbation vorticity in azimuthal direction ($\omega'_\theta = \frac{\partial u'}{\partial z} - \frac{\partial w'}{\partial r}$), *i.e.*

$$\frac{\partial^2 \omega'_\theta}{\partial t^2} + \Phi \frac{\partial u'}{\partial z} = 0 , \quad (2.19)$$

where $\Phi = (2\bar{\omega} + f)(\bar{\zeta} + f)$ with basic-state vertical vorticity $\bar{\zeta} = \frac{1}{r} \frac{d(r\bar{v})}{dr}$, angular velocity $\bar{\omega} = \bar{v}/r$ and Coriolis parameter f . Next, I introduce ψ' as the perturbation of streamfunction, and express $u' = -\frac{\partial \psi'}{\partial z}$, $w' = \frac{1}{r} \frac{\partial(r\psi')}{\partial r}$. Substituting the normal-mode solution, $\psi'(r, z, t) = \text{Re}[\hat{\psi}(r)e^{(\sigma_i t + ikz)}]$, where $\text{Re}[\cdot]$ denotes “the real part of”, σ_i is growth rate and k is vertical wavenumber, I can rewrite Eq. (2.19) as

$$\frac{d^2 \hat{\psi}}{dr^2} + \frac{1}{r} \frac{d\hat{\psi}}{dr} + \left(\mu - \frac{1}{r^2} \right) \hat{\psi} = 0 , \quad (2.20)$$

where $\mu = k^2 (-\Phi/\sigma_i^2 - 1)$ and $\sigma_i^2 \neq 0$. For simplicity, μ is assumed to be constant and then Eq. (2.20) can be treated as Bessel, Cauchy-Euler or modified Bessel differential equation for $\mu > 0$, $\mu = 0$ or $\mu < 0$, respectively. Physically, $\hat{\psi}(r)$ is bounded as $r \rightarrow 0$ and $r \rightarrow \infty$, which will be satisfied only when $\mu > 0$. Therefore, Eq. (2.20) becomes Bessel equation of order one and its solution is

$$\hat{\psi}(r) = C J_1(x) = C J_1(\sqrt{\mu} r) ,$$

where C is a constant and $J_1(x)$ is Bessel function of the first kind of order one. Denote the n th zero-crossing of $J_1(x)$ by $x_0^{(n)}$. With boundary condition $\hat{\psi}(R) = 0$, *i.e.* $J_1(\sqrt{\mu} R) = 0$, where R is vortex radius, I obtain the eigenvalue μ and growth rate σ_i of mode n ,

$$\mu^{(n)} = \left(\frac{x_0^{(n)}}{R} \right)^2 , \quad \sigma_i^{(n)} = \sqrt{\frac{-\Phi}{1 + \mu^{(n)}/k^2}} , \quad (n = 1, 2, 3, \dots) \quad (2.21)$$

According to the above Eq. (2.21), for fixed vertical wavenumber k , growth rate of mode $n = 1$ is the largest, since the zero-crossings of Bessel function increase monotonically, *i.e.* $x_0^{(n+1)} > x_0^{(n)} > 0$. In addition, the growth rate increases with increasing wavenumber k ; as $k \rightarrow \infty$, the growth rate σ_i reaches its upper limit $(-\Phi)^{1/2}$. Hence, the maximum growth rate that inertial instability can gain is $(-\Phi_{min})^{1/2}$, where Φ_{min} is the minimum of Φ (*if* $\Phi < 0$).

Inertial instability requires $\Phi < 0$ in Eq. (2.21) of the growth rate, *i.e.*

$$(2\bar{\omega} + f)(\bar{\zeta} + f) < 0 , \quad (2.22)$$

which is identical to the result obtained by Kloosterziel and van Heijst (1991) using particle-instability method. In terms of Eq. (2.22), I can qualitatively discuss the

effect of background rotation on the inertial instability in a vortex. When $f > 0$, a cyclonic vortex has $\bar{\omega} > 0$; then background rotation (f) tries to keep both terms $(2\bar{\omega} + f)$ and $(\zeta + f)$ to be positive, suppressing inertial instability to stabilize the cyclonic vortex. For an anticyclonic vortex ($\bar{\omega} < 0$), however, background rotation may stabilize or destabilize the flow depending on the micro Rossby number which is defined as $Ro_\zeta = |\zeta|/f$. If $Ro_\zeta \ll 1$, the two terms, $(2\bar{\omega} + f)$ and $(\zeta + f)$, tend to be positive, since f is dominant; therefore background rotation has stabilizing effect in this case. If $Ro_\zeta \gg 1$ then background rotation has little effect on vortex stability. If $Ro_\zeta \sim O(1)$, the above two terms are both about zero and may easily have opposite signs somewhere, causing $\Phi < 0$ and triggering inertial instability. Indeed, vigorous inertial instability in anticyclonic vortices with $Ro_\zeta \sim O(1)$ has been widely reported (e.g. Lesieur, Yanase and Métais 1991; Afanasyev and Peltier 1998; Orlandi and Carnevale 1999). In brief, background rotation has different stabilization effects on cyclonic and anticyclonic vortices, also known as selective stabilization.

Additionally, an example of inertial instability shown in Fig. 2.6 manifests that inertial instability can create toroidal/rib vortices that collapse later, causing vortex breaking.

2.3.3 Three-dimensional instability

Barotropic and inertial instabilities are essentially 2D, since flows in the analysis presented in sections 2.3.1 and 2.3.2 are always uniform in one direction (the vertical or azimuthal). In fact, geophysical vortices may simultaneously undergo barotropic and inertial instabilities, allowing perturbations in all three directions and leading to 3D instability. Consider a vortex with a basic-state velocity $[0, \bar{v}(r), 0]$ which is in gradient wind balance and in hydrostatic balance. I analyze its stability on an f -plane in cylindrical coordinates using normal-mode method. The linearized

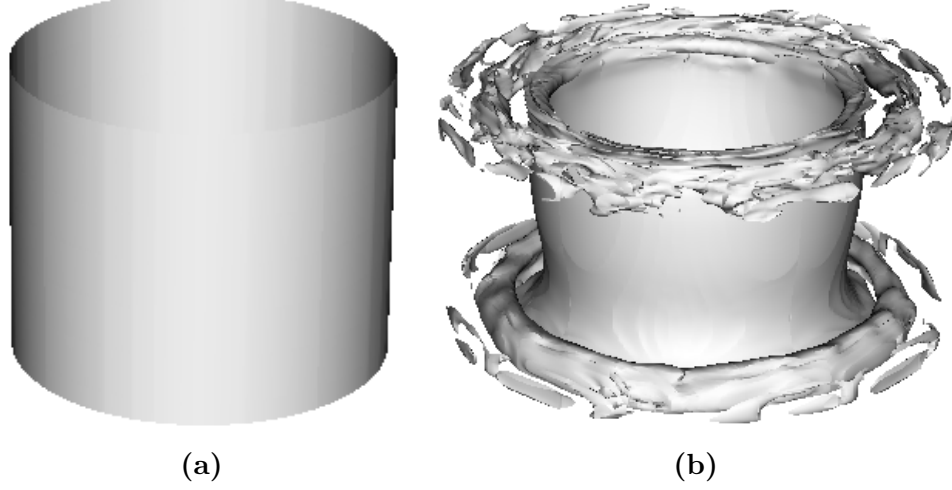


Figure 2.6: The generation of toroidal/rib vortices by inertial instability from the target experiment T4, visualized by the isosurface of vertical vorticity equal to -1 at (a) time = 0 and (b) time = 8.

governing equations are (primes denoting perturbations)

$$\frac{\partial u'}{\partial t} + \bar{v} \frac{\partial u'}{\partial \theta} - \frac{2\bar{v}v'}{r} - fv' = -\frac{1}{\rho} \frac{\partial p'}{\partial r}, \quad (2.23a)$$

$$\frac{\partial v'}{\partial t} + u' \frac{\partial \bar{v}}{\partial r} + \bar{v} \frac{\partial v'}{\partial \theta} + \frac{u'\bar{v}}{r} + fu' = -\frac{1}{\rho r} \frac{\partial p'}{\partial \theta}, \quad (2.23b)$$

$$\frac{\partial w'}{\partial t} + \bar{v} \frac{\partial w'}{\partial \theta} = -\frac{1}{\rho} \frac{\partial p'}{\partial z}, \quad (2.23c)$$

$$\frac{1}{r} \frac{\partial(ru')}{\partial r} + \frac{1}{r} \frac{\partial v'}{\partial \theta} + \frac{\partial w'}{\partial z} = 0. \quad (2.23d)$$

Manipulating equations (2.23a) – (2.23c) to eliminate variable p' , I get equations for the azimuthal and radial component of perturbation vorticity. Assume normal-mode solutions $(u', v', w') = \text{Re}\{[\hat{u}(r), \hat{v}(r), \hat{w}(r)]e^{i(m\theta+kz-\sigma t)}\}$, where $\text{Re}[\]$ denotes “the real part of”, m and k is wavenumber in the azimuthal and vertical direction, and $\sigma = \sigma_r + i\sigma_i$ is complex frequency. Substitute solutions into the new equations as well as Eq. (2.23d), apply the critical-radius relation, *i.e.* $\sigma_r - m\bar{\omega} = 0$, plug r_c into

r , and take the imaginary parts, yielding

$$\sigma_i k \hat{u} - \left(\frac{2\bar{v}}{r_c} + f \right) k \hat{v} + \frac{\bar{v}}{r_c} \frac{m}{r_c} \hat{w} = 0 , \quad (2.24a)$$

$$(\bar{\zeta} + f) k \hat{u} + \sigma_i k \hat{v} - \sigma_i \frac{m}{r_c} \hat{w} = 0 , \quad (2.24b)$$

$$\frac{m}{r_c} \hat{v} + k \hat{w} = 0 . \quad (2.24c)$$

The determinant of equations (2.24) must be zero for nontrivial solution, giving growth rate

$$\sigma_i = \sqrt{-\Phi \left[\frac{k^2 + (m/r_c)^2}{k^2 + (m/r_c)^2} \eta \right]} , \quad (m, k \neq 0) , \quad (2.25)$$

where $\Phi = (2\bar{\omega} + f)(\bar{\zeta} + f)$ and $\eta = \bar{\omega}/(2\bar{\omega} + f)$ with basic-state angular velocity $\bar{\omega} = \bar{v}/r$, vertical vorticity $\bar{\zeta} = \frac{1}{r} \frac{d(r\bar{v})}{dr}$ and Coriolis parameter f . I compute the growth rate for the vortex given by Eq. (2.3a), with critical radius $r_c = 0.752$ and $\eta = 0.113$ being used in Eq. (2.25). This growth rate shown in Fig. 2.7 is similar to that of Billiant and Gallaire (2005) who computed the growth rate using the large-axial-wavenumber WKB approximation.

In terms of Eq. (2.25), I can qualitatively discuss the problem on whether the non-axisymmetric/asymmetric perturbations can have higher growth rates than that of the axisymmetric/symmetric ones. In cyclonic vortices, since η satisfies the relation of $0 < \eta < 1/2$, the growth rate in Eq. (2.25) is less than $(-\Phi)^{1/2}$ which is the maximum growth rate for inertial instability or for axisymmetric perturbations ($m = 0$). That is to say, in cyclonic vortices, axisymmetric perturbations have the highest growth rate. Nonetheless in anticyclonic vortices, if $-\bar{\omega} < f < -2\bar{\omega}$, then $\eta > 1$; thus growth rate Eq. (2.25) is larger than $(-\Phi)^{-1/2}$. In other words, for anticyclonic vortices with proper η , non-axisymmetric perturbations ($m \neq 0$) can have a larger growth rate than the axisymmetric counterparts.

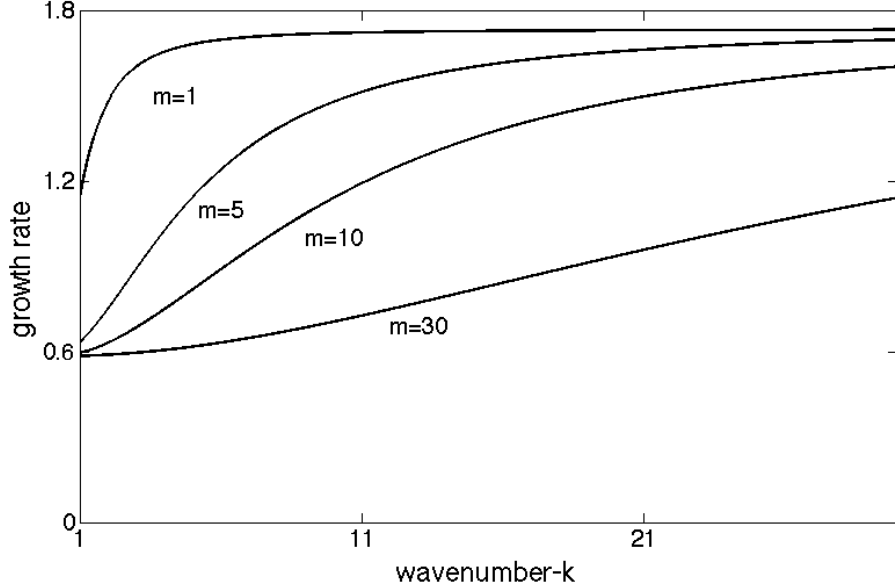


Figure 2.7: Growth rates of 3D instability for different azimuthal and vertical wavenumber pairs (m, k) .

Further based on the growth rate in Eq. (2.25), I can analyze the necessary condition for the 3D instability. If taking $f > 0$, then for cyclonic vortices ($\bar{\omega} > 0$) I have $\eta > 0$; thus it requires $\Phi < 0$ at least for one point in the domain in order to get nonzero σ_i . But for anticyclonic vortices ($\bar{\omega} < 0$), $\Phi < 0$ is not necessary to launch instability because of the uncertainty of the sign of η . For example, if $\eta < 0$ and $\Phi > 0$, nonzero growth rate can still exist for proper wavenumber pairs (m, k) that satisfy $[k^2 + (m/r)^2\eta] < 0$. Hence with background rotation, anticyclonic vortices are more vulnerable to instability than the cyclonic counterparts, since anticyclonic vortices may undergo 3D instability when either $\Phi < 0$ or $\Phi > 0$.

In addition to the above necessary condition, I also obtain another necessary condition shown below. Using equations (2.23a) and (2.23b), I get the equation for the vertical perturbation vorticity. Substituting normal-mode solutions into the

new equation as well as Eq. (2.23d), and taking the real parts, I obtain

$$\frac{d(r\hat{v})}{dr} = \frac{U_0}{\sigma_i} \frac{d\bar{\zeta}}{dr}, \quad (2.26)$$

where U_0 is a nonzero constant. Integrating Eq. (2.26) over $r \in (0, R)$ with boundary condition $\hat{v}(R) = 0$, I attain

$$\frac{U_0}{\sigma_i} \int_0^R \frac{d\bar{\zeta}}{dr} dr = 0. \quad (2.27)$$

Since $U_0 \neq 0$, the above integral has to be zero, yielding the necessary condition, *i.e.*, the radial gradient of basic-state vorticity, $d\bar{\zeta}/dr$, changes sign somewhere. Consequently, the 3D instability in cyclonic vortices has two necessary conditions which are actually the necessary conditions for barotropic and inertial instabilities, respectively. This is not surprising since our stability analysis treats the 3D instability as the combination of barotropic and inertial instabilities. In fact, in order to combine the two kinds of instability, it requires that background flows favor both instabilities and that their growth rates are comparable.

As stated by Gallaire and Chomaz (2003), the 3D instability produces helical structures, each of which is associated with a specific wavenumber pair ($m \neq 0, k \neq 0$). Indeed, an example of 3D instability shown in Fig. 2.8 exhibits such a helical structure related to the wavenumber pair ($m = 2, k = 1$).



Figure 2.8: The helical structure of 3D instability from the target experiment T1, visualized by the isosurface of vertical vorticity equal to 1.

2.4 Joint impacts of instabilities on transport

2.4.1 Evolution of an unstable vortex

In the context of the background presented in section 2.3, I can now identify these instabilities developed in the vortex. Take the target experiment T1 as an example. At the beginning, the vortex undergoes weak inertial instability that generates short-living, vertically stacked overturning cells. Then barotropic instability develops the azimuthal wavenumber-4 mode (Fig. 2.9a) that quickly grows into nonlinear phase, creating four satellite vortices surrounding the central vortex (Fig. 2.9b). Through the vortex merging mechanism which states that two same-signed vorticity regions can merge into one vortex (Melander, Zabusky and McWilliams 1988), the four satellite vortices merges into two larger ones. As the merging proceeds, the central vortex undergoes horizontal stretching (Fig. 2.9c). Next by the vortex axisymmetrization mechanism which expresses that a vortex relaxes

towards axisymmetry as a result of filament generation (Melander, McWilliams and Zabusky 1987), the stretched central vortex rolls up and bonds with the two satellite vortices via spiral vorticity filaments, forming tripolar vortices (Fig. 2.9d). The entire pattern of the tripolar vortices rotates together and remains coherent till the end of simulation. Additionally, the 3D tripolar vortices (Fig. 2.10b) demonstrate the helical structures produced by 3D instability; the helical structures consist of both horizontally propagating and vertically propagating waves. In particular, the helical structure of the central vortex has a reversed winding direction, compared with that of the satellite vortices owing to their opposite-sign vorticity.

Barotropic, inertial and 3D instabilities are all observed in the above example; accordingly, the impacts of instabilities to be presented below are actually produced by the joint actions of these instabilities.

2.4.2 Overturning transport by the secondary circulation

In order to visualize pathways of the overturning transport, I inject a small, low-diffusivity tracer blob within the mid-depth vortex core at the beginning, and track its evolution.

In the control experiment C1, the vertical velocity field is upward within the vortex core and downward outside the core, developing an annulus of downwelling (Fig. 2.11a). Thus, intuitively, tracer is transported upward within the vortex core (Fig. 2.12b). After arriving at the surface, tracer uniformly spreads out of the core and enters into the downwelling annulus (Fig. 2.12c). Then the downwelling carries tracer downward, completing the overturning transport (Fig. 2.12d). The above process is further illustrated via streamlines shown in Fig. 2.14a. The streamline spirals up in the upwelling core and gets into the downwelling annulus where it spirals down.

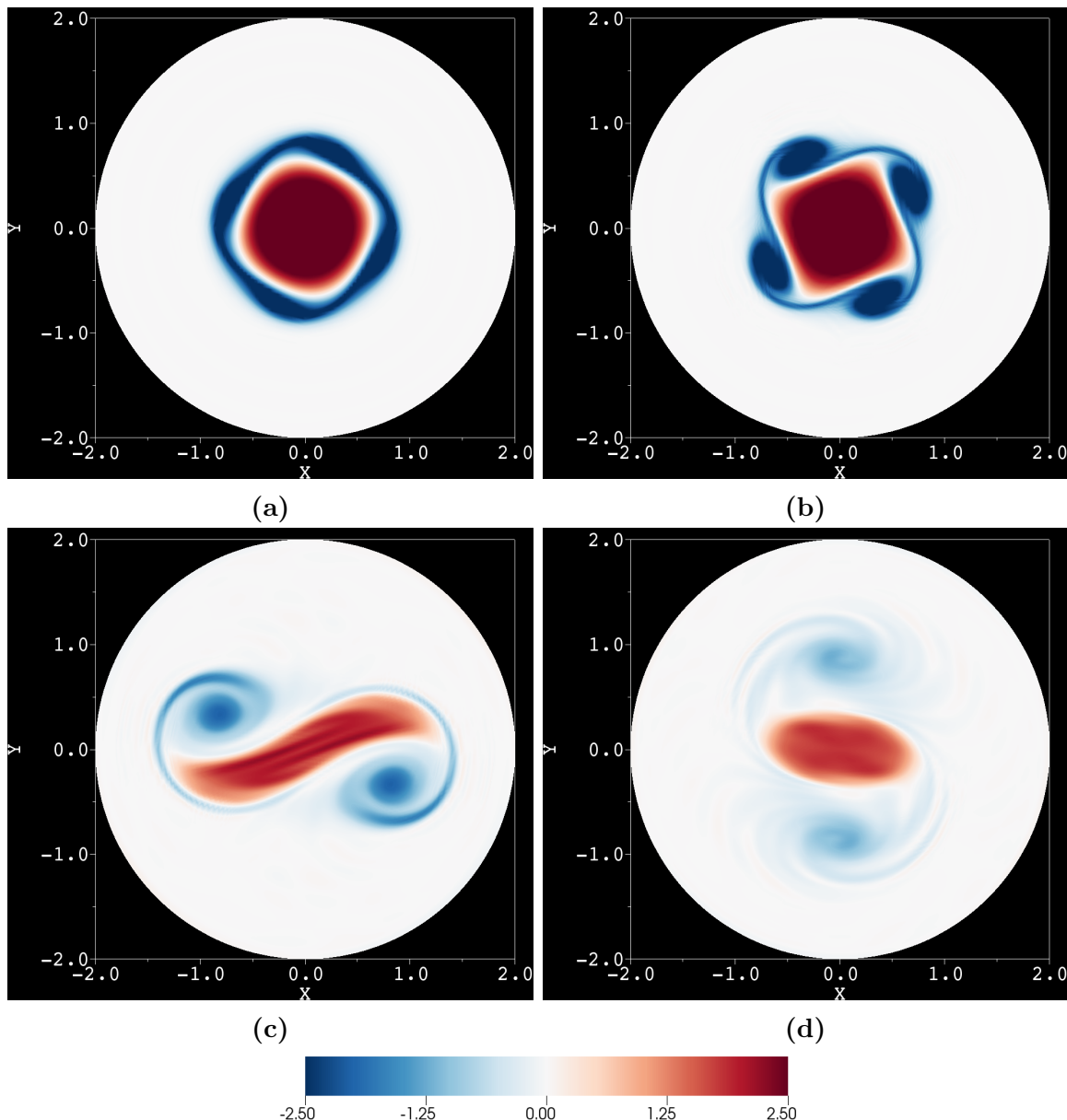


Figure 2.9: Vertical vorticity field at mid-depth horizontal plane in the target experiment T1 at (a) time = 17 (b) time = 19 (c) time = 65 and (d) time = 195.

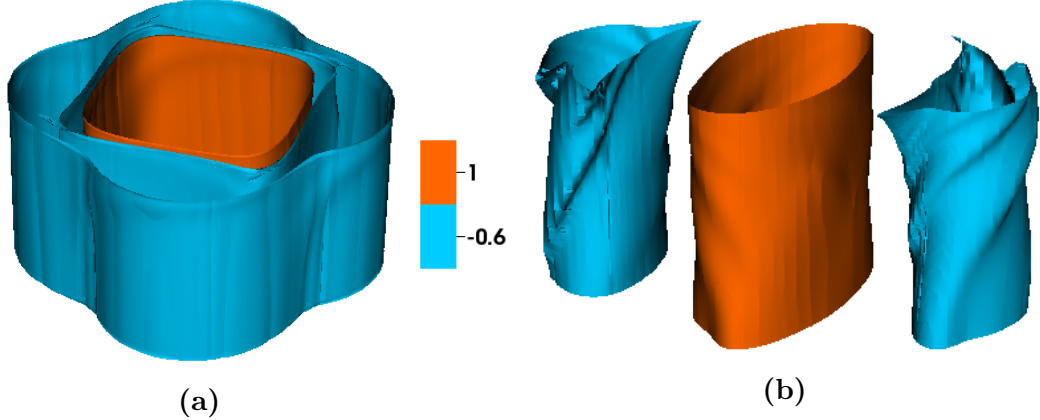


Figure 2.10: 3D structures of vortices, visualized by the isosurface of vertical vorticity, correspond to the vortex shown in (a) Fig. 2.9b and (b) Fig. 2.9d.

In the target experiment T1, instabilities create small, weak downwelling zones settling in the vortex core (Fig. 2.11b), but the upwelling is dominant within the core. Thus, similar to the control experiment C1, the tracer goes upward at the beginning; then it is horizontally stretched (Fig. 2.13b) as the vortex core is suffering stretch (*cf.* Fig. 2.9c). Next due to vortex axisymmetrization, the stretched tracer rolls up, creating spiral filaments (Fig. 2.13c). Tails of the spiral filaments are cut off later and stay at domain corners, being nearly motionless, as shown on Figs. 2.13d–f. After reaching the surface, the tracer disperses out of the central vortex and gets attracted into two surrounding satellite vortices (Fig. 2.13d), within which tracer continues moving down. During the downward motion, the tracer is gradually shaped into two 3D “funnel” structures (Fig. 2.13e) that are confined inside the satellite vortices. When the funnels touch the bottom, the tracer spirals inward and then is carried up by the dominant upwelling inside the central vortex (Fig. 2.13f). Hereafter, the tracer circulates among the central and satellite vortices and completes the overturning transport. This 3D circulation is also demonstrated by streamlines shown in Fig. 2.14b. The two sets of streamline are parallel to each other inside the

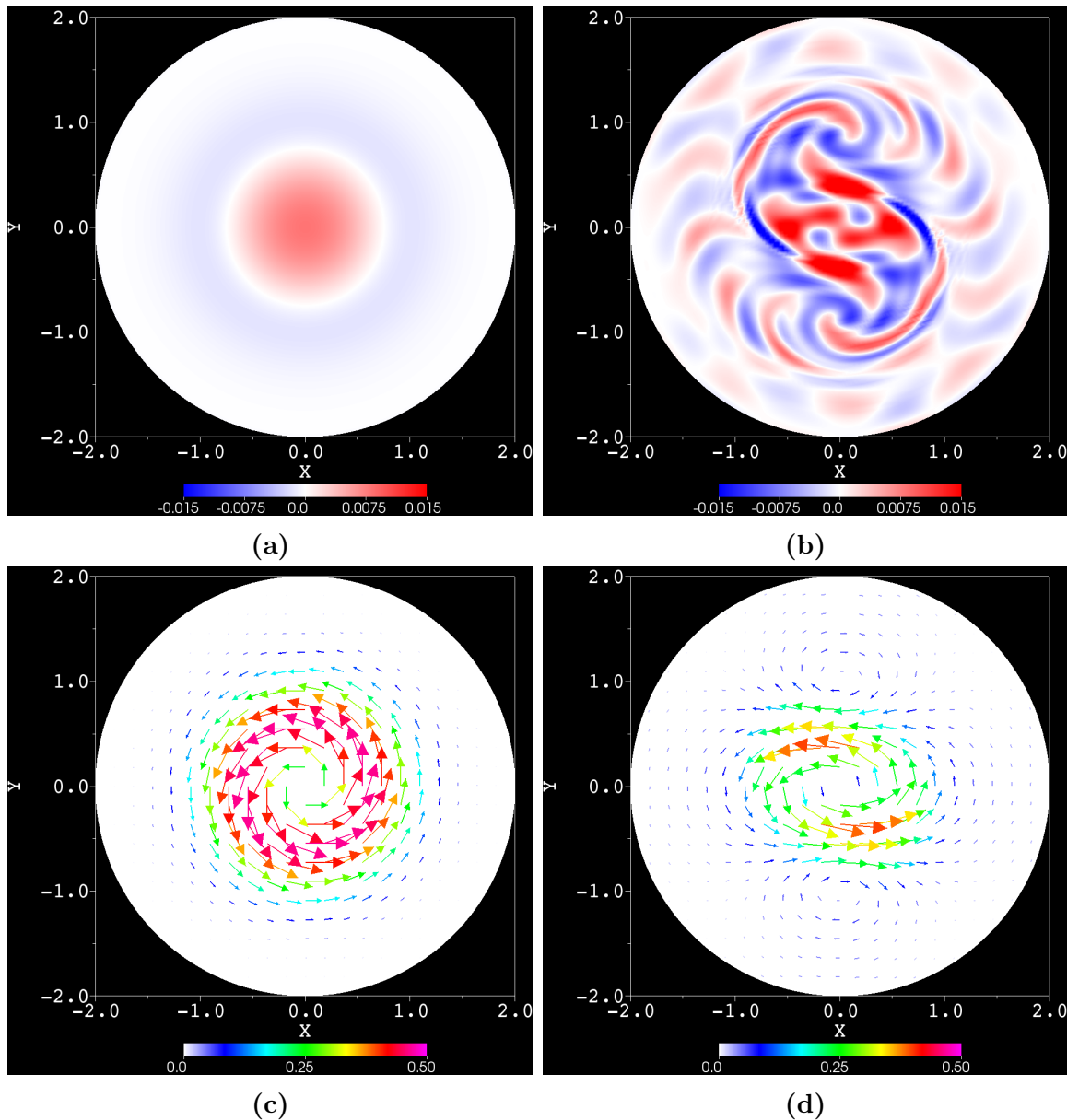


Figure 2.11: (a, b) Vertical velocity fields and (c, d) horizontal velocity vectors at mid-depth horizontal plane at time = 195; color denotes the magnitude of velocity; left column: the control experiment C1; right column: the target experiment T1.

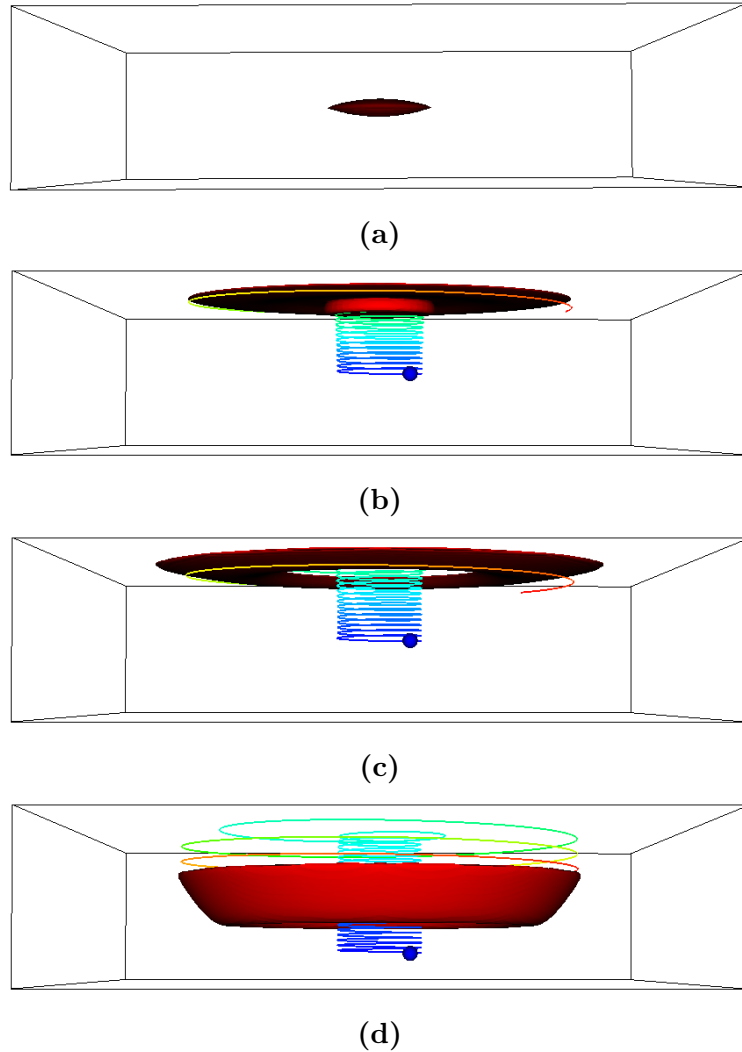


Figure 2.12: Tracer evolution in the control experiment C1, visualized by the tracer isosurface of 0.0006 at (a) time = 0 (b) time = 76 (c) time = 95 and (d) time = 399. A particle trajectory is imposed on (b)–(d) with the blue sphere denoting the initial position of the particle. (Readers may refer to the animation at <http://youtu.be/qm7i0bVv41s>.)

central vortex, but diverge into different satellite vortices after leaving the central vortex.

During the tracer transport, the tracer around edges of vortices quickly diffuses and mixes, implying that vigorous flow stirring (rapid stretching and folding of fluid elements) exists around edges. The finite-time Lyapunov exponent (FTLE) is adopted to test this implication. Briefly, FTLE is the exponential rate of dispersion between particles initially close to each other, after particles being advected by ambient flows for finite time (*e.g.* Haller and Yuan 2000; Shadden, Lekien and Marsden 2005). The larger FTLE represents the faster particle dispersion and also means the stronger flow stirring. Indeed, as shown in Fig. 2.15a, the extremes of FTLE occupy the regions around vortices edges, confirming the vigorous flow stirring around edges. Additionally, vigorous flow stirring accompanies with strong strain rate that can be identified from Okubo-Weiss (OW) field shown in Fig. 2.15b. The definition of OW is $OW = S^2 - \zeta^2$, with the horizontal strain rate $S = [(u_x - v_y)^2 + (v_x + u_y)^2]^{\frac{1}{2}}$ and vertical vorticity $\zeta = v_x - u_y$ in Cartesian coordinates. Therefore, positive OW indicates strong strain rate, which appears around the edges of vortices according to Fig. 2.15b, particularly at the rear end of the major axis of central elliptic vortex.

Furthermore, I investigate the root mean square (RMS) of vertical velocity that reflects the flow's overall ability of vertical motions and overturning transport. In the control experiment C1, vertical velocity manifests decaying oscillations in the early adjustment stage and then gradually reaches an equilibrium (Fig. 2.16). Similarly in the target experiment T1, decaying oscillations appear at the beginning (*cf.* Fig. 2.16). Afterwards (time > 15), instabilities start to grow and increase the magnitude of vertical velocity; however, the magnitude decreases later (60 < time < 110) and then is re-elevated to a quasi-steady state at which the magnitude is twice as much as that of the control experiment C1. On the whole, instabilities increase the

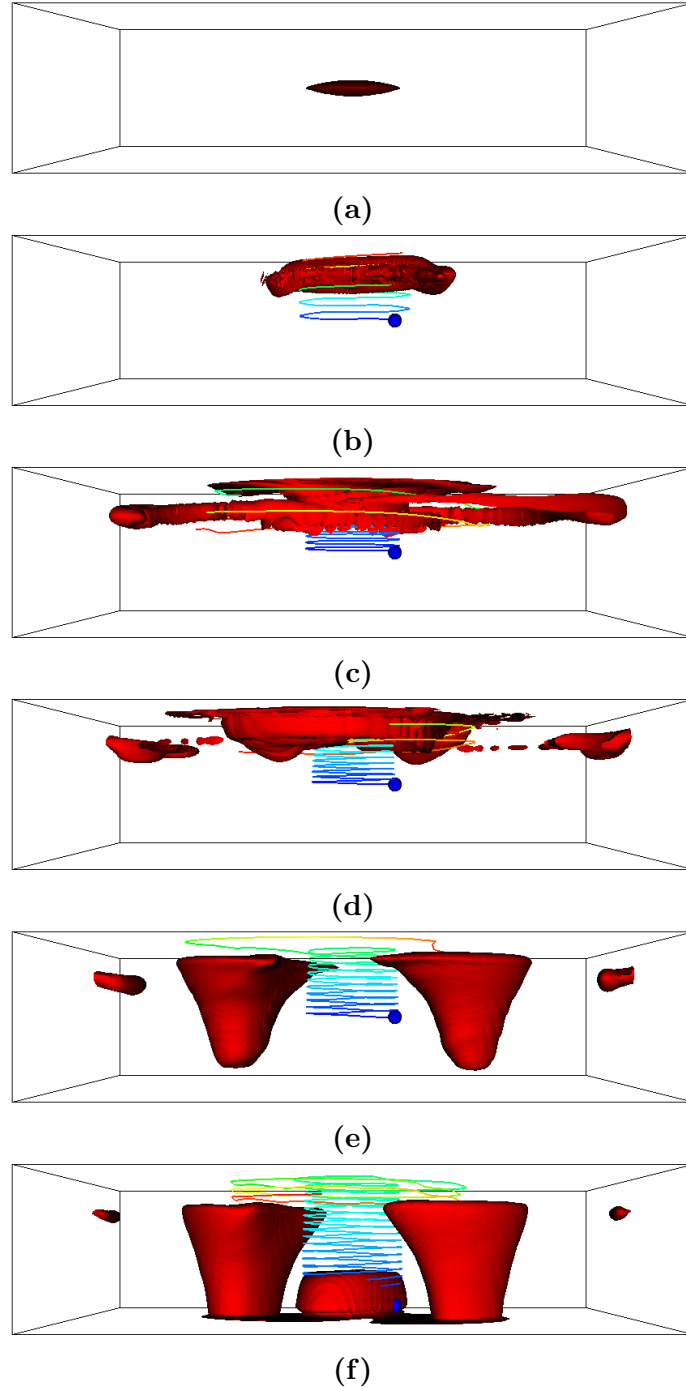


Figure 2.13: Tracer evolution in the target experiment T1, visualized by the tracer isosurface of 0.0006 at (a) time = 0 (b) time = 65 (c) time = 90 (d) time = 116 (e) time = 256 and (f) time = 399. Similar to Fig. 2.12, a particle trajectory is imposed on (b)–(f), too. (Readers may refer to the animation at <http://youtu.be/ZJYpLcSLGSc.>)

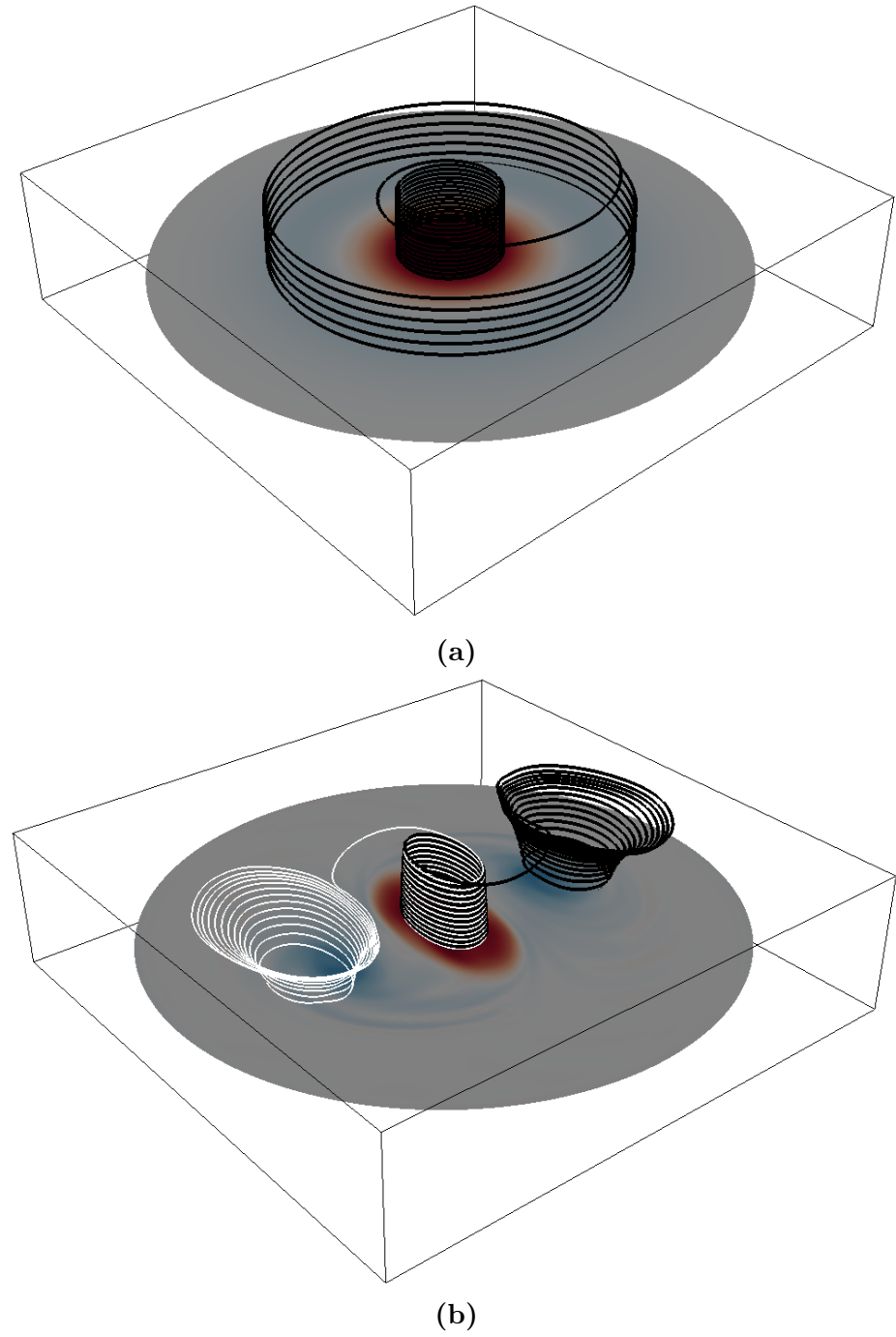


Figure 2.14: Streamlines over a horizontal slice of the vertical vorticity field at mid depth in (a) the control experiment C1 and (b) the target experiment T1 at time = 195. Two sets of streamline are coloured by white and black. Positive (negative) vorticity is coloured by red (blue).

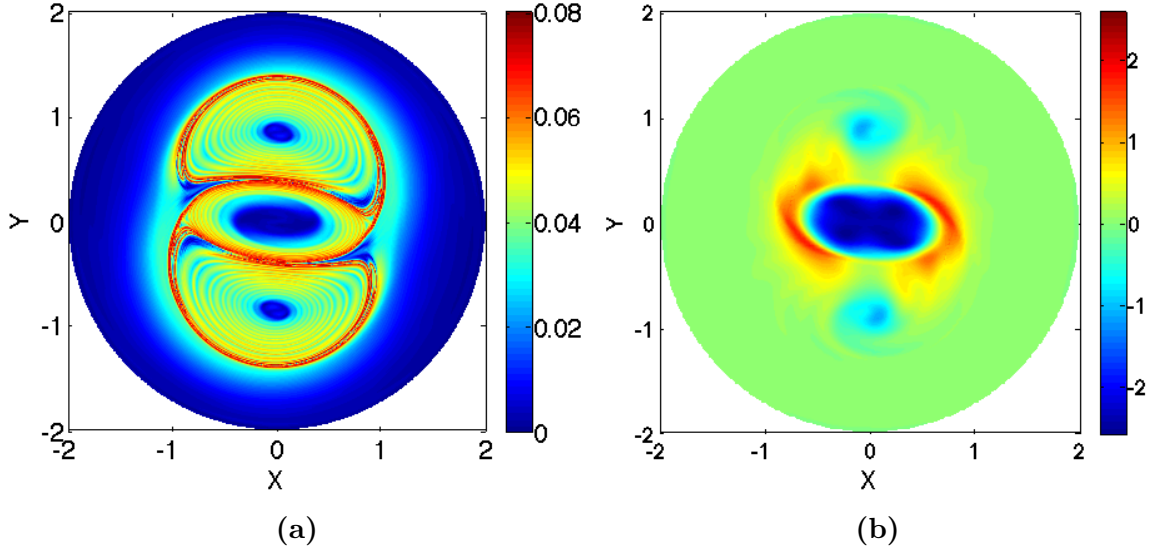


Figure 2.15: (a) FTLE field at mid-depth horizontal plane in the target experiment T1 at time = 195, with trajectories of 1,283,202 particles being integrated for a period of 80 (forward-in-time). (b) Okubo-Weiss field at mid-depth horizontal plane in the target experiment T1 at time = 195.

magnitude of vertical velocity and therefore enhance the overturning transport. The enhanced overturning transport can be verified by comparing the location of tracer blobs in the control and target experiments. Tracer blob in the target experiment T1 has already arrived at the bottom before time = 399 (*cf.* Fig. 2.13f); while in the control experiment C1, tracer blob is still on the way to bottom at time = 399 (*cf.* Fig. 2.12d).

2.4.3 Rates of the vertical exchange and mixing

Now I fill up the entire domain with a low-diffusivity ($Pe = 10^5$) tracer, the initial distribution of which is uniform in the horizontal direction and is linearly stratified in the vertical direction.

By defining the rate of vertical exchange and the rate of mixing, I can quantify the instabilities impacts. The rate of vertical exchange is estimated by the vertical gradient of vertical tracer flux, *i.e.* $\partial(wC)/\partial z$ (of dimension $[C][T^{-1}]$) where w is

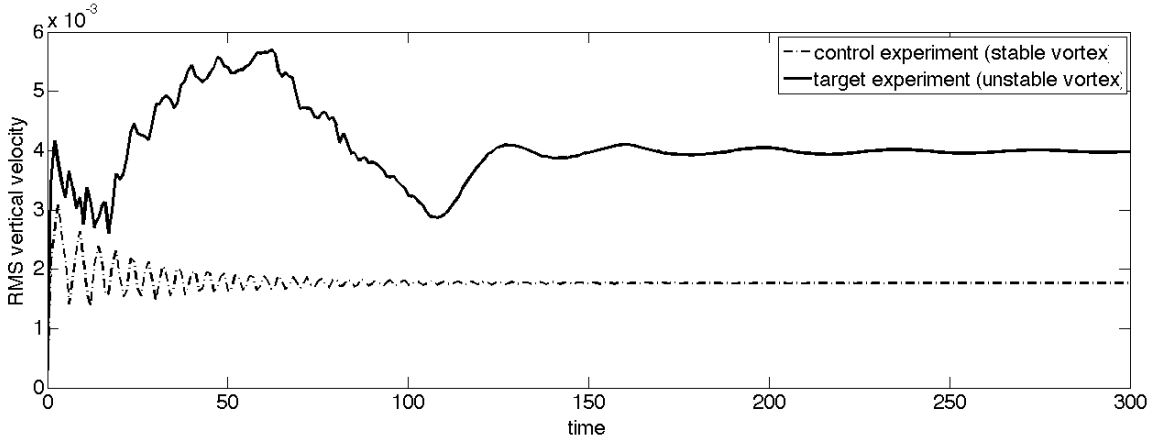


Figure 2.16: Evolution of the RMS vertical velocity in the control experiment C1 and target experiment T1.

vertical velocity and C denotes tracer field. In the control experiment C1, large absolute gradients are located within the vortex core and downwelling annulus (Fig. 2.17), which are the zones of rapid vertical exchange. In the target experiment T1, however, large absolute gradients occupy the edges of vortices, rather than the core, as well as the spiral filaments (*cf.* Fig. 2.17). This implies that instabilities create rapid vertical exchange regions concentrated along the vortex edges. Besides, according to Fig. 2.17, the vertical exchange rate in the target experiment T1 is one order of magnitude higher than that in the control experiment C1.

The rate of mixing is defined as $\Gamma(t) \equiv \left| \frac{1}{\Delta t} \log \left[\frac{\bar{C}^2(t)}{\bar{C}^2(t_0)} \right] \right|$, where $\bar{C}^2(t)$ and $\bar{C}^2(t_0)$ represent the domain-averaged square tracer field at time t and t_0 , and $\Delta t = t - t_0$. During the early period of instability growth (Fig. 2.18a), the mixing rate increases by $(\Gamma_{tar} - \Gamma_{con})/\Gamma_{con} = 140\%$ (with $\Gamma_{tar} = 1.4 \times 10^{-4}$ in the target experiment and $\Gamma_{con} = 5.8 \times 10^{-5}$ in the control experiment). The increase of mixing rate is contributed by the larger tracer gradient that is confirmed by the RMS gradient of tracer field shown in Fig. 2.18b.

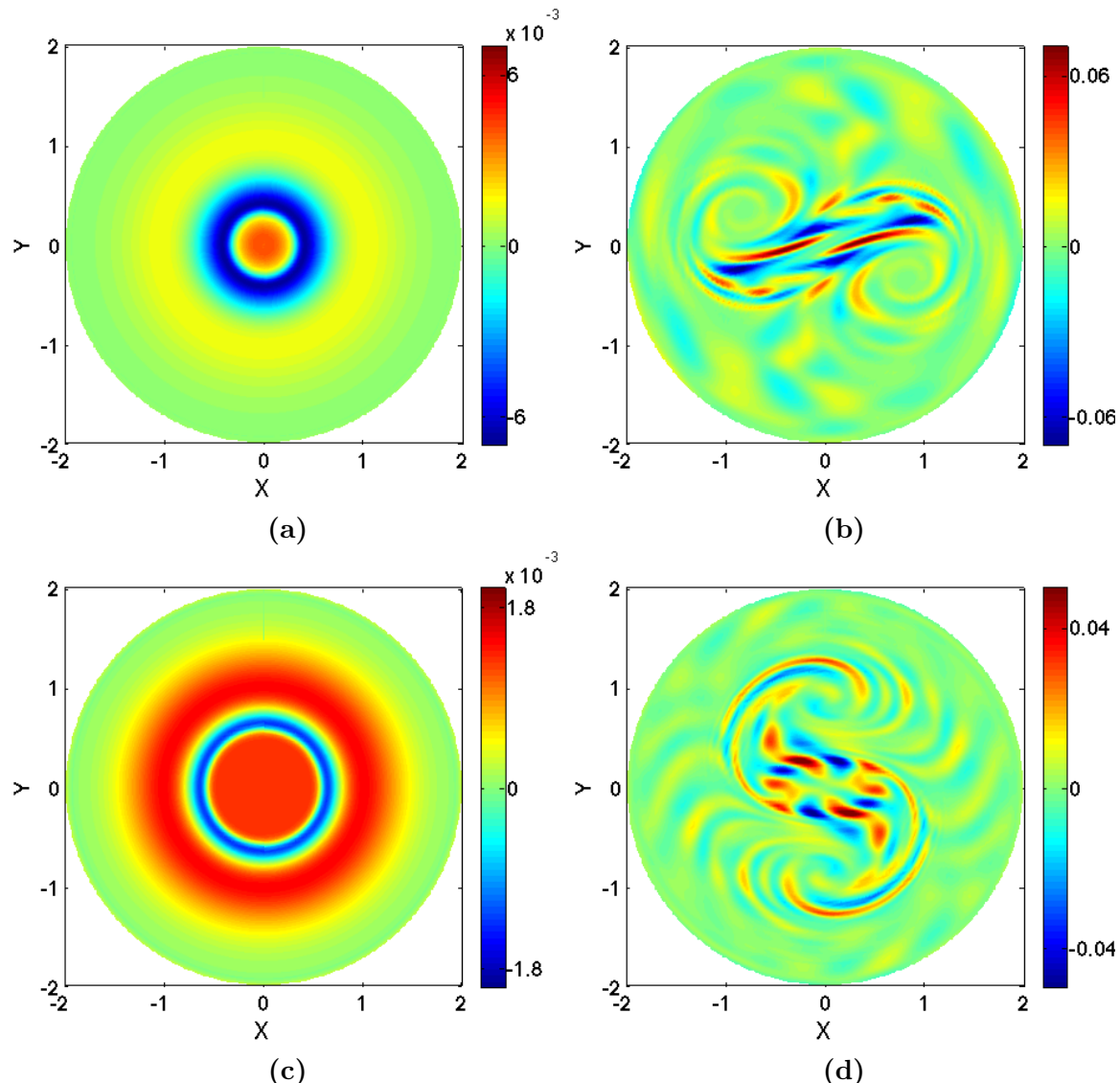


Figure 2.17: Vertical gradients of the vertical tracer flux across mid-depth horizontal plane at (a, b) time = 65 and (c, d) time = 195; left column: the control experiment C1; right column: the target experiment T1.

Since the mixing rate is also depend on tracer diffusivity, I inject tracers with different diffusivities, namely $Pe = 10^4$ and $Pe = 10^6$, to examine the dependence. Indeed, as shown in Fig. 2.19, the mixing rate changes strikingly with tracer diffusivity; for example, in the early period of instability growth, the mixing rate increase by 40% for the higher-diffusivity tracer (with $\Gamma_{con} = 5.0 \times 10^{-4}$ and $\Gamma_{tar} = 7.0 \times 10^{-4}$) and by 1100% for the lower-diffusivity tracer (with $\Gamma_{con} = 5.8 \times 10^{-6}$ and $\Gamma_{tar} = 7.0 \times 10^{-5}$).

2.4.4 A new thinking on the energy transfer

The kinetic energy wavenumber spectrum is used to check the energy transfer, and is computed as follows: sample the velocity field along the azimuthal direction which is the periodic direction of the cylindrical domain, calculate the energy spectrum, and then average the spectrum over different depths and radii in the fluid interior.

For both the control and target experiments, the initial vortices are purely axisymmetric, which theoretically means the initial flow contains the only mode of azimuthal wavenumber-0; hence, energy has the only peak at wavenumber-0 and is almost zero at other wavenumbers. The vortex in the control experiment C1 is stable and stays axisymmetric throughout the simulation, and thus it is not surprising that the final-state energy spectrum shown in Fig. 2.20a has almost identical shape to the initial, but with reduced energy level due to dissipation. The fact that final-state energy remains small at nonzero wavenumbers indicates that energy is directly dissipated by friction acting on large scales through non-local interactions (Vallis 2006), without being cascaded into inertial ranges of energy spectrum.

On the other hand, instabilities developed in the target experiment change the flow into non-axisymmetric by generating disturbances of nonzero azimuthal wavenumbers, and increase energy at nonzero wavenumbers. Consequently,

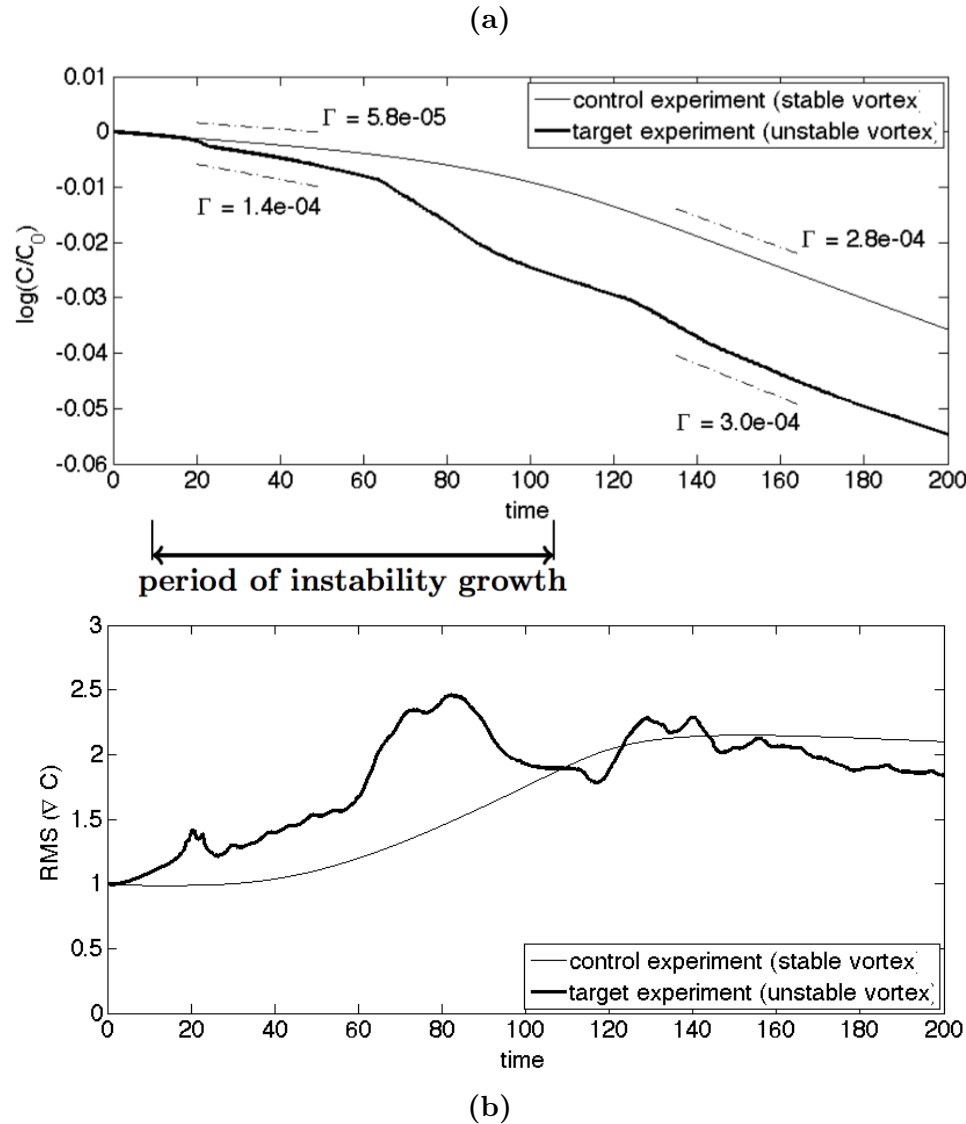


Figure 2.18: (a) Evolution of the domain-averaged tracer field with mixing rate Γ being labelled; (b) evolution of the RMS gradient of tracer fields. The period of instability growth is labelled.

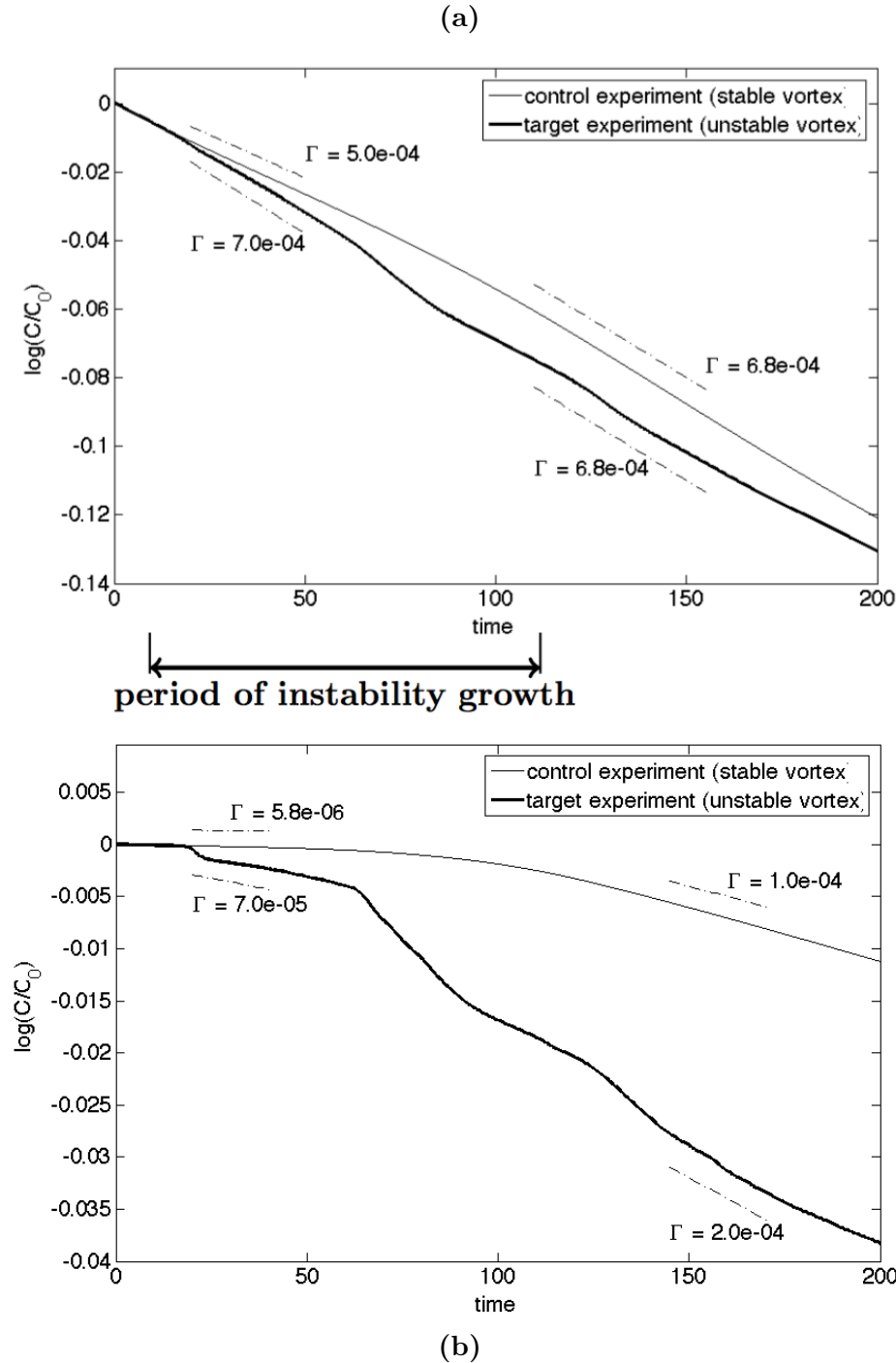


Figure 2.19: Evolution of the domain-averaged tracer field with mixing rate Γ being labelled for the (a) higher diffusivity, $Pe = 10^4$ and (b) lower diffusivity, $Pe = 10^6$. The period of instability growth is labelled. (Note the different scaling of the panels.)

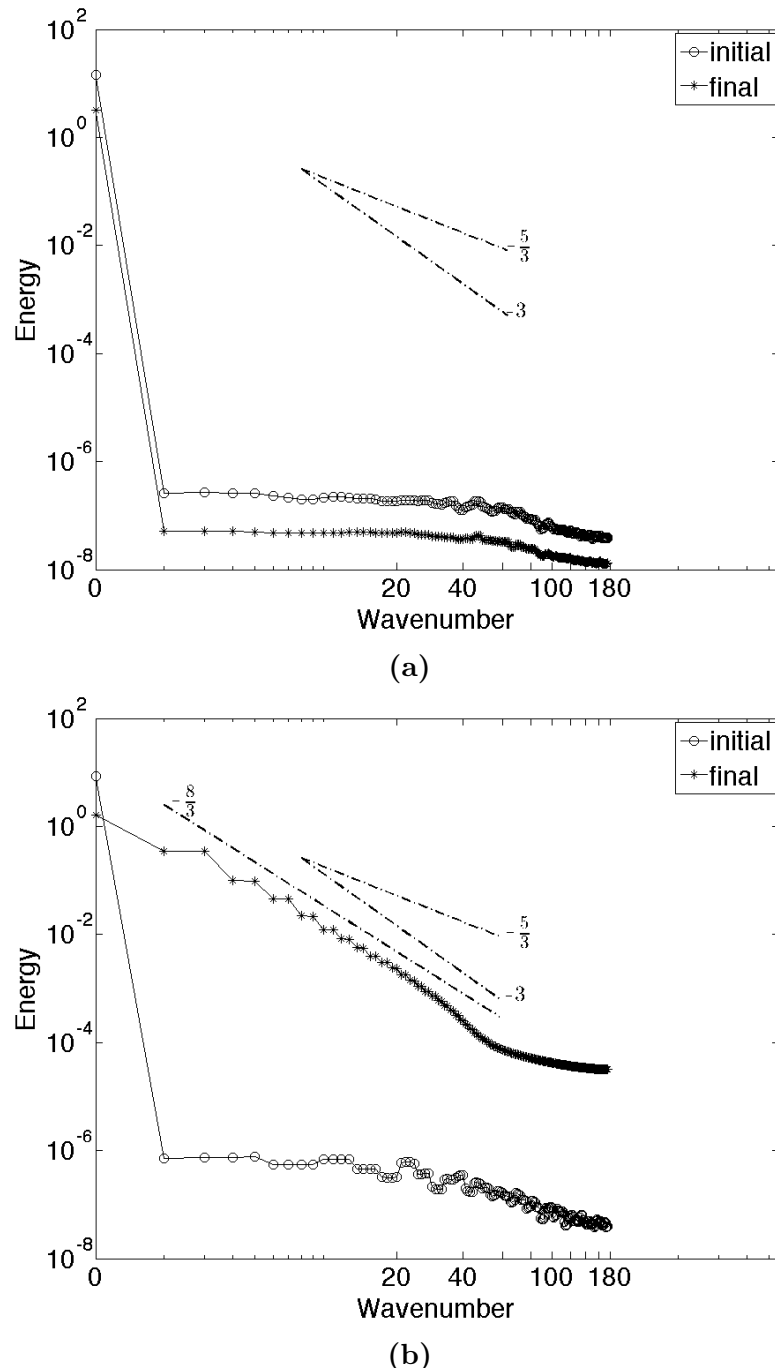


Figure 2.20: Kinetic energy wavenumber spectrum at the initial and final state of the flow in (a) the control experiment C1 and (b) the target experiment T1.

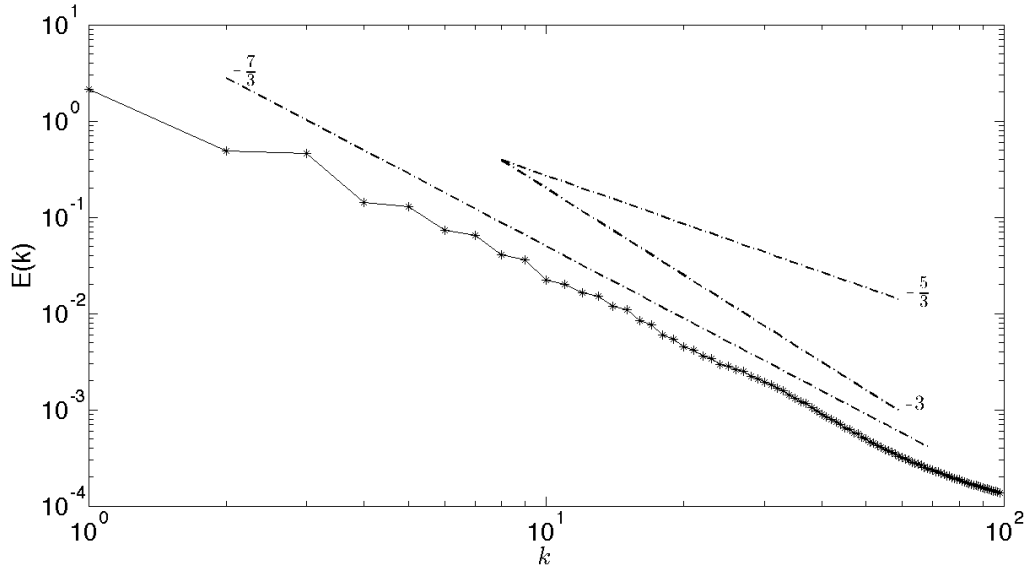


Figure 2.21: Kinetic energy wavenumber spectrum at the final state of the flow in the target experiment T3.

instabilities boost local nonlinear interactions, generating a broader wavenumber spectrum. I find that the final-state energy spectrum has a wavenumber power of $k^{-8/3}$ at the inertial range for the target experiment T1 (Fig. 2.20b) and of $k^{-7/3}$ for the target experiment T3 (Fig. 2.21).

I propose a heuristic explanation for the above mentioned non-classic power-law regimes of $k^{-8/3}$ and $k^{-7/3}$. Assume that through local nonlinear interactions, the quantity being transferred within the inertial range is $E^{1-\alpha}Z^\alpha$, where E is kinetic energy, Z is enstrophy and α measures the isotropy of turbulence at different wavenumbers. Postulate $\alpha \in [0, 1]$ with $\alpha = 0$ implying fully 3D isotropic turbulence and $\alpha = 1$ indicating purely 2D turbulence. Therefore, the change of α from 0 to 1 represents the transition of turbulence from 3D to 2D; that is, α bridges the gap between 3D and 2D turbulence. Denoting ξ as the transfer rate of $E^{1-\alpha}Z^\alpha$, and using dimensional analysis, I obtain the kinetic energy spectrum

$$E(k) \propto \xi^{2/3} k^{-(4\alpha+5)/3}. \quad (2.28)$$

When $\alpha = 0$, the above spectrum recovers the energy-downscale-cascade regime ($k^{-5/3}$) of fully-developed, homogeneous, isotropic 3D turbulence, predicted by Kolmogorov (1941) who assumed the spectrum depends only on the energy transfer rate and wavenumber. When $\alpha = 1$, it recovers the enstrophy-downscale-cascade regime (k^{-3}) of purely 2D turbulence, predicted by Kraichnan (1967) who supposed the spectrum relies only on the enstrophy transfer rate and wavenumber. Moreover, when $\alpha = 3/4$ and $1/2$, it explains the power-law regime of $k^{-8/3}$ and $k^{-7/3}$ observed in Figs. 2.20b and 2.21, respectively. Further, analogous to the definitions of energy flux $\Pi(k)$ and enstrophy flux $Y(k)$ across wavenumber k , *i.e.*

$$\Pi(k) \equiv \int_k^\infty T(k') dk' , \quad (2.29a)$$

$$Y(k) \equiv \int_k^\infty k'^2 T(k') dk' , \quad (2.29b)$$

where $T(k')$ represents the rate of energy transfer owing to nonlinear interactions (Boffetta and Ecke 2012), I can define the flux of $E^{1-\alpha} Z^\alpha$, denoted by $A(k)$, as

$$A(k) \equiv \int_k^\infty k'^{2\alpha} T(k') dk' . \quad (2.30)$$

2.5 Discussion

2.5.1 Linear instability analysis of geophysical vortices

The analysis of barotropic instability showed that wavenumber-1 instability is neutral in purely 2D flows (Schubert *et al.* 1999; Terwey and Montgomery 2002). Nonetheless, laboratory experiments (Smith and Rosenbluth 1990) and numerical simulations (Nolan and Montgomery, 2000) showed that wavenumber-1 instability has algebraic growth rate; later by numerical simulations, Nolan and Montgomery

(2001) pointed out that wavenumber-1 instability may become exponentially unstable in a shallow-water system. In this study, I prove that wavenumber-1 instability can exponentially grow in shallow-water systems. Moreover, the unstable zones of wavenumber-1 instability change remarkably with Rossby radius of deformation; however, other wavenumber- m ($m = 2, 3, 4, \dots$) instabilities only alter a little (*cf.* Fig. 2.4). Therefore, wavenumber-1 instability is quite sensitive to the deformation radius, agreeing with the result of Flierl (1988).

Wavenumber-1 instability introduces geometrical asymmetry into flows by shifting the vortex core out of the symmetric center (*cf.* Fig. 2.5). This kind of asymmetry is also observed in laboratory experiment (van de Konijnenberg *et al.* 1999, their Fig. 5) and is identified from the reflectivity map of hurricane's inner core (*e.g.* Reasor *et al.* 2000). Further, wavenumber-1 instability is claimed to be related with the trochoidal motions of hurricane tracks (Nolan and Montgomery 2001). Analogously in ocean eddies that undergo wavenumber-1 instability, I expect that the asymmetry can be observed, for example, in ocean color images by the aid of high-resolution remote sensing technology. Also, tracks of these eddies may exhibit the wobbling motions like the hurricane tracks.

In the analysis of inertial instability (*cf.* Section 2.3.2), I discuss the selective stabilization which now is used to interpret the vorticity skewness of submesoscale turbulence. According to ship-based surveys, vorticity skewness of oceanic submesoscale turbulence is positive (towards cyclonic) in the upper ocean mixed layer and decreases to zero below the mixed layer (Shcherbina *et al.* 2013). Based on the selective stabilization, submesoscale anticyclonic vortices (of characteristic $Ro \sim O(1)$) are vulnerable to inertial instability under the Earth's rotation, whereas cyclonic vortices tends to be stabilized by the Earth's rotation, causing vorticity skewness towards cyclonic. Below the upper ocean mixed layer, strong density

stratification prohibits inertial instability (Kloosterziel *et al.* 2007) and consequently anticyclonic vortices survive. Hence below the mixed layer, oceanic environments do not prefer to stabilize cyclonic or anticyclonic vortices; in other words, the vorticity skewness is about zero.

In analyzing the 3D instability which is the combination of barotropic and inertial instabilities from the perspective of normal-mode analysis, I define a new formula of growth rate. In terms of this formula, a new insight is delivered to the argument on whether the non-axisymmetric/asymmetric perturbations can possess higher growth rates than that of the axisymmetric/symmetric ones. It was argued in swirling flows that axisymmetric perturbations have the highest growth rate at large axial/vertical wavenumbers by Gallaire and Chomaz (2003) using the direct numerical simulation of linear impulse response and by Billant and Gallaire (2005) using WKB approximation. In a jet flow study, Griffiths (2008) argued a similar conclusion which is symmetric perturbations possessing the highest growth rate at large vertical wavenumbers, by means of Rayleigh-Schrödinger perturbation analysis. In contrast, the opposite result was claimed in the study of the Bickley jet's stability; that is, asymmetric perturbations have the highest growth rate at a certain range of vertical wavenumbers (Bouchut, Ribstein and Zeitlin 2011; Ribstein, Plougonven and Zeitlin 2014). Here I suggest that the above problem should be considered separately in the context of cyclonic and anticyclonic vortices (*cf.* Section 2.3.3), at least in swirling flows. Hence, our conclusion is divided into two situations, *i.e.* cyclonic and anticyclonic vortices. In cyclonic vortices, axisymmetric perturbations have the highest growth rate; and in anticyclonic vortices, with the proper combination of angular velocity $\bar{\omega}$ and Coriolis parameter f that makes $\bar{\omega}/(2\bar{\omega} + f) > 1$, non-axisymmetric perturbations can have a larger growth rate.

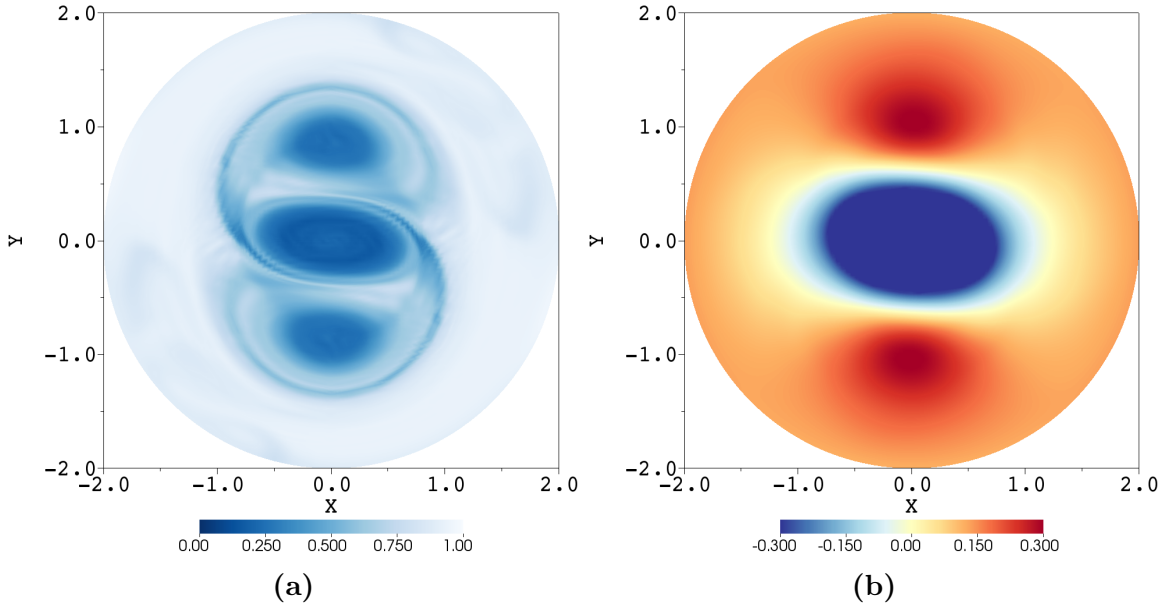


Figure 2.22: (a) Temperature field and (b) pressure field at the surface in the target experiment T1 at time = 195.

2.5.2 Nonlinear evolution and transport in geophysical vortices

During the vortex evolution, I find that tracer fields tend to exhibit patterns similar to the underlying vorticity fields. For instance, temperature and pressure fields shown in Fig. 2.22 resemble the corresponding vorticity field shown in Fig. 2.9d. In fact, measuring vorticity can be quite challenging for ocean observations, while the remote sensing can readily provide estimates of the sea surface temperature (SST), sea surface height, chlorophyll, *etc.* Therefore, the pattern similarity between the vorticity field and tracer field (*e.g.* SST and chlorophyll) is a useful property that can help identify the united system of central and satellite vortices in the ocean. Observational examples of these united vortices were given by Pingree and Le Cann (1992, their Fig. 2) in SST and by Stapleton *et al.* (2002, their Fig. 2) in chlorophyll.

The tracer motion in the stable vortex (*cf.* Fig. 2.12) depicts a traditional picture of the secondary circulation within a cyclonic ocean eddy; that is, water is uplifted in the eddy core and is pushed down at the eddy edges. If ambient surface currents exist as is in the oceanic environments, some of the uplifted water from the eddy core might be entrained into and carried away by these surface currents. Previous studies mainly focus on the upwelling branch of this secondary circulation. One reason is that the upwelling brings nutrients into euphotic zones for plankton growth, whereas the downwelling does not excite much ecosystem response (*e.g.* Mizobata *et al.* 2002; McGillicuddy *et al.* 2007; Klein and Lapeyre 2009). Here our results demonstrate some interesting features of the downwelling as a result of instabilities. For example, the downwelling shifts into the satellite eddies that are generated around the original eddy edges by instabilities. Subsequently, unexpected 3D pathways of transport, *e.g.* the funnels shown in Fig. 2.13e, are created, replacing the former downwelling annulus that is regarded as a traditional transport pathway.

Further, thinking of the material belt defined by Haller and Beron-Vera (2013) in a 2D black-hole vortex as the boundary that prevents material from leaking out of the vortex, I conclude that such material belts may also exist in the interior of 3D vortex, since material exchange between the central and satellite vortices actually take place near the 3D vortex surface and bottom, not in the interior (*cf.* Figs. 2.13e&f and 2.14b). Consequently, instabilities break the material belts near the 3D vortex surface and bottom, create new pathways of material exchange between the central and satellite vortices, and translate the exchange immediately into 3D regime. In this way, a family of vortices operate together in order to complete the 3D secondary circulation within this system. To our knowledge, it is the first time that this kind of cooperation among vortices has been discovered. Although previous studies found satellite vortices created by instabilities (*e.g.* Kloosterziel and van Heijst

1991; Carnevale and Kloosterziel 1994; Schubert *et al.* 1999), the 2D kinematics and dynamics, rather than the 3D circulation, were the major concern. Besides, in order to observe a complete 3D overturning transport, the family of central and satellite vortices has to remain coherent for 10 or more eddy turnover time in our experiment. In extending the results of idealized numerical experiments to oceanic situations, the main implication is the possibility of the existence of such complex 3D pathways for material exchange among eddies in close proximity. Indeed, such family of eddies has been captured by satellite images (*e.g.* Pingree and Le Cann 1992; Stapleton *et al.* 2002) and hopefully in the future, I can track the material exchange in these eddy families to verify this 3D pathways of transport.

The RMS vertical velocity can measure the overall ability of overturning transport by the secondary circulation. As a whole, instabilities increase the magnitude of vertical velocity; however, at a certain stage of instability growth, *e.g.* $60 < \text{time} < 110$ in the target experiment T1 shown in Fig. 2.16, the magnitude is reduced. In fact, at this stage vortex is suffering horizontal stretching (*cf.* Fig. 2.9c), which greatly depresses the upwelling in the central vortex core due to its horizontal expansion; consequently, the magnitude of vertical velocity decreases. After the tripolar vortices have formed, the upwelling is recovered and instabilities are saturated. Hence, the magnitude of vertical velocity increases again and reaches a quasi-steady state.

Some field observations showed that strong vertical exchanges appear around the edges of mesoscale and submesoscale eddies, other than within the cores. This phenomenon has been explained by resorting to the presence of frontal instability along the periphery of eddies (*e.g.* Strass 1992; Lima, Olson and Doney 2002; Mizobata *et al.* 2002; Lapeyre and Klein 2006; Capet *et al.* 2008a; Klein and Lapeyre 2009). Yet, our target experiments with homogeneous-density fluid show that without density stratification (thus no frontal instability), large rates of vertical

exchange still exist around edges (*cf.* Figs. 2.17b&d). This result indicates that the instabilities can also create strong vertical exchanges around edges, in addition to the frontal instability.

As for mixing, I find that instabilities increase mixing rates, particularly for low-diffusivity tracers. This finding is reasonable since instabilities contribute to vigorous flow stirring that favors the generation of tracer filaments. The filaments amplify the gradient of tracer field (*cf.* Fig. 2.18b, during the period of instability growth). Large gradients of tracer field then accelerate the tracer mixing. Thus, throughout the above successive process, I can conclude that instabilities increase mixing rates. In addition, the filaments generation is of special importance to low-diffusivity tracers for mixing, unlike high-diffusivity tracers that can quickly mix, even without filaments generation, owing to their high molecular diffusion. Therefore, instabilities are more important for the mixing of low-diffusivity tracers than high-diffusivity tracers. In oceanic environments, heat diffusivity is two orders of magnitude higher than salinity diffusivity; therefore, I infer that instabilities increase salinity mixing more efficiently than heat mixing.

I observe non-classic power-law regimes of energy spectrum (*e.g.* $k^{-8/3}$ and $k^{-7/3}$); in order to interpret the non-classic regimes, I propose a new spectrum of $E(k) \propto \xi^{2/3} k^{-(4\alpha+5)/3}$, by assuming the quantity of $E^{1-\alpha} Z^\alpha$ being transferred between scales (with E and Z being energy and enstrophy). In addition, another non-classic power-law regime of k^{-2} was discovered in laboratory rotating turbulence (Baroud, Plapp, She and Swinney 2002) and in oceanic submesoscale turbulence (Capet *et al.* 2008b; Shcherbina *et al.* 2013). In our proposed spectrum, the k^{-2} gives $\alpha = 1/4$, implying that oceanic submesoscale turbulence is neither fully 3D ($\alpha = 0$) nor purely 2D ($\alpha = 1$). Moreover, a special case is $\alpha = 1/2$ such that $E^{1/2} Z^{1/2}$ may be interpreted as helicity (velocity-vorticity-correlations); that is, helicity is transferred

between scales. Indeed, it was claimed that helicity cascade can lead to the non-classic power-law regime in rotating turbulence (*e.g.* Brissaud *et al.* 1973; Bershadskii, Kit and Tsinober 1993; Chakraborty 2007; Mininni and Pouquet 2009).

Furthermore, for the turbulence governed by N-S equations under stochastic power-law forcing, the renormalization group (RG) theory predicts an energy spectrum similar to our proposed one. The RG spectrum is given by $E(k) \propto k^{1-4\epsilon/3}$, where ϵ is the power of the forcing spectrum (*e.g.* Fournier and Frisch 1983; Yakhot and Orszag 1986; Smith and Woodruff 1998). If ϵ is replaced by $(\alpha + 2)$, then the wavenumber power in RG spectrum is identical to that in our spectrum.

The present study contains several obvious simplifications that are introduced in order to deduce clear results and make this an incremental step towards investigation of the complex structure of real-world ocean eddies. Of particular interest for further studies are two factors, the effects of density stratification and small aspect ratios, that can create a significant anisotropy (in terms of horizontal and vertical velocities and circulation time scales) in the system, as well as generating new phenomena, such as internal gravity waves and frontal instabilities. The aspect ratio used here is relevant to the eddies in the upper ocean mixed layer and shallow coastal waters; however, smaller aspect ratios that are more realistic for deep-water oceanic environments also need to be pursued. In fact, in the rotating and stratified oceanic environment, quasi-geophysical flows tend to exhibit aspect ratios of order f/N_b ($\sim 10^{-2}$, with N_b being the buoyancy frequency).

Chapter 3

Spiral inertial waves

3.1 Overview

By simulating an initially-unstable geophysical vortex in a cylindrical domain, I discover a special kind of inertial waves that are emitted from the vortices in a spiral manner; hence, I refer to them as spiral inertial waves (SIWs). In fact, spiral waves have been reported in studies of inertia-gravity wave radiation (*e.g.* Schecter and Montgomery 2006; Viúdez 2006, 2007; Schecter 2008; Sugimoto *et al.* 2015), but for inertial waves, I believe it is the first time that the spiral structures have been discovered. It is worth mentioning that gravity waves are removed from our numerical simulations, because of the conditions of homogeneous density, rigid lid and flat bottom.

This chapter is organized as follows. The numerical model is described in section 3.2. The emissions of SIWs are displayed in section 3.3.1. Parameter-sweep experiments listed in section 3.3.2 show the dependence of SIWs on Rossby numbers. In section 3.3.3, I extend the theory of Lighthill-Ford radiation, and propose an indicator for the emission of inertial waves. The effects of SIWs on material dispersion

are investigated in section 3.3.4. Finally, I summarize and discuss the main results in section 3.4.

3.2 Numerical model

SIWs are simulated with NEK5000, which is a numerical solver for Navier-Stokes equations based on the spectral element method (*e.g.* Patera 1984; Fischer 1997). NEK5000 has been used in studying geophysical flows, including ocean mixed-layer instabilities (*e.g.* Özgökmen *et al.* 2011; Özgökmen *et al.* 2012), chaotic advection inside an ocean eddy (Pratt *et al.* 2014; Rypina *et al.* 2015) and effects of instabilities on 3D material transport within an ocean eddy (Wang and Özgökmen 2015).

NEK5000 solves the following dimensionless equations of motion:

$$\frac{\partial \mathbf{u}}{\partial t} + (\mathbf{u} \cdot \nabla) \mathbf{u} = -\nabla p - \frac{1}{Ro} \hat{\mathbf{k}} \times \mathbf{u} + \frac{1}{Re} \nabla^2 \mathbf{u} , \quad (3.1a)$$

$$\nabla \cdot \mathbf{u} = 0 . \quad (3.1b)$$

The Rossby number is defined as $Ro = U/(fL)$, where U and L are the characteristic scales of horizontal velocity and horizontal length; $f = 2\Omega$ is the Coriolis parameter, with Ω being the angular velocity of the background rotation. In the following experiments of vortex, I choose the maximum azimuthal velocity and the vortex radius as the U and L , respectively; for all experiments, the U and L are similar, and therefore Ro is mainly determined by f . The Reynolds number is given by $Re = UL/\nu$, where ν is the kinematic viscosity. $\mathbf{u} = (u, v, w)$ is the relative velocity measured in the rotating frame, and p is the pressure. $\hat{\mathbf{k}}$ is the unit vector in the vertical direction, and operator $\nabla = (\frac{\partial}{\partial x}, \frac{\partial}{\partial y}, \frac{\partial}{\partial z})$. In addition, NEK5000 integrates

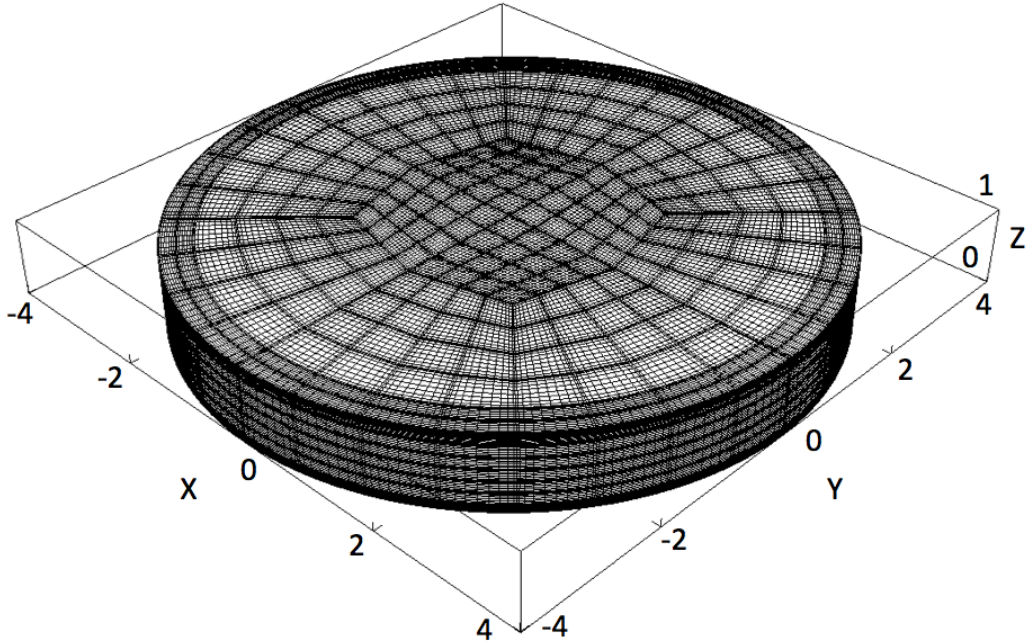


Figure 3.1: The cylindrical domain used in the numerical experiments.

the advection-diffusion equation (3.2) for the passive scalar (tracer):

$$\frac{\partial C}{\partial t} + (\mathbf{u} \cdot \nabla)C = \frac{1}{Pe} \nabla^2 C , \quad (3.2)$$

where $Pe = UL/\kappa$ is the Péclet number and κ is the diffusivity of passive scalar C .

The numerical domain (Fig. 3.1) is a cylinder with radius $R = 4$ and height $H = 1$. The cylinder is filled with homogeneous fluid, which is in solid-body rotation with an angular velocity of Ω about its central axis. Instantly at time = 0, a barotropic vortex is initialized in the center of the domain. The initial vortex has two types of vortical flows (Fig. 3.2) initialized by Eq. (3.3); Wang and Özgökmen (2015) investigated the stability of the two types of flows at different parameter (Ro, Re) regimes. At proper parameters (Ro, Re), the vortex defined by Eq. (3.3a) favors instabilities, producing a family of non-axisymmetric vortices; yet, the vortex given by Eq. (3.3b) suppresses

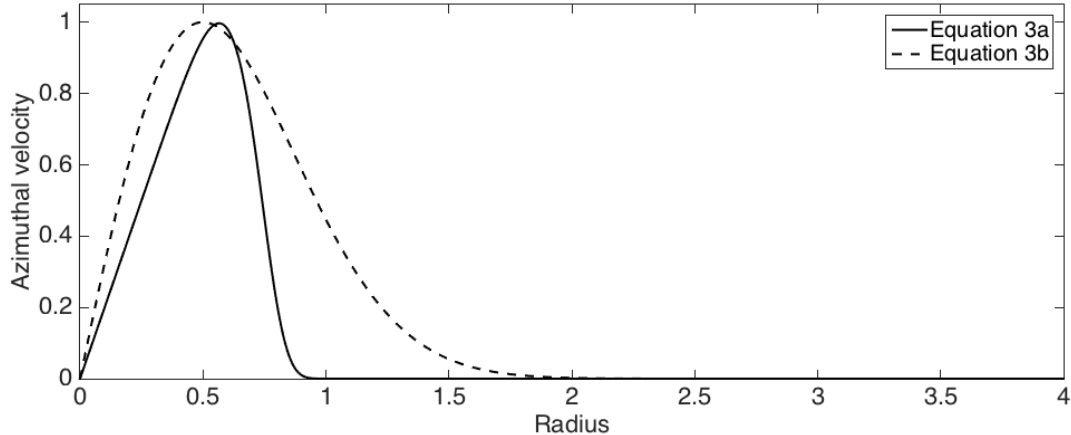


Figure 3.2: Azimuthal velocity profiles of the initial vortex.

instabilities, remaining single and axisymmetric.

$$V(r) = 2r \exp(-12r^8) , \quad (3.3a)$$

$$V(r) = 3.3r \exp(-2r^2) . \quad (3.3b)$$

The boundary conditions are free-slip on the sidewall and no-slip at the bottom; on the top boundary, the velocity is prescribed with the same profile of the initial vortex. Note that the conditions of homogeneous density, rigid lid and flat bottom will exclude gravity waves.

The domain is discretized into $K = 2560$ quadrilateral elements; on each element, solutions are approximated by Legendre polynomials of order $N = 10$, which generates approximately $K(N + 1)^3 = 3,407,360$ grid points; for fixed K , increasing N will increase the resolution. The numerical model is integrated for a total dimensionless time of 300 (about five eddy-turnover times) with a time step of 10^{-3} . For the experiments listed in Table 3.1, the flows typically need an integration time of 120~150 to reach a steady state of total kinetic energy (Fig. 3.3).

Table 3.1:

List of the numerical experiments. The vortices initialized by Eq. (3.3a) and Eq. (3.3b) are designated as target (T) and control (C) experiments, respectively. The initial vortex in Exp. T10 is anticyclonic, denoted by $-$ Eq. (3.3a).

Exp. #	Initial vortex	Domain radius	<i>Ro</i>	<i>Re</i>	Resolution
C1	Eq. (3.3b)	4	0.2	10^4	10
T1	Eq. (3.3a)	4	0.2	10^4	10
T2	Eq. (3.3a)	4	0.01	10^4	10
T3	Eq. (3.3a)	4	0.04	10^4	10
T4	Eq. (3.3a)	4	0.1	10^4	10
T5	Eq. (3.3a)	4	0.4	10^4	10
T6	Eq. (3.3a)	4	0.6	10^4	10
T7	Eq. (3.3a)	4	1	10^4	10
T8	Eq. (3.3a)	4	5	10^4	10
T9	Eq. (3.3a)	8	0.2	10^4	10
T10	$-$ Eq. (3.3a)	4	0.2	10^4	10
T11	Eq. (3.3a)	4	0.2	10^4	13
T12	Eq. (3.3a)	4	0.2	2×10^4	13

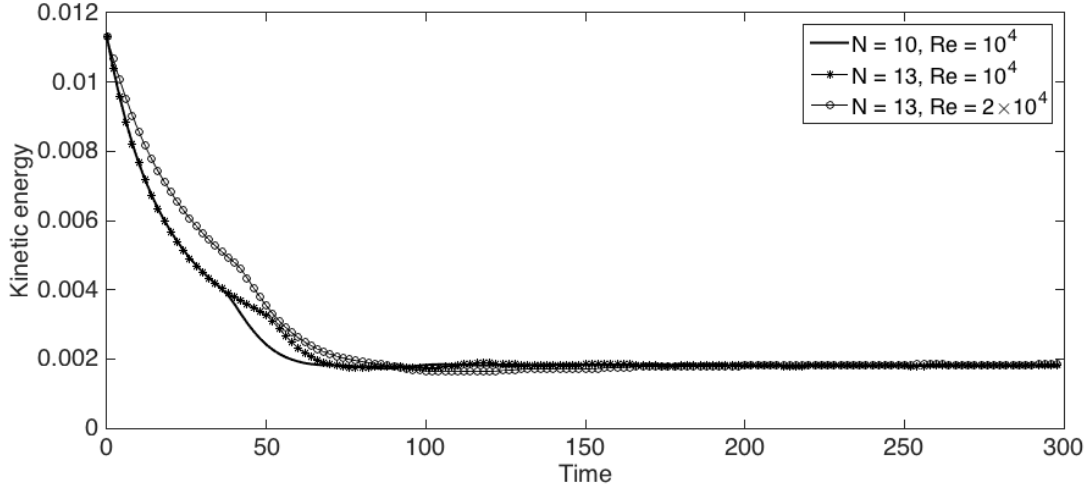


Figure 3.3: The evolutions of kinetic energy of Exp. T1 with different mesh resolutions and Reynolds numbers.

By comparing the two contrasting experiments T1 and C1, I illustrate how the stability and axisymmetry of the vortex can affect the emission of SIWs. The parameter-sweep experiments T2–T8 are designed to investigate the dependence of SIWs on Rossby numbers; the range of Ro is from 0.01 to 5, which covers, for example, ocean mesoscale to submesoscale eddies. I use Exp. T9 to explore the effect of domain size on SIWs, and employ Exp. T10 to study the SIWs emitted from an initially anticyclonic vortex. In order to check the numerical convergence, I conduct Exps. T11 and T12 on a higher-resolution mesh (by increasing the polynomial order to $N = 13$, yielding 7,024,640 grid points) and with a larger Reynolds number ($Re = 2 \times 10^4$).

3.3 Results

3.3.1 Emission of SIWs

Take Exp. T1 as an example to illustrate the generation of SIWs by the initially cyclonic vortex. The vertical vorticity (Figs. 3.4a,c,e) demonstrates the vortex evolution; the vertical velocity (Figs. 3.4b,d,f) manifests the emitted inertial waves.

Besides, the inertial waves can also be manifested by the vorticity anomaly, horizontal divergence and vertical gradient of pressure.

In reality, many factors can push vortices away from geostrophic balance; these include wind forcing, interaction with other vortices, internal waves, bathymetry, *etc.* In this sense, it is useful to investigate how an initially unbalanced vortex evolves. In our experiments, after the unbalanced vortex is initialized, the geostrophic adjustment takes place, leading to the emission of circular inertial waves (Fig. 3.4b). Later, four satellite vortices with negative vorticity are created by the azimuthal wavenumber-4 mode of barotropic instability (Fig. 3.4c); they surround the vortex core of positive vorticity. This instability is caused by the interactions of phase-locking vortex Rossby waves, which exist due to the gradient of mean flow's potential vorticity (*e.g.* Montgomery and Kallenbach 1997; Schecter and Montgomery 2004). Instabilities (or vortex Rossby waves) change the initially axisymmetric vortex into non-axisymmetric, breaking the circular pattern of inertial waves. Subsequently, four pairs of SIWs are emitted from these non-axisymmetric vortices; each pair consists of two spirals with opposite signs in vertical velocity (Fig. 3.4d). Then the four satellite vortices merge and form two larger ones. At the final stage of vortex evolution, a family of vortices constituted by a central vortex and two satellite vortices, also known as tripolar vortices, is established (Fig. 3.4e); meanwhile, SIWs have organized the spirals into two groups (Fig. 3.4f). In addition, the total kinetic energy has now reached a steady state, and the flow becomes nearly balanced, rather than exactly balanced, for it still continuously emits SIWs. Consequently, I attribute the wave emission at the final stage to the spontaneous adjustment emission that is responsible for the wave emission from balanced flows; in contrast, the geostrophic adjustment accounts for the wave emission from unbalanced flows (*e.g.* Plougonven and Zhang 2014). Typically, the geostrophic adjustment makes flows towards a balanced state free of wave emission,

while the spontaneous emission drives flows to emit waves at any stage of evolution (*e.g.* Sugimoto *et al.* 2008).

Moreover, the emitted waves are so weak relative to the vortices that no significant back-reaction between waves and vortices are expected. In fact, I only observe a weak back-reaction during the vortex merging, which merely lasts a short period; therefore, the back-reaction is negligible in our experiments.

Our experiments show that SIWs have two organized phases. The first phase (Fig. 3.4d) is associated with the wavenumber-4 barotropic instability; accordingly, this phase consists of four complete waves in the azimuthal direction (Fig. 3.5a). The second phase (Fig. 3.4f) contains two wave packets (Fig. 3.5b), which are associated with the two satellite vortices formed by the vortices merging. I refer to the first and second phase as “SIW-4” and “SIW-2”, respectively. The SIW-4 phase is transient and is soon replaced by the SIW-2, which keeps intact till the end.

Also, the emission of inertial waves is illustrated by the Hovmöller diagram (Fig. 3.6), which can reveal the propagation of wave phase and energy. The zoom-in views of Hovmöller diagram (Figs. 3.6b,c) reveal that the wave phase propagates radially inward, but the wave energy (group velocity) propagates radially outward, indicating the energy being emitted out of the vortices (wave source). As waves approach the far field, wave energy is gradually dissipated (*cf.* Fig. 3.6a). This opposite propagation between wave phase and wave energy was also observed by Afanasyev *et al.* (2008), who were studying the emission of inertial waves by baroclinic unstable flows using laboratory experiments. In fact, inertial waves have a characteristic propagation; that is, in the horizontal direction, the phase propagation is opposite to the energy propagation, and the phase propagates toward the wave source, whereas the energy propagates away from the wave source. In particular, as shown in Figs. 3.6b and 3.6c, the energy propagation is perpendicular to the phase

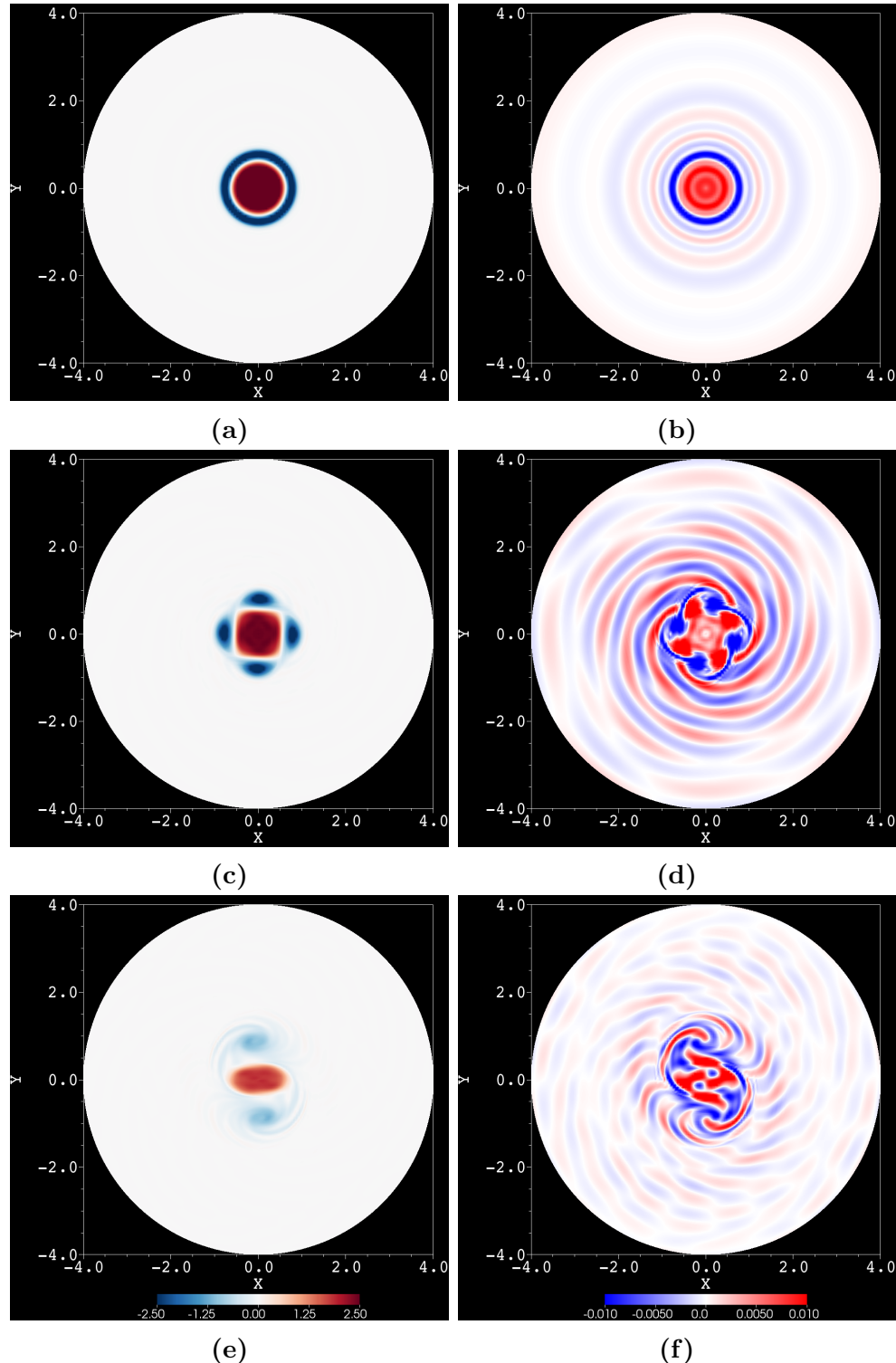


Figure 3.4: Vertical vorticity fields (left column) and vertical velocity fields (right column) from Exp. T1 (initially cyclonic); both fields are plotted at mid-depth horizontal plane at (a, b) time = 6; (c, d) time = 30 and (e, f) time = 204. (The <https://youtu.be/Vw564T17pk4> links the wave animation.)

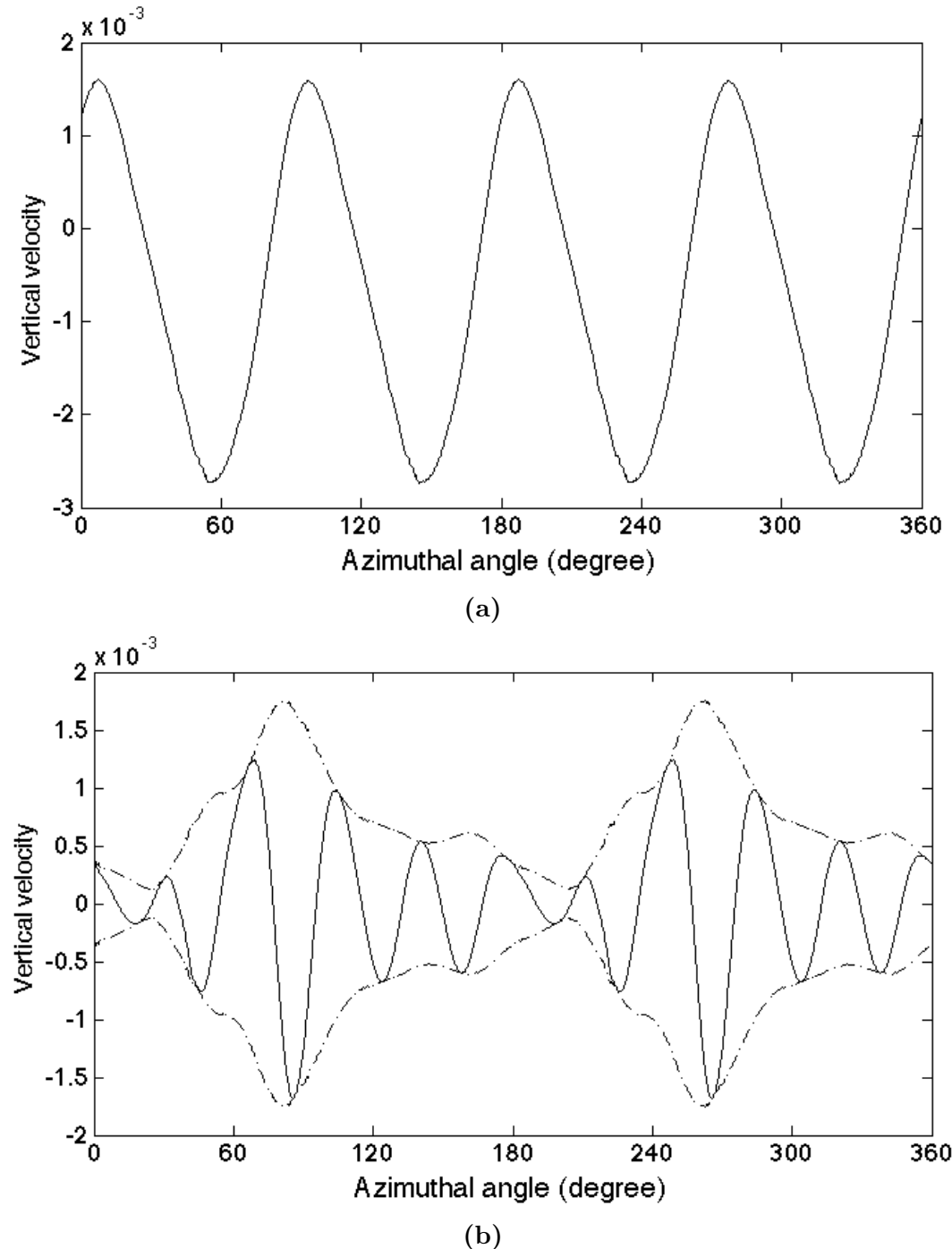


Figure 3.5: Vertical velocity along the circle of radius $r = 2.5$ at the mid-depth in Exp. T1. (a) SIW-4 phase at time = 30 and (b) SIW-2 phase at time = 204 (dashed lines outlining the wave envelope).

propagation; this feature is analogy to that of inertia-gravity waves, whose energy propagation is also perpendicular to their own phase propagation (*e.g.* Gill 1982).

The distance that inertial waves can propagate away from the vortices is limited by the domain size; therefore, I design Exp. T9 which is performed in a domain with doubled radius, to inspect the effect of domain size on inertial waves. As shown in Fig. 3.7, SIWs still exhibit spiral patterns similar to that observed in Exp. T1 (*cf.* Figs. 3.4d,f), and also have two organized phases of SIW-4 and SIW-2. However, the spirals of SIWs extend longer in the larger domain; consequently, I infer that if the domain radius expands more, the spirals will extend even longer.

An initially anticyclonic vortex in Exp. T10 also emits SIWs (Fig. 3.8), and develops similar processes as observed in the cyclonic vortex, such as the geostrophic adjustment, vortex Rossby waves, vortex merging and spontaneous wave emission. As well, these SIWs exhibit a transient phase of SIW-4 (Fig. 3.8d) and a final phase of SIW-2 (Fig. 3.8f); nevertheless, the direction of spirals has reversed.

By contrast, the vortex in Exp. C1 remains axisymmetric and stable throughout the experiment, but no SIWs are observed (Fig. 3.9). At the early stage of evolution, the geostrophic adjustment also generates circular inertial waves; however, these waves are gradually diminishing while the flow is approaching a steady state. The fact that no SIWs are generated by this stable, axisymmetric vortex indicates that the generation of SIWs requires the vortex to become non-axisymmetric and to remain unsteady (*i.e.* the local time derivative $\frac{\partial}{\partial t} \neq 0$). Particularly, the non-axisymmetry is necessary in forming the spirals, and the unsteadiness is requisite in generating waves.

The numerical convergence is confirmed by the similar wave characteristics observed in a higher-resolution mesh with a larger Reynolds number. For instance, in comparison with the SIWs in Exp. T1 (*cf.* Figs. 3.4d,f and Fig. 3.5), the SIWs in

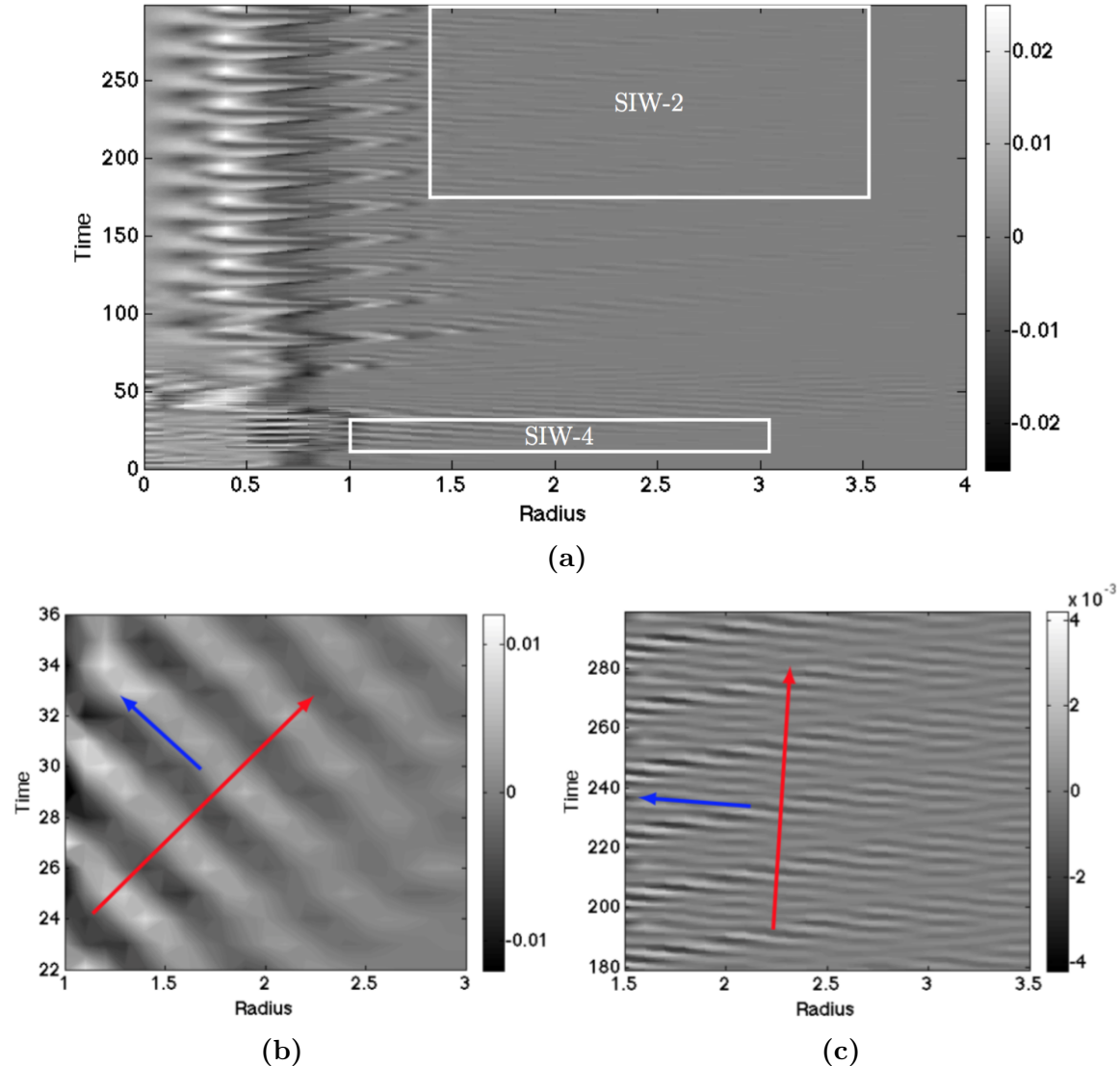


Figure 3.6: (a) Hovmöller diagram of vertical velocity on mid-depth horizontal plane, shown in the radius–time section. (b) and (c) show the zoom-in views of regions denoted by the boxes in (a), for phases SIW-4 and SIW-2, respectively. The blue arrows show the direction of phase speed and the red arrows point the direction of group velocity.

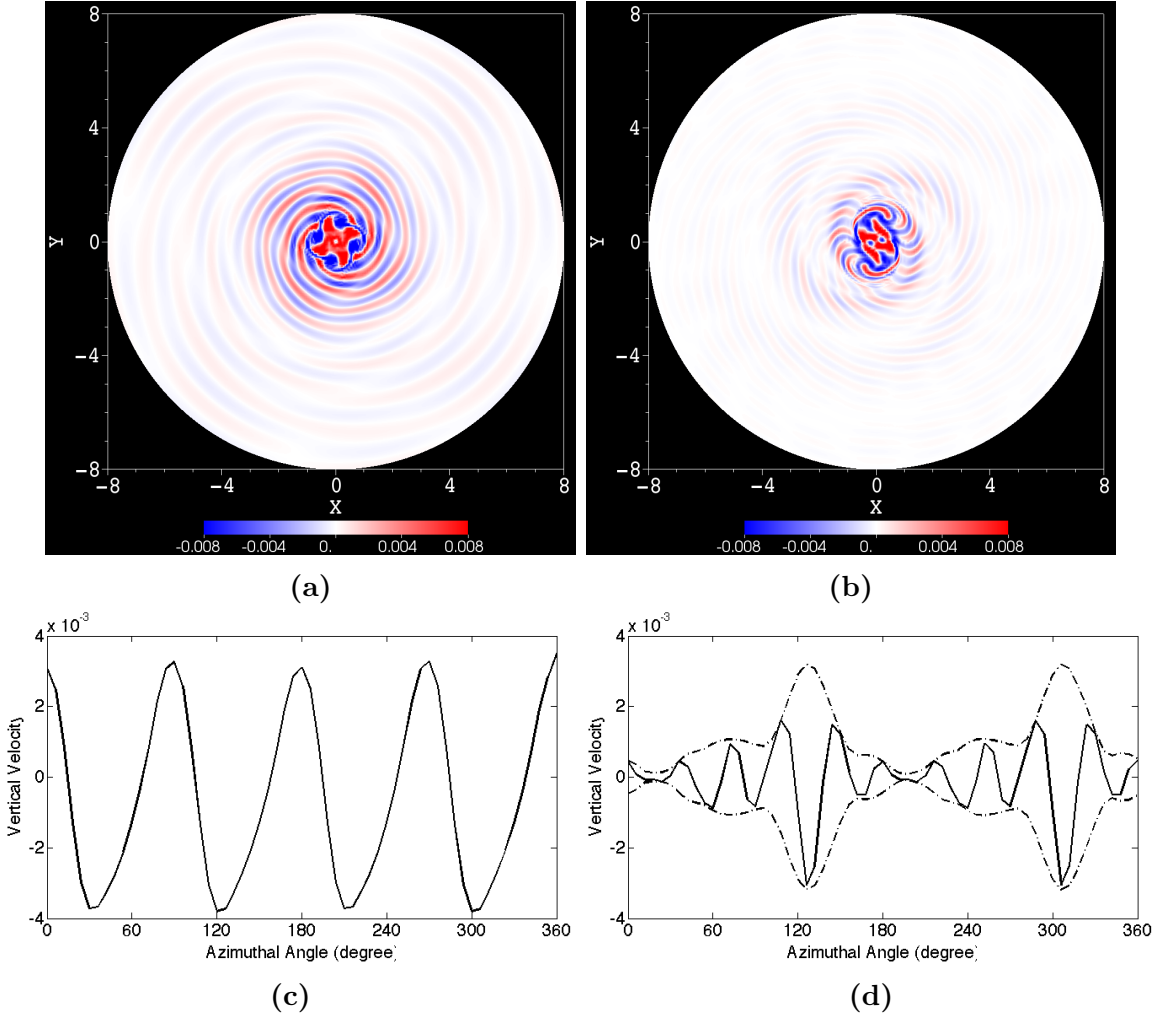


Figure 3.7: Upper panel: vertical velocity fields at the mid-depth horizontal plane, from Exp. T9, at (a) time = 30 and (b) time = 204. Lower panel: the corresponding vertical velocity along the circle of radius $r = 6$ for phase (c) SIW-4 and (d) SIW-2 (dashed lines outlining the wave envelope).

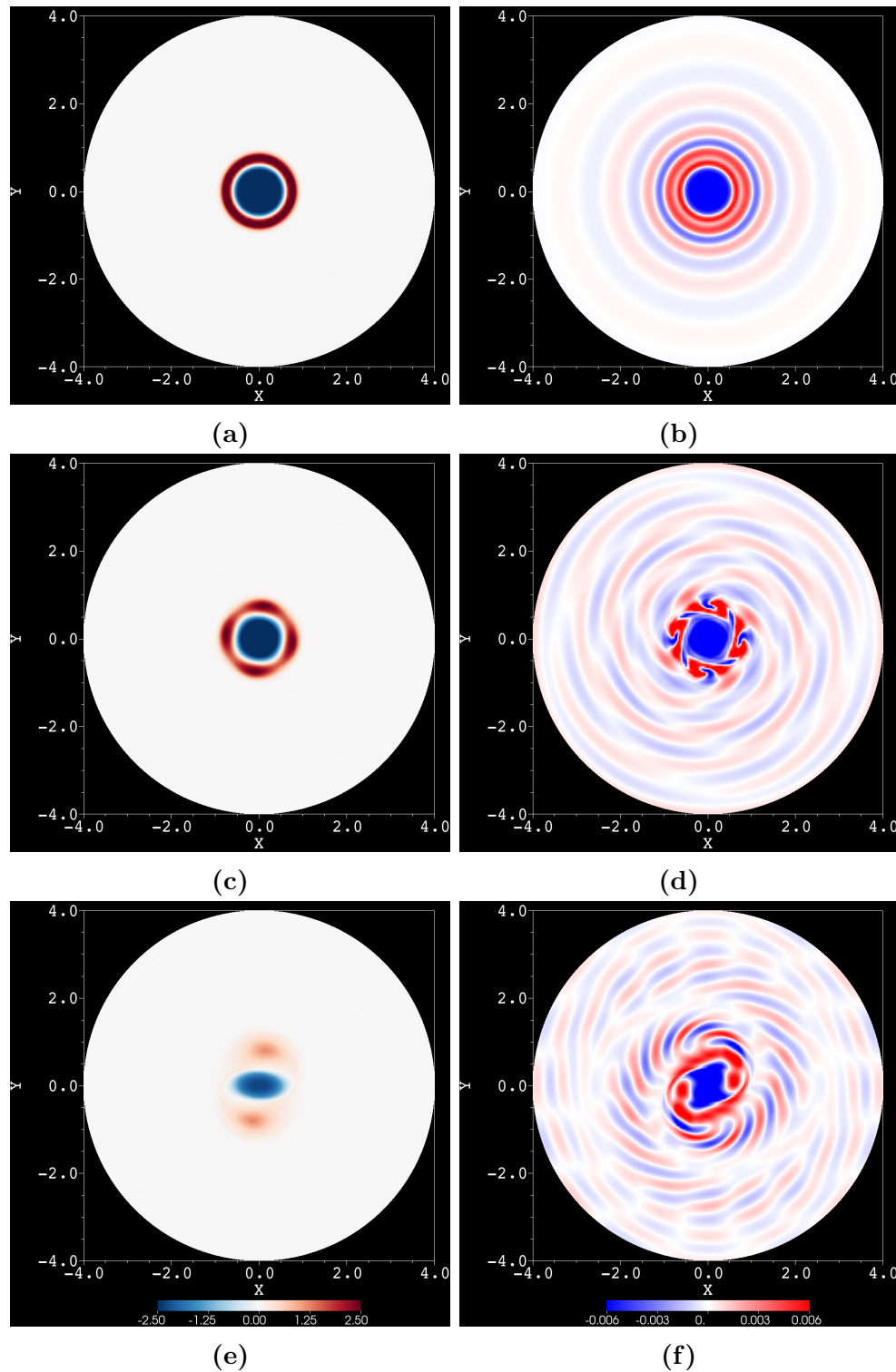


Figure 3.8: Vertical vorticity fields (left column) and vertical velocity fields (right column) from Exp. T10; both fields are plotted at mid-depth horizontal plane at (a, b) time = 6; (c, d) time = 26 and (e, f) time = 205.

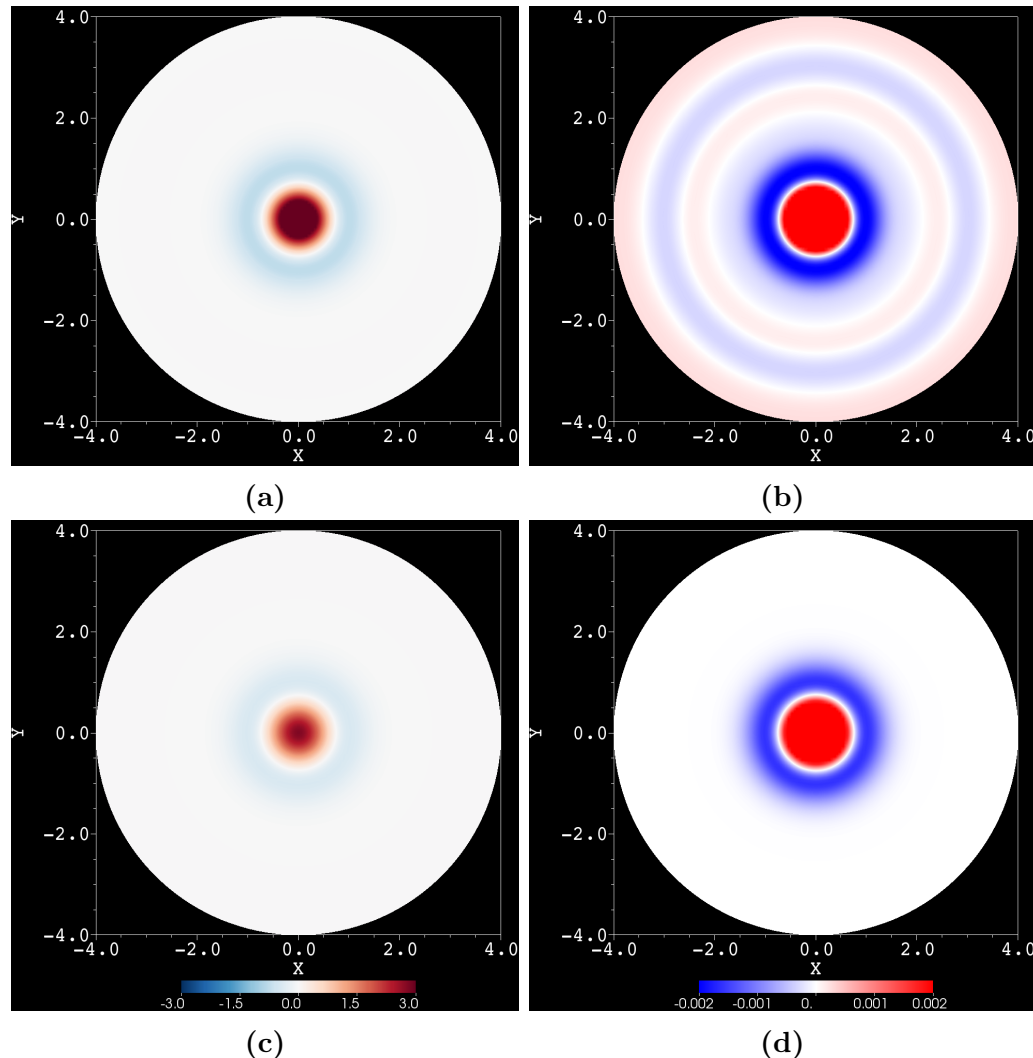


Figure 3.9: Vertical vorticity fields (left column) and vertical velocity fields (right column) from Exp. C1; both fields are plotted at mid-depth horizontal plane at (a,b) time = 10 and (c, d) time = 296.

Exps. T11 and T12 (Fig. 3.10) have similar wave patterns, nearly equal amplitudes, and same organizations like phases SIW-4 and SIW-2. Particularly in Exp. T12, the wave amplitude is a little larger at phase SIW-4, and the wave is a bit more intense in the far field due to the larger Reynolds number (smaller viscosity). Together with the fact that the wave scale is much larger than the grid spacing, the numerical convergence rules out the possibility that SIWs are numerical artifacts.

3.3.2 Dependence of SIWs on Rossby number

In order to investigate how SIWs change with Rossby numbers, I resort to parameter-sweep experiments T2–T8. In experiments T2–T7 (small $Ro \leq 1$), circular inertial waves are observed owing to the geostrophic adjustment at the early stage of evolution; later, the circular inertial waves are replaced by SIWs. At the final stage, all SIWs evolve into the phase SIW-2 (Fig. 3.11). However, in Exp. T8 (large $Ro = 5$), no inertial waves appear, and both the vorticity and velocity fields looks chaotic, lacking the tripolar structure observed in Exps. T2–T7.

Next I compare the wave frequency measured in experiments with the prediction by theory. The theoretical eigenfrequency or dispersion relation of inertial waves that exist in cylindrical domains, was first derived by Kelvin (1880) in a linear inviscid system. A complete derivation was documented by Greenspan (1969). Concisely, by the asymptotic expansion of small parameter, inertial waves are formulated as ageostrophic modes of an initial-value problem for rotating fluids. Then by exploiting proper boundary conditions of the cylindrical geometry, the dispersion relation is derived as

$$\lambda_{nmk} = 2 \left(1 + \frac{\xi_{nmk}^2}{n^2 \pi^2 a^2} \right)^{-\frac{1}{2}}, \quad (3.4)$$

where λ_{nmk} is the eigenfrequency of wave mode (n, m, k) with n, m, k denoting the axial, radial and azimuthal wavenumbers, respectively (Greenspan 1969). Here a is

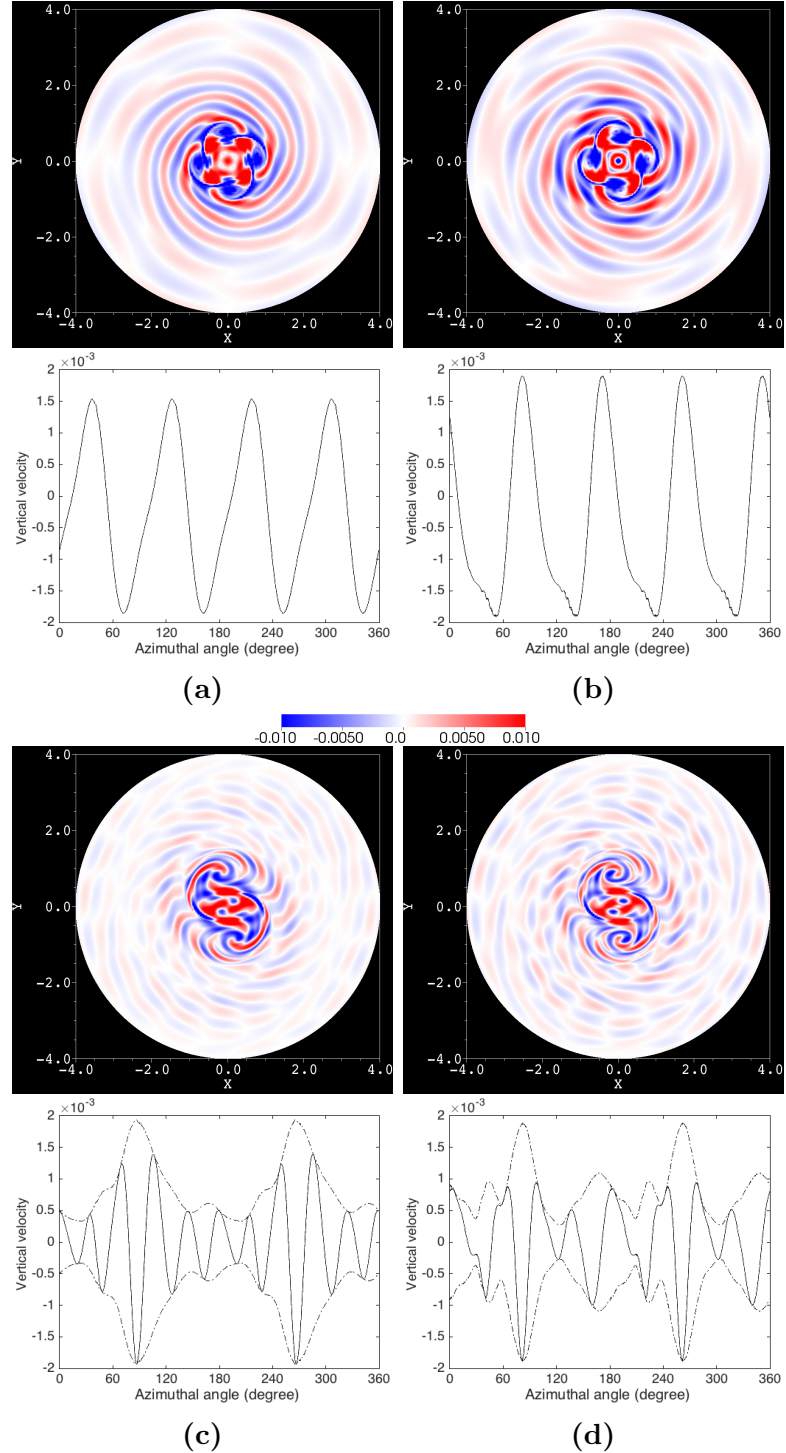
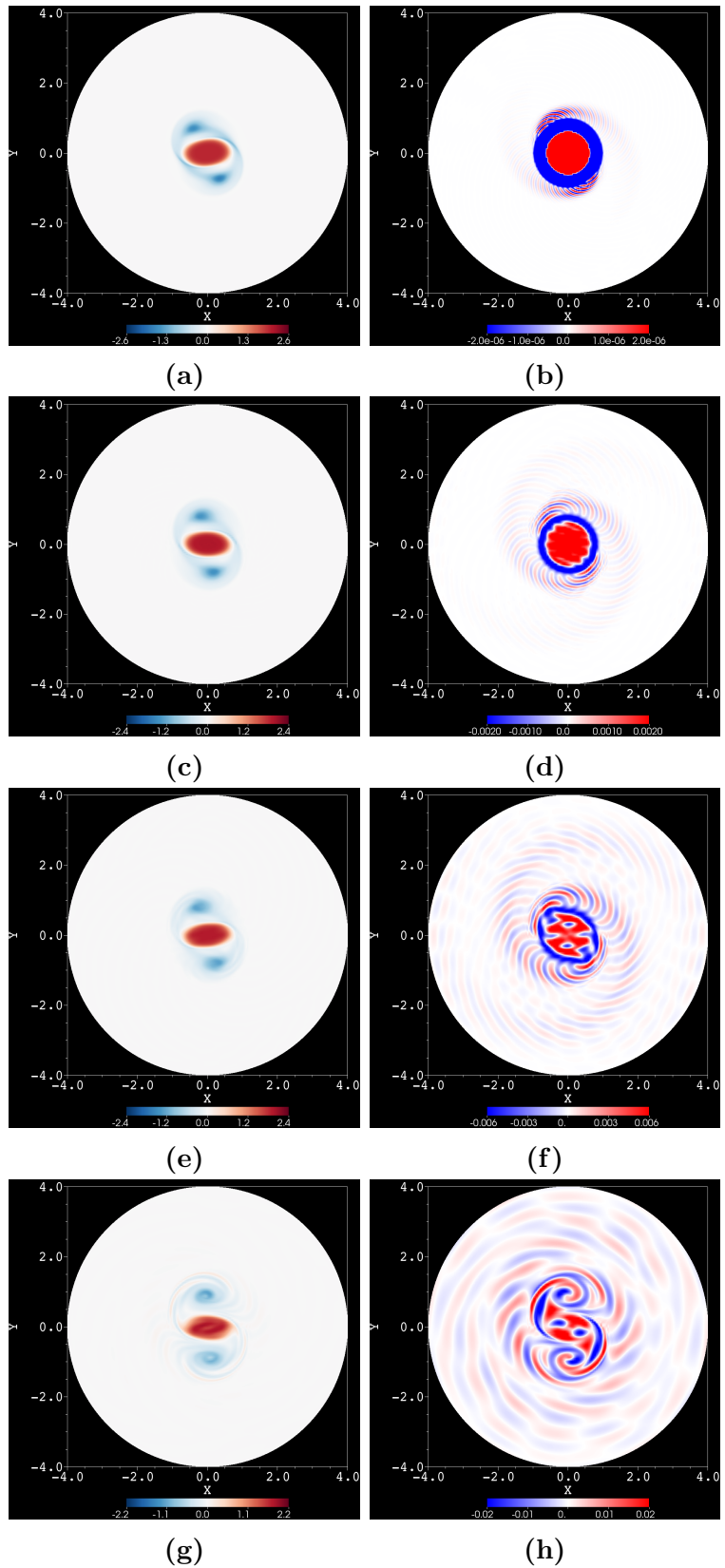


Figure 3.10: Phases SIW-4 and SIW-2 of (a,c) Exp. T11 and (b,d) Exp. T12 at the mid-depth horizontal plane. [The vertical velocities are sampled along the circle of radius = 2.5 to show the four complete waves and two wave packets; dashed lines represent wave envelopes.]



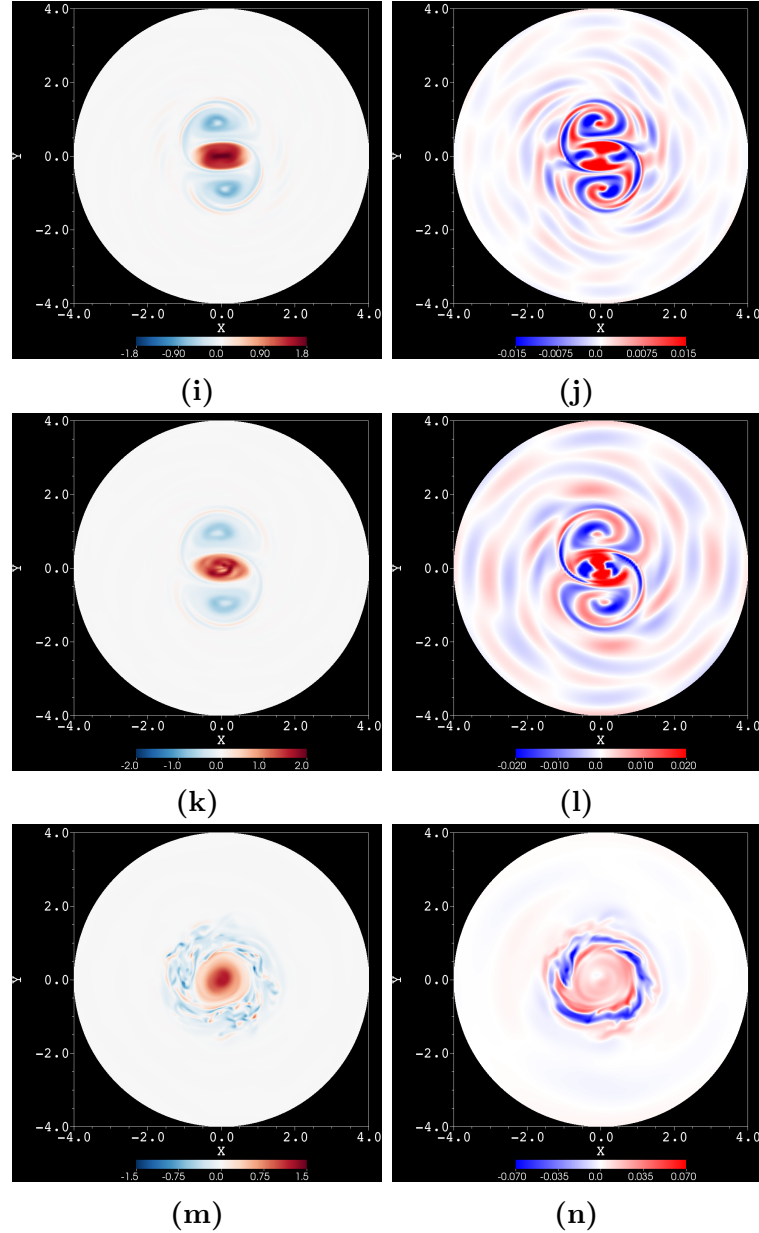


Figure 3.11: Snapshots of vertical vorticity fields (left column) and the corresponding vertical velocity fields (right column) at mid-depth horizontal plane for target experiments (a,b) T2; (c,d) T3; (e,f) T4; (g,h) T5; (i,j) T6; (k,l) T7; (m,n) T8. (Note the change of magnitude of vertical velocity.)

the ratio of domain's radius to height, and ξ_{nmk} is the m -th positive solution of the transcendental equation (3.5):

$$\xi \frac{d}{d\xi} J_{|k|}(\xi) + k \left(1 + \frac{\xi^2}{n^2 \pi^2 a^2} \right)^{\frac{1}{2}} J_{|k|}(\xi) = 0 , \quad (3.5)$$

where $J_{|k|}(\xi)$ is the Bessel function of the first kind of order $|k|$. The eigenfrequency λ_{nmk} in Eq. (3.4) is normalized by the angular velocity Ω of background rotation, and has a maximum equal to 2; that is, the frequency of inertial waves cannot exceed the Coriolis parameter f ($= 2\Omega$).

I use spectral analysis to acquire the most energetic frequency and wavenumbers (n, m, k) of waves emitted during the final stage of vortex evolution; they are referred to as experimental frequency and wavenumbers. Then I substitute (n, m, k) into Eq. (3.5) to obtain ξ , which is used in Eq. (3.4) to calculate the theoretical frequency λ . As shown in Table 3.2, there is a good agreement between the theory and experiments.

According to Fig. 3.12a, the (maximum) wave amplitude increases linearly with Rossby number within $0.01 \leq Ro \leq 0.2$, and reaches a maximum at $Ro = 0.4$; afterwards at $0.6 \leq Ro \leq 1$, the amplitude drops to a roughly constant value.

Since SIWs are manifested by the vertical velocity, I use the quadratic vertical velocity (W^2) to indicate the energy of SIWs; then I define the ratio $Q = W_{\text{wave}}^2 / W_{\text{vortex}}^2$ to estimate the overall wave intensity, where W_{wave}^2 denotes the square of vertical velocity integrated over the volume of SIWs, and W_{vortex}^2 represents the square of vertical velocity integrated over the volume of vortices; hereafter, the boundary of vortices is estimated by the zero vorticity contour. In agreement with the wave amplitude, the wave intensity is the largest at $Ro = 0.4$ (Fig. 3.12b).

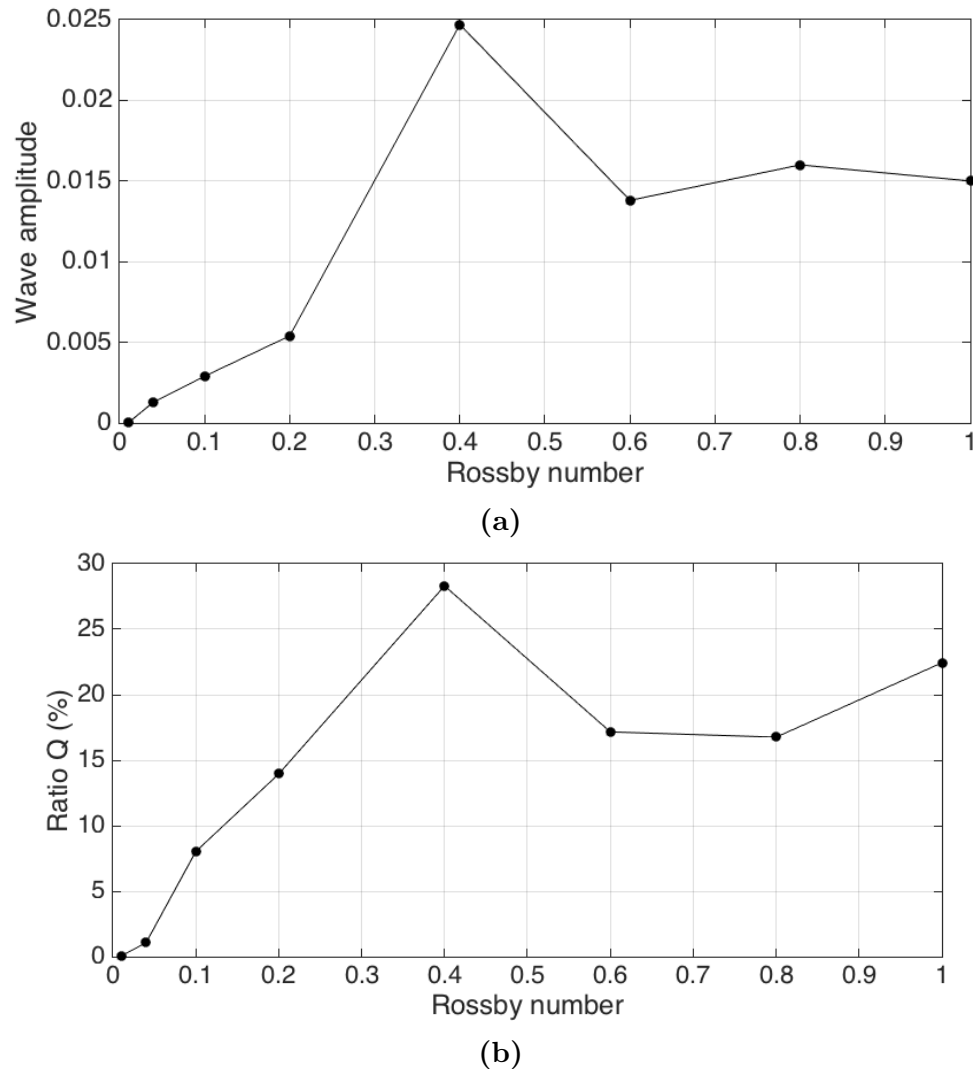


Figure 3.12: The change of (a) SIWs amplitude and (b) ratio Q with Rossby number.
(Wave amplitudes are recorded at the final stage of vortex evolution.)

Table 3.2:
List of the most energetic mode and frequency of SIWs.

Exp.#	Ro	Mode (n, m, k)	Eigenfrequency	
			Theory	Experiment
T2	0.01	(1,72,31)	0.094	0.085
T3	0.04	(1,26,20)	0.234	0.231
T4	0.1	(1,14,12)	0.431	0.462
T1	0.2	(1,11,10)	0.545	0.616
T10	0.2	(1,12, 8)	0.542	0.564
T5	0.4	(1,11, 6)	0.624	0.667
T6	0.6	(1, 7, 6)	0.881	0.923
T7	1	(1, 7, 4)	0.966	0.898

3.3.3 Source of SIWs

Lighthill (1952) conducted a pioneering work on the generation mechanism of sound waves by vortical flows with small Mach number, showing that the unstratified, three-dimensional, unsteady vortical flows will spontaneously generate sound waves. Later, Ford (1994a) extended Lighthill's theory into the f -plane, shallow-water equations, and demonstrated that rotating, stratified vortical flows with small Froude number can spontaneously emit inertia-gravity waves.

Let's begin with the governing equations (3.6) for homogeneous, inviscid, rotating fluids:

$$\frac{\partial u}{\partial t} + u \frac{\partial u}{\partial x} + v \frac{\partial u}{\partial y} + w \frac{\partial u}{\partial z} - fv = -\frac{1}{\rho} \frac{\partial p}{\partial x}, \quad (3.6a)$$

$$\frac{\partial v}{\partial t} + u \frac{\partial v}{\partial x} + v \frac{\partial v}{\partial y} + w \frac{\partial v}{\partial z} + fu = -\frac{1}{\rho} \frac{\partial p}{\partial y}, \quad (3.6b)$$

$$\frac{\partial w}{\partial t} + u \frac{\partial w}{\partial x} + v \frac{\partial w}{\partial y} + w \frac{\partial w}{\partial z} = -\frac{1}{\rho} \frac{\partial p}{\partial z}, \quad (3.6c)$$

$$\frac{\partial u}{\partial x} + \frac{\partial v}{\partial y} + \frac{\partial w}{\partial z} = 0, \quad (3.6d)$$

where (u, v, w) is the velocity component in (x, y, z) direction; f is the Coriolis parameter; p is the pressure and ρ is the constant density.

I manipulate the above Eqs. (3.6) to get its flux form, which is:

$$\frac{\partial u}{\partial t} - fv + \frac{\partial P}{\partial x} = -\left(\frac{\partial uu}{\partial x} + \frac{\partial uv}{\partial y} + \frac{\partial uw}{\partial z}\right), \quad (3.7a)$$

$$\frac{\partial v}{\partial t} + fu + \frac{\partial P}{\partial y} = -\left(\frac{\partial uv}{\partial x} + \frac{\partial vv}{\partial y} + \frac{\partial vw}{\partial z}\right), \quad (3.7b)$$

$$\frac{\partial w}{\partial t} + \frac{\partial P}{\partial z} = -\left(\frac{\partial uw}{\partial x} + \frac{\partial vw}{\partial y} + \frac{\partial ww}{\partial z}\right), \quad (3.7c)$$

where $P = p/\rho$. Take $\frac{\partial(3.7b)}{\partial x} - \frac{\partial(3.7a)}{\partial y}$, obtaining

$$\frac{\partial \zeta}{\partial t} = f \frac{\partial w}{\partial z} - \left(\frac{\partial^2 uv}{\partial x^2} + \frac{\partial^2 vv}{\partial x \partial y} + \frac{\partial^2 vw}{\partial x \partial z}\right) + \left(\frac{\partial^2 uu}{\partial x \partial y} + \frac{\partial^2 uv}{\partial y^2} + \frac{\partial^2 uw}{\partial y \partial z}\right), \quad (3.8)$$

where $\zeta = \frac{\partial v}{\partial x} - \frac{\partial u}{\partial y}$. Take $\frac{\partial}{\partial t} \left[\frac{\partial(3.7a)}{\partial x} + \frac{\partial(3.7b)}{\partial y} \right]$, obtaining

$$\begin{aligned} & \frac{\partial^2}{\partial t^2} \left(\frac{\partial w}{\partial z} \right) + f \frac{\partial \zeta}{\partial t} - \frac{\partial}{\partial t} \left(\frac{\partial^2 P}{\partial x^2} + \frac{\partial^2 P}{\partial y^2} \right) = \\ & \frac{\partial}{\partial t} \left(\frac{\partial^2 uu}{\partial x^2} + \frac{\partial^2 uv}{\partial x \partial y} + \frac{\partial^2 uw}{\partial x \partial z} \right) + \frac{\partial}{\partial t} \left(\frac{\partial^2 uv}{\partial x \partial y} + \frac{\partial^2 vv}{\partial y^2} + \frac{\partial^2 vw}{\partial y \partial z} \right). \end{aligned} \quad (3.9)$$

Substitute Eq. (3.8) into Eq. (3.9) and then take $\frac{\partial}{\partial z}$, obtaining

$$\begin{aligned} & -\frac{\partial}{\partial t} \left(\frac{\partial^2}{\partial x^2} + \frac{\partial^2}{\partial y^2} \right) \frac{\partial P}{\partial z} + \frac{\partial^2}{\partial t^2} \left(\frac{\partial^2 w}{\partial z^2} \right) + f^2 \frac{\partial^2 w}{\partial z^2} = \\ & \frac{\partial^2}{\partial t \partial z} \left[\left(\frac{\partial^2 uu}{\partial x^2} + \frac{\partial^2 uv}{\partial x \partial y} + \frac{\partial^2 uw}{\partial x \partial z} \right) + \left(\frac{\partial^2 uv}{\partial x \partial y} + \frac{\partial^2 vv}{\partial y^2} + \frac{\partial^2 vw}{\partial y \partial z} \right) \right] + \\ & f \frac{\partial}{\partial z} \left[\left(\frac{\partial^2 uv}{\partial x^2} + \frac{\partial^2 vv}{\partial x \partial y} + \frac{\partial^2 vw}{\partial x \partial z} \right) - \left(\frac{\partial^2 uu}{\partial x \partial y} + \frac{\partial^2 uv}{\partial y^2} + \frac{\partial^2 uw}{\partial y \partial z} \right) \right]. \end{aligned} \quad (3.10)$$

Last, substitute Eq. (3.7c) into Eq. (3.10) to eliminate $\frac{\partial P}{\partial z}$, yielding

$$\frac{\partial^2}{\partial t^2} \left(\frac{\partial^2 w}{\partial x^2} + \frac{\partial^2 w}{\partial y^2} + \frac{\partial^2 w}{\partial z^2} \right) + f^2 \frac{\partial^2 w}{\partial z^2} = S, \quad (3.11)$$

where

$$S = \sum_{i=1}^2 \sum_{j=1}^3 \frac{\partial^2}{\partial x_i \partial x_j} T_{ij}, \quad (3.12)$$

and

$$T_{ij} = \frac{\partial}{\partial t} \left[\frac{\partial}{\partial x_3} (u_i u_j) \right] + f \sum_{m=1}^2 \frac{\partial}{\partial x_3} (\varepsilon_{im} u_m u_j) - \frac{\partial}{\partial t} \left[\sum_{n=1}^3 \frac{\partial}{\partial x_n} (\delta_{ij} u_n u_3) \right], \quad (3.13)$$

with (x_1, x_2, x_3) denoting (x, y, z) , and (u_1, u_2, u_3) meaning (u, v, w) ; $\varepsilon_{11} = \varepsilon_{22} = 0$, $\varepsilon_{12} = -\varepsilon_{21} = 1$; $\delta_{ij} = 1$ (if $i = j$) and $\delta_{ij} = 0$ (if $i \neq j$). Now I have extended the Lighthill-Ford radiation theory, which is responsible for the emission of inertia-gravity waves, into the emission of inertial waves. The left-hand side of Eq. (3.11) is the operator of inertial waves, and the right-hand side S represents the wave source that consists of nonlinear terms, including the back-reaction of waves.

Here I use the two contrasting Exps. T1 and C1 to illustrate the function of the wave source S . At the early stage of vortex evolution, wave sources in Exps. T1 and C1 both have regions of large-magnitude sources [$S \gg \mathcal{O}(1)$] inside the vortex; these regions exhibit a quadrupole pattern (Figs. 3.13a,b). At the final evolution stage, the

vortices in Exp. T1 still has large-magnitude wave sources (Fig. 3.13c); nevertheless, the magnitude of wave source in Exp. C1 drops to a level much smaller than $\mathcal{O}(1)$ (Fig. 3.13d). Recall the evolutions of inertial waves in Exps. T1 and C1. At the early stage, inertial waves are emitted in both Exps. T1 and C1 (Figs. 3.4b and 3.9b); at the final stage, inertial waves still exist in Exp. T1 (Fig. 3.4f), but vanishes in Exp. C1 (Fig. 3.9d). Based on the corresponding changes between wave sources and wave emissions, I suggest that the wave source S can function as an indicator for the emission of inertial waves. Specifically, if the vortical flow possesses large-magnitude wave sources [$S \gg \mathcal{O}(1)$], it can emit significant inertial waves, provided that the peak frequency of wave source satisfies the condition to be discussed below. (Note that S is computed in terms of Eq. (3.12) with the dimensionless output from NEK5000; thus here the value of S is also dimensionless.)

Also, I calculate the wave sources of other target experiments at the final stage of evolution. In terms of Fig. 3.14, all the wave sources have regions of $S \geq \mathcal{O}(1)$ inside the vortices; consequently, inertial waves are observed in all these experiments. Among the four experiments shown in Fig. 3.14, the magnitude of S in Exp. T2 (Fig. 3.14b; $Ro = 0.01$) is the smallest, only a little over $\mathcal{O}(1)$, which I suggest is the threshold for significant wave emission; accordingly, the wave emission in Exp. T2 is the weakest, with the wave amplitude being several orders of magnitude less than that in other target experiments T3–T7 (*cf.* Fig. 3.11).

According to Fig. 3.15, the most energetic wave frequency listed in Table 3.2 matches well with the highest peak frequency of wave source; thus, via resonance only these wave modes can gain the most energy from sources. By contrast, for Exp. T8 shown in Fig. 3.15f, the peak frequency is much larger than 2, which is the (dimensionless) maximum frequency of inertial waves (*cf.* Eq. 3.4). In fact, all peaks are beyond the frequency of 2; hence, no inertial waves emit from the wave source in

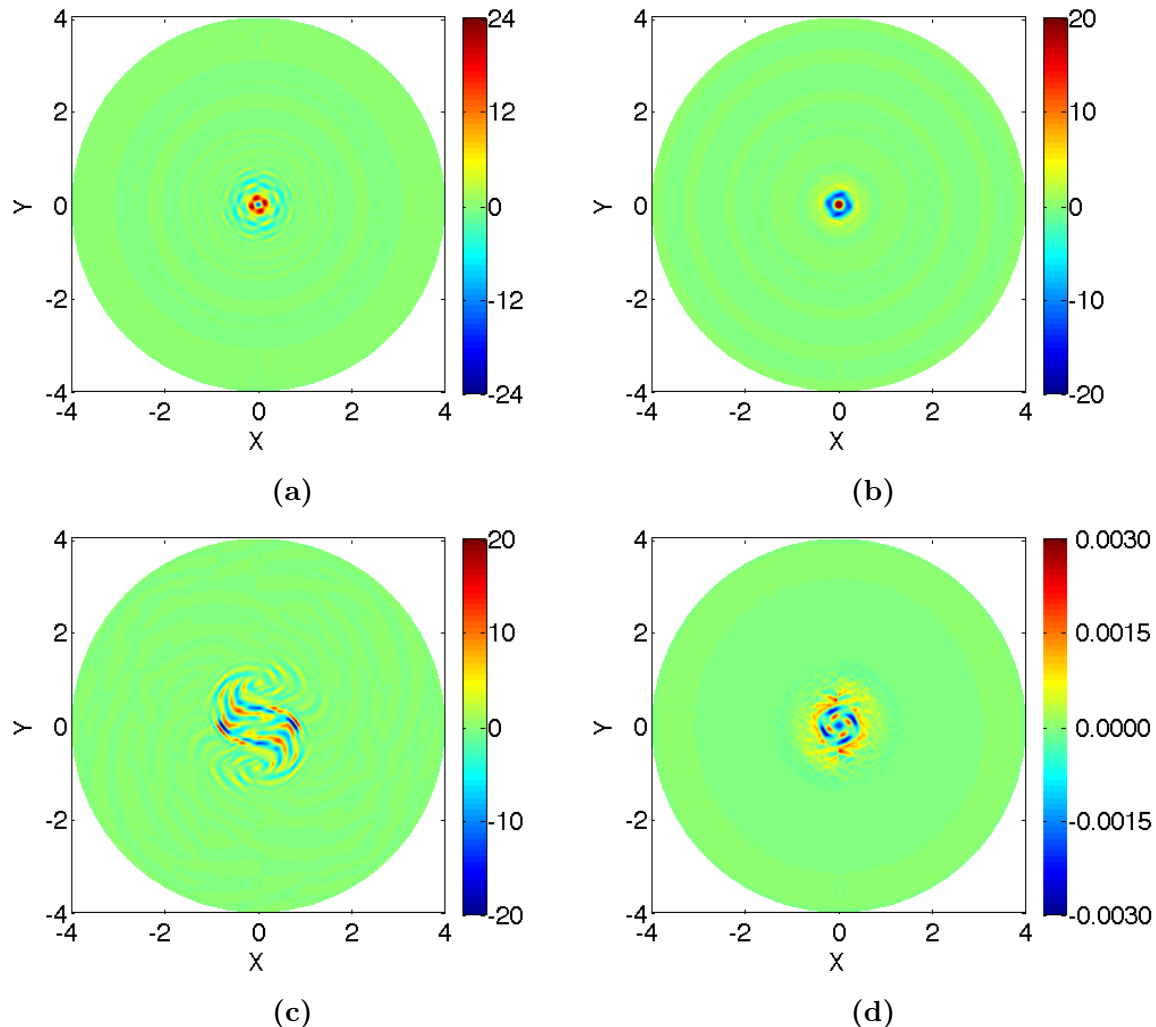


Figure 3.13: Wave source fields S in Exp. T1 (left column) at (a) time = 6, (c) time = 204; the fields in Exp. C1 (right column) at (b) time = 10, (d) time = 296, at mid-depth horizontal plane. (Note the change of magnitude of wave source.)

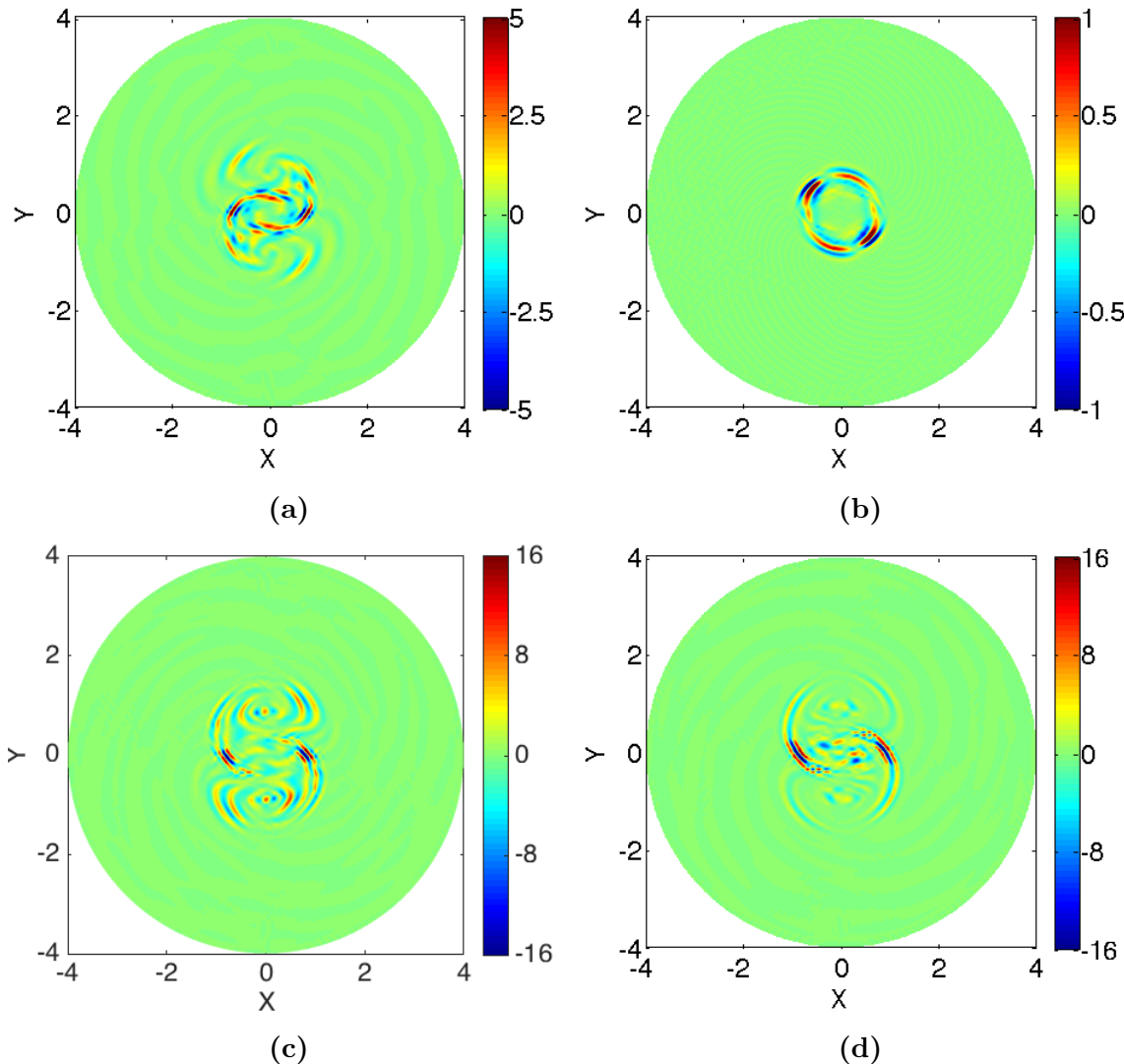


Figure 3.14: Snapshots of the wave source fields S in Exps. (a) T10 (b) T2 (c) T5 and (d) T7 at mid-depth horizontal plane. (The time stamps are the same to that of the corresponding wave fields shown in Figs. 3.8f, 3.11b, 3.11h and 3.11l, respectively.)

Exp. T8, even though the wave source has $S \gg \mathcal{O}(1)$. To sum up, if the wave source has $S \gg \mathcal{O}(1)$ and has a peak frequency below 2, significant emissions of inertial waves are expected.

Further, I divide the wave source S in Eq. (3.12) into three parts based on the three terms of Eq. (3.13), *i.e.* $S = S_1 + S_2 + S_3$ with

$$S_1 = \sum_{i=1}^2 \sum_{j=1}^3 \frac{\partial^2}{\partial x_i \partial x_j} \left\{ \frac{\partial}{\partial t} \left[\frac{\partial}{\partial x_3} (u_i u_j) \right] \right\}, \quad (3.14a)$$

$$S_2 = \sum_{i=1}^2 \sum_{j=1}^3 \frac{\partial^2}{\partial x_i \partial x_j} \left\{ f \sum_{m=1}^2 \frac{\partial}{\partial x_3} (\varepsilon_{im} u_m u_j) \right\}, \quad (3.14b)$$

$$S_3 = \sum_{i=1}^2 \sum_{j=1}^3 \frac{\partial^2}{\partial x_i \partial x_j} \left\{ -\frac{\partial}{\partial t} \left[\sum_{n=1}^3 \frac{\partial}{\partial x_n} (\delta_{ij} u_n u_3) \right] \right\}. \quad (3.14c)$$

S_1 and S_3 are related to the unsteadiness of wave source; in a steady wave source, S_1 and S_3 are zero, without contributions to wave emission. S_2 is associated with the Coriolis force or background rotation; however, strong background rotation (large f) does not necessarily indicate large S_2 , for under strong background rotation, the flow tends to be two dimensional, causing the vertical gradient ($\partial/\partial x_3$) in S_2 to be small.

Then, I integrate $|S_1|$, $|S_2|$ and $|S_3|$ over the volume of vortices to estimate the overall intensity of each source term. According to Fig. 3.16, S_1 is always smaller than S_2 and S_3 but not negligible, and is almost constant at $Ro \geq 0.2$. When $Ro < 0.4$ or so, S_2 is the primary source; however, the primary source shifts to S_3 when $Ro \geq 0.4$. The total source S increases with Rossby number, and reaches its maximum at $Ro = 0.2$; then, it drops to a nearly constant value within $0.6 \leq Ro \leq 1$.

Fig. 3.16 and Fig. 3.12 imply that the largest source intensity (at $Ro = 0.2$) does not guarantee the strongest wave intensity (at $Ro = 0.4$), though a positive correlation

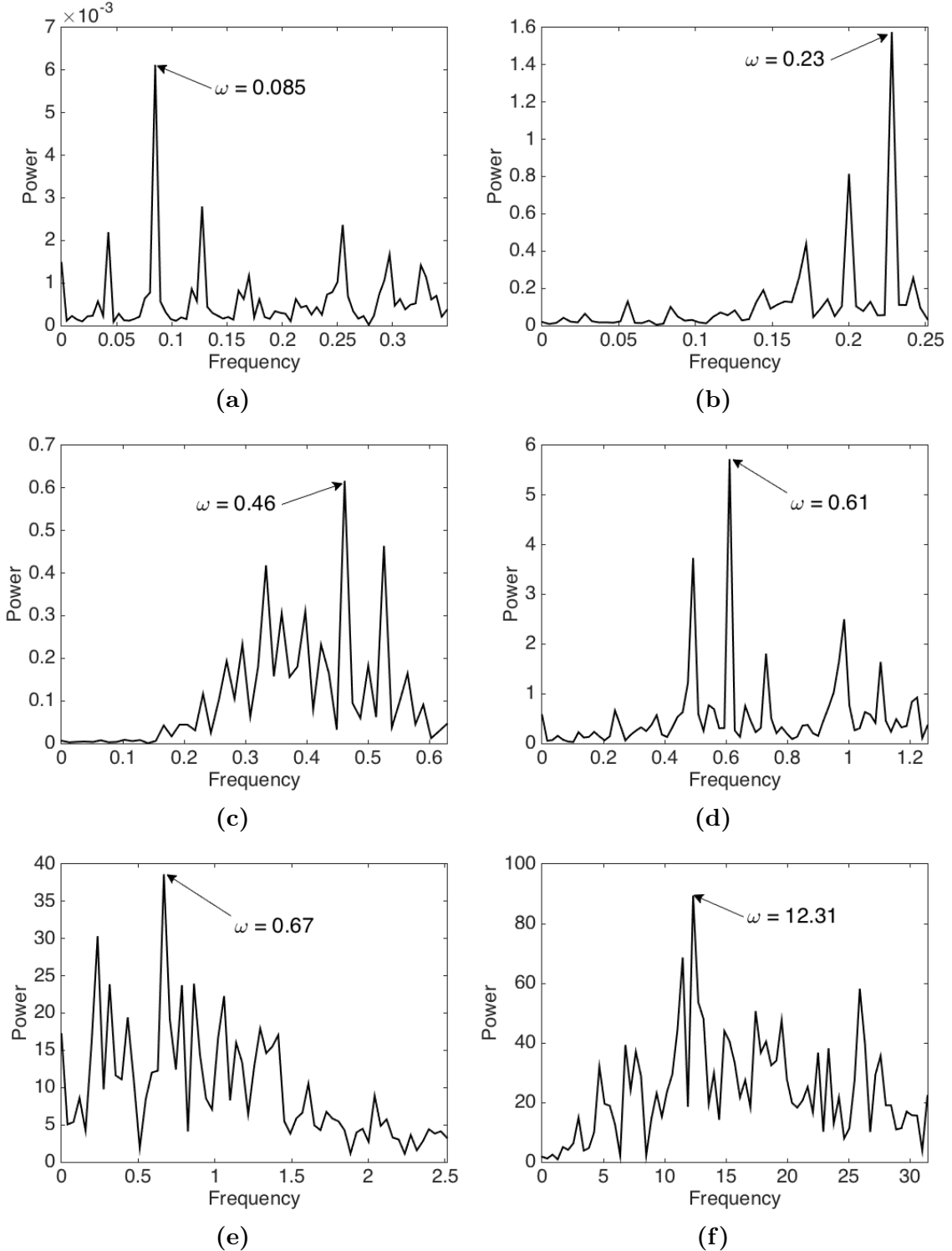


Figure 3.15: Frequency spectra of the wave source S inside the vortex in Exps. (a) T2 (b) T3 (c) T4 (d) T1 (e) T5 and (f) T8. (Note that the maximum frequency of inertial waves is 2 according to Eq. 3.4.)

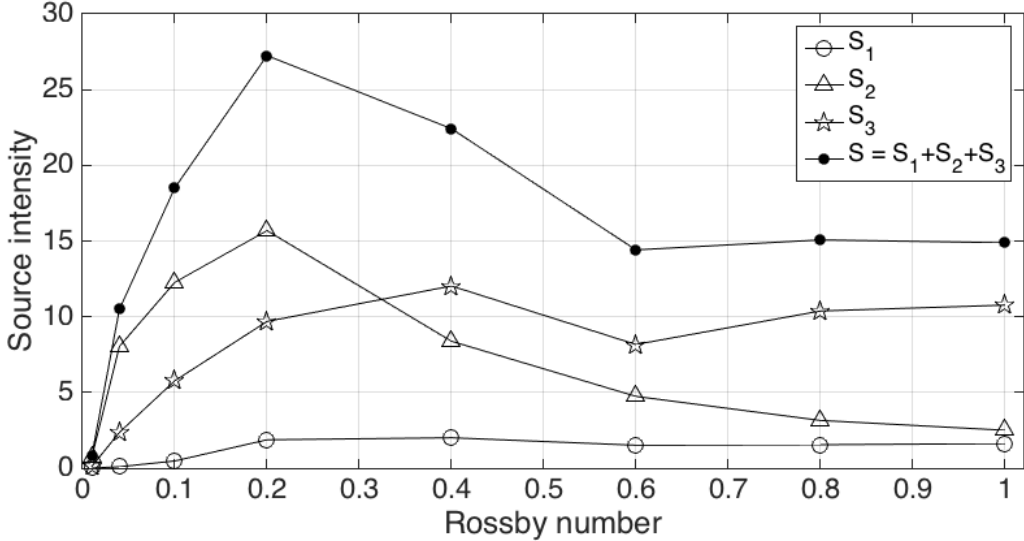


Figure 3.16: The change of source intensity with Rossby number. (Source intensities are computed at the final stage of vortex evolution.)

exists between the wave intensity and source intensity within $0.01 \leq Ro \leq 0.2$. Besides, within $0.6 \leq Ro \leq 1$, the source intensity remains nearly constant; meanwhile, the wave intensity varies little, too.

3.3.4 Effects of SIWs on material dispersion

Using passive tracers, I investigate the effect of SIWs on material dispersion. Initially, the tracer field C is uniform in the horizontal direction and increases linearly from the top ($z = 1$) to the bottom ($z = 0$), *i.e.* $C(z) = 1 - z$. After SIWs being emitted, the tracer outside the vortices is organized into spiral streaks (Fig. 3.17a) that have a pattern similar to SIWs. These streaks increase the horizontal gradients of tracer field, and thus can benefit material diffusion. However, in Exp. C1 no spiral streaks form (Fig. 3.17b), for no SIWs exist.

Moreover, I compute the vertical advection of tracer, which is $w \frac{\partial C}{\partial z}$ with w and C denoting the vertical velocity and tracer field, respectively. As shown in Fig. 3.18, lots of spiral streaks characterized by the large-magnitude $w \frac{\partial C}{\partial z}$ emerge in the wave field;

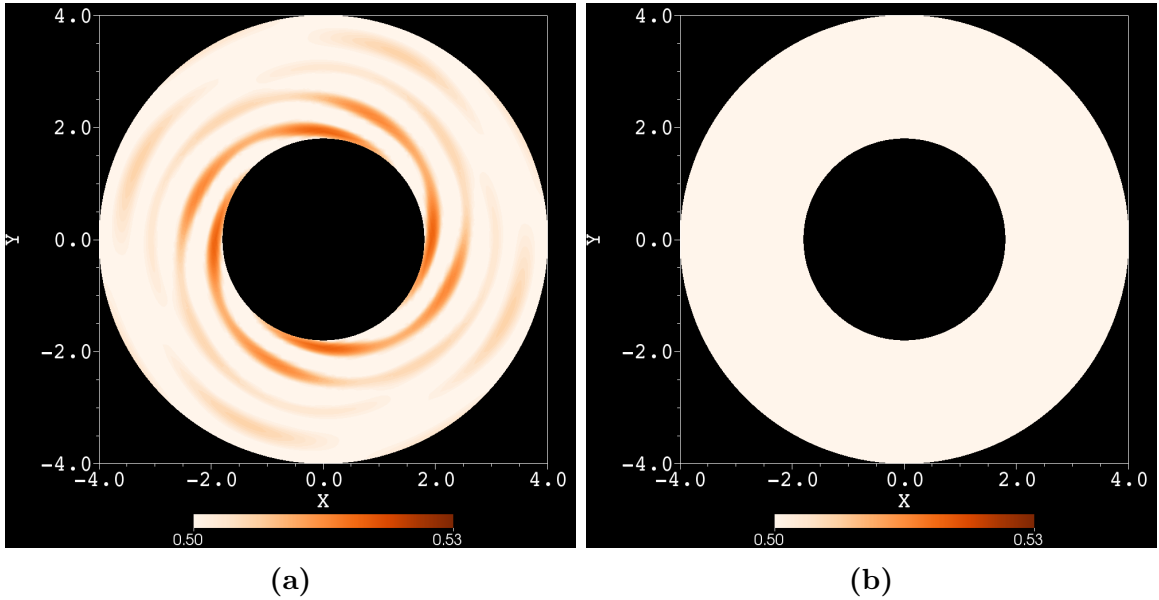


Figure 3.17: Tracer fields at mid-depth horizontal plane in (a) Exp. T1 and (b) Exp. C1 at time = 30. (The central regions occupied by the vortices are clipped to emphasize the outside wave field.)

the length scales of streaks are visually consistent with that of SIWs. The magnitude of $w \frac{\partial C}{\partial z}$ in Exp. T7 ($Ro = 1$) is larger than that in Exp. T1 ($Ro = 0.2$) due to the stronger wave intensity in Exp. T7 (*cf.* Fig. 3.12). However, no such features appear in Exp. C1, in which SIWs are absent. In the wave field, $w \frac{\partial C}{\partial z}$ is associated with the up and down motions of SIWs; thus according to Eq. (3.2), SIWs can modify the tracer's local rate of change ($\frac{\partial C}{\partial t}$) by advecting tracer vertically, instead of by mixing tracer directly, for the direct tracer mixing occurs at the moment of SIWs breaking. Besides, stronger wave intensities modify the rate more.

Also, Fig. 3.18 shows that in the same background flow but with different tracer diffusivities ($Pe = 10^4, 10^5$), the $w \frac{\partial C}{\partial z}$ has similar patterns and magnitudes. This result indicates that the vertical tracer advection by SIWs is insensitive to the tracer diffusivity (Pe); at least, there is no significant difference in $w \frac{\partial C}{\partial z}$ between $Pe = 10^4$ and $Pe = 10^5$.

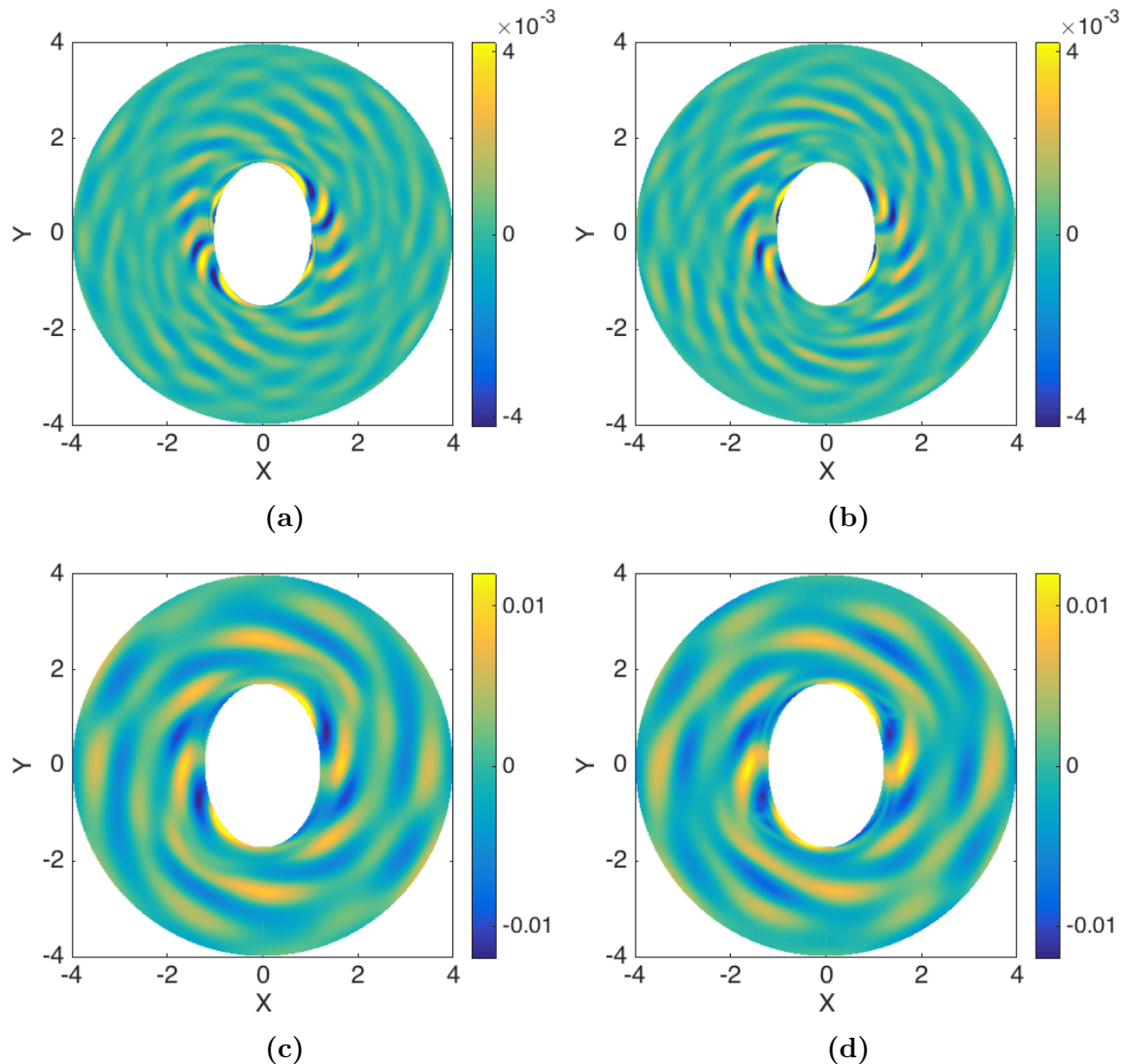


Figure 3.18: Snapshots of the vertical tracer advection by SIWs ($w \frac{\partial C}{\partial z}$), across mid-depth horizontal plane of (a,b) Exp. T1 and (c,d) Exp. T7; left column: $Pe = 10^4$, right column: $Pe = 10^5$. (The central regions occupied by the vortices are clipped to emphasize the outside wave field.)

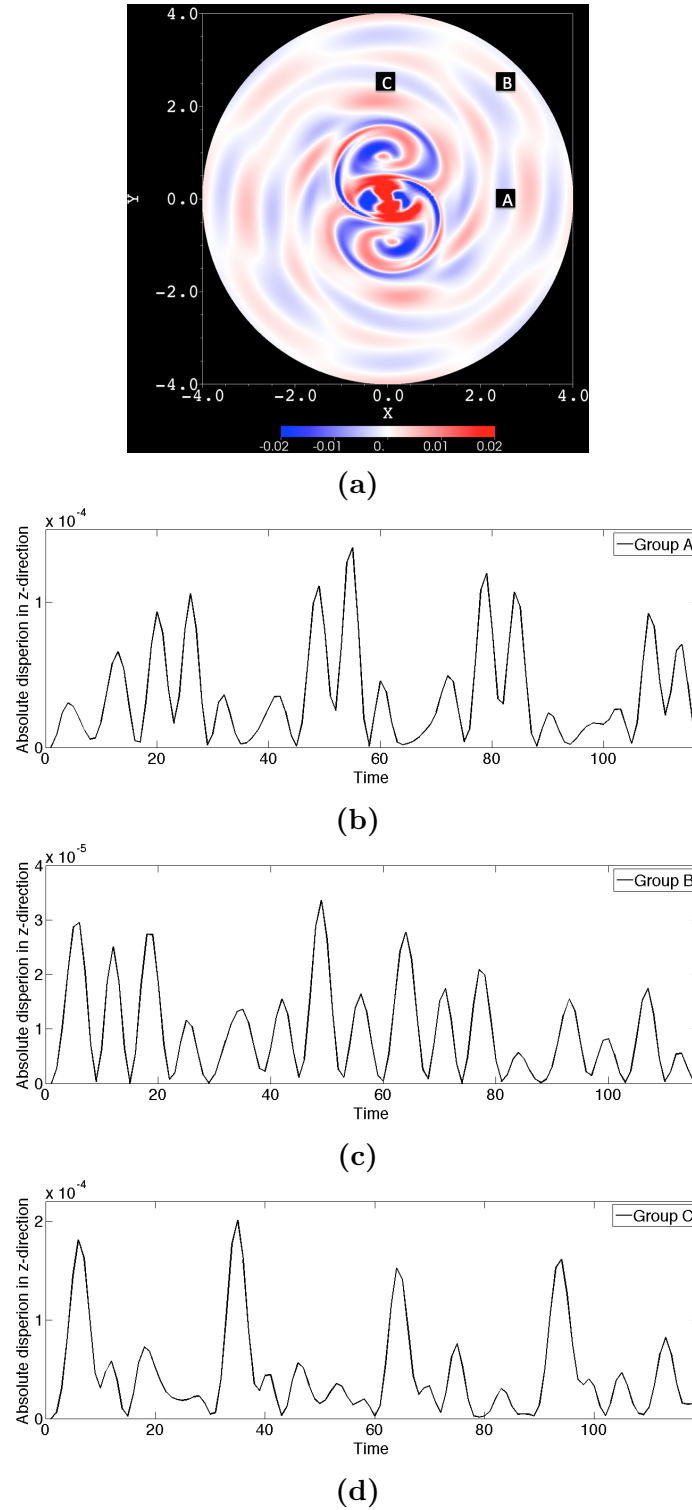


Figure 3.19: (a) Initial positions of particle groups A,B,C at the wave field of Exp. T7. (b,c,d) Evolutions of the absolute dispersion of particle groups A,B,C, respectively.

In addition to tracers, I adopt Lagrangian particles to investigate whether SIWs can produce a net vertical transport. In Exp. T7, for example, I release three groups of particles (A,B,C) centered on (2.5, 0, 0.5), (2.5, 2.5, 0.5), (0, 2.5, 0.5), respectively (Fig. 3.19a), at the final stage of evolution; then I monitor the evolution of particles' absolute dispersion in the vertical direction, lasting for two eddy-turnover times. This vertical absolute dispersion is defined by

$$A_z^2(t, t_0) = \frac{1}{M} \sum_{i=1}^M |z_i(t) - z_i(t_0)|^2 , \quad (3.15)$$

where M is the number of Lagrangian particles, z_i is the z-coordinate of the i -th particle; A_z quantifies the average vertical distance covered by particles. As shown in Figs. 3.19b,c,d, the evolutions of vertical absolute dispersion show oscillations, but the minimum dispersion remains almost unchanged (equal to zero); that is, during the two eddy-turnover times, particles move up and down due to SIWs, but do not produce a net vertical transport.

3.4 Discussion

Using numerical simulations of an unstable ocean eddy, I discover a special class of inertial waves, *i.e.* spiral inertial waves (SIWs), emitted in a spiral manner from a set of unsteady, non-axisymmetric geophysical vortices; this set of vortices is generated by the single unstable eddy. In particular, the generation of waves requires the vortices to be unsteady, and the formation of spiral patterns needs the eddies to be non-axisymmetric. In terms of the parameter sweep experiments on Rossby number, SIWs are only found at small Rossby numbers ($0.01 \leq Ro \leq 1$); also, SIWs change dramatically with different Rossby numbers, including the wavelength, wave frequency and wave amplitude. By an analysis similar to the theory of Lighthill-Ford radiation, I derive a wave source for the emission of inertial waves; the source term

can be used as an indicator of inertial wave emission, provided that the source satisfies two conditions, *i.e.* large source magnitude and source peak frequency lower than the inertial frequency.

The question whether these emitted spiral waves in the target experiments are pure inertial waves may be raised. Previous studies showed that if the fluid is stratified, vortex Rossby waves can excite inertia-gravity waves (Schecter and Montgomery 2004, 2006; Schecter 2008), which can also create spirals similar to those shown in Fig. 3.4d. But in the present study, I apply conditions of homogeneous density, rigid lid and flat bottom; thus, gravity waves are ruled out. Besides, vortex Rossby waves diminish outside of the vortices, as the mean potential-vorticity gradients vanish there (*cf.* Figs. 3.4a,c,e). In fact, there is a so-called stagnation radius, beyond which no vortex Rossby waves exist (Montgomery and Kallenbach 1997; Moon and Nolan 2010). The stagnation radius implies that vortex Rossby waves are restricted to the near-vortex region, rather than being emitted to the far field. Therefore, these spiral waves emitted into the far field are pure inertial waves.

In terms of Table 3.2, when Rossby number decreases, the wavenumber increases; I interpret this relation using the theory of wave capture (Bühler and McIntyre 2005). One result of this theory states that in a background flow with horizontal strain rate α , the wavenumber of a wave packet increases rapidly like $\exp(|\alpha|t)$. Thus, I would expect that for a finite time, the wavenumber is larger if the horizontal strain rate α is bigger. Now I examine the square of horizontal strain rate defined by $\alpha^2 = [(u_x - v_y)^2 + (v_x + u_y)^2]$. As is shown in Fig. 3.20, the magnitude of horizontal strain rate increases while Rossby number decreases; the regions of large strain rate locate at the ends of major axis of the elliptic vortex core. According to Fig. 3.14, these regions are also the leading wave sources; hence, the wavenumber of inertial

waves emitted from these regions, in view of the wave capture theory, increases when Rossby number decreases.

The linear relation between SIWs amplitude and Rossby number within [0.01, 0.2] (*cf.* Fig. 3.12a) was also reported by Williams *et al.* (2008), who observed inertia-gravity waves in a rotating, two-layer annulus laboratory experiment. Theoretically, at $Ro \ll 1$, ageostrophic effects can be expressed as the first order of Ro in an asymptotic expansion of governing equations (Pedlosky 1987). Therefore, I might expect that the amplitudes of ageostrophic motions, like inertial waves and inertia-gravity waves, are scaled as Ro^γ with $\gamma \geq 1$ (Williams *et al.* 2008); $\gamma = 1$ recovers the relation of linearity with Rossby number. Besides the algebraic scaling, exponential scalings were also derived for inertia-gravity waves generated through the breakdown of geostrophic balance, for instance $Ro^{-1/2}\exp(-\alpha/Ro)$ (Vanneste and Yavneh 2004). However, whether the exponential scalings are applicable to inertial waves needs a farther study.

I find a local maximum of inertial wave emission at $Ro = 0.4$ (*cf.* Fig. 3.12a); likewise, Sugimoto *et al.* (2008) also report a local maximum of inertia-gravity wave radiation at a moderate Rossby number, and suggested that the local maximum is caused by the shift of primary source. Indeed, as shown in Fig. 3.16, there is a shift of primary source between S_2 and S_3 around $Ro = 0.4$, where the maximum wave amplitude is observed. Therefore, our results confirm that the shift of primary source can amplify the wave emission. From another point of view, the maximum of wave emission at a moderate Rossby number is the result of competition between the dual effects of background rotation on wave emission. That is, at smaller Rossby number, the strong background rotation tends to suppress the vertical motions and thereby the wave emission (Ford *et al.* 2000); for instance, the wave emission is the weakest in Exp. T2 ($Ro = 0.01$). Nevertheless, at larger Rossby number, since inertial waves

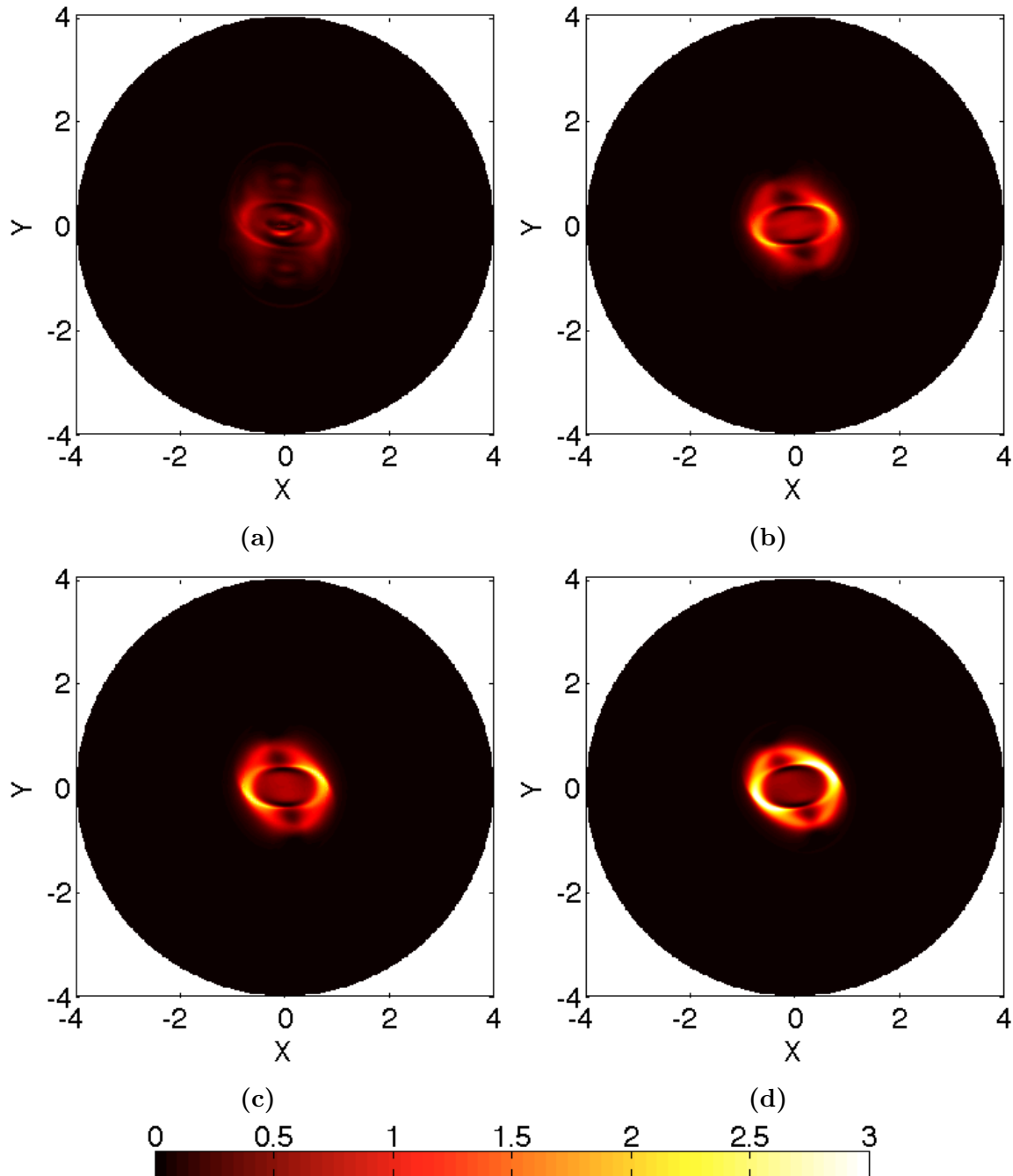


Figure 3.20: Snapshots of the square of horizontal strain rate on mid-depth horizontal plane in Exps. (a) T7 (b) T4 (c) T3 and (d) T2.

arise thanks to the Coriolis force, the weak background rotation (weak Coriolis force) damages the emission of inertial waves; for example, no inertial waves are observed in Exp. T8 ($Ro = 5$).

The theory of Lighthill-Ford radiation was tested by laboratory experiments of inertia-gravity wave radiation (*e.g.* Williams *et al.* 2005), and was adopted into practical applications, for example the forecast of clear-air turbulence (Knox *et al.* 2008). By extending the Lighthill-Ford radiation theory into inertial waves, I derive a wave source S given by Eq. (3.12) or Eq. (3.14). Since the source S does not include the dissipation due to fluid viscosity, the condition of $S \neq 0$ is necessary but not sufficient for the emission of inertial waves in viscous fluids like the ocean and atmosphere; in other words, the dissipation will weaken and may even eliminate inertial waves, particularly for $S \ll \mathcal{O}(1)$.

In addition to a wave source with $S \gg \mathcal{O}(1)$, the emission of inertial waves also requires that the peak frequency of wave source needs to be smaller than the Coriolis parameter f , which is the cut-off frequency of inertial waves. Otherwise, even though the wave source has $S \gg \mathcal{O}(1)$, the source still cannot emit inertial waves; for example in Exp. T8, no inertial waves are observed as the peak frequency of wave source is much larger than the cut-off frequency of inertial waves (*cf.* Fig. 3.15f). Similarly, in the study of inertia-gravity wave radiation, Sugimoto *et al.* (2008) and Sugimoto and Ishii (2012) pointed out that an important factor that determines the inertia-gravity wave radiation is the relative relation between the peak frequency of wave source and the cut-off frequency of inertia-gravity waves. Therefore, I suggest that if the wave source has $S \gg \mathcal{O}(1)$ and a peak frequency smaller than the cut-off frequency of inertial waves, the source can emit significant inertial waves that possess large amplitudes; if $S \leq \mathcal{O}(1)$, inertial waves may also be emitted, but are difficult to be detected due to small wave amplitudes.

At the final stage of vortex evolution, SIWs packets are emitted continuously and keep stationary relative to the tripolar vortices; that is, the phase speed of SIWs is equal to that of vortex Rossby waves, which control the rotation of vortices in our experiments. This relation of wave stationarity relative to the vortices was also documented in studies of inertia-gravity waves (*e.g.* Snyder *et al.* 2007; Snyder *et al.* 2009; Viúdez 2007, 2008; Wang *et al.* 2009). I interpret the relative stationarity based on the theory of interactions between long and short waves (Benney 1977). In the present context, this theory would express that owing to the resonant triad interactions, energy is transferred to SIWs (short waves) from vortex Rossby waves (long waves), if and only if the phase speed of SIWs is equal to that of vortex Rossby waves. Hence, only the waves that are stationary relative to the vortices can persistently acquire energy.

The asymmetry between cyclone and anticyclone under background rotation was found based on evidences, such as the evolution of vortex (*e.g.* Kloosterziel and van Heijst 1991), growth rate of vortical flow instabilities (*e.g.* Kloosterziel *et al.* 2007; Wang and Özgökmen 2015) and inertia-gravity wave radiation (*e.g.* Kuo and Polvani 2000; Sugimoto *et al.* 2015). According to the study of Sugimoto *et al.* (2015), this asymmetry comes from the source term that originates in the Coriolis force, *i.e.* the second term of wave source Eq. (3.13). Physically, the asymmetry is caused by the reverse of direction of Coriolis force between cyclone and anticyclone. Our study enriches the cyclone-anticyclone asymmetry in the subject of inertial wave emission. In Exps. T1 and T10, this asymmetry is elucidated by the wave amplitude and the variation along radius (Figure 3.21); particularly in the field of radius > 2 , SIWs emitted from the anticyclone have a larger amplitude. In fact, the phenomenon of stronger wave radiation from anticyclones was also found in inertia-gravity wave radiation (*e.g.* Snyder *et al.* 2007; Viúdez 2007; Wang *et al.* 2009; Sugimoto *et al.*

2015). In addition, this asymmetry is also manifested by the difference in magnitudes of wave sources between Exps. T1 and T10 at the final stage of vortex evolution (*cf.* Fig. 3.13c and Fig. 3.14a).

On the material dispersion, although SIWs do not produce a net vertical transport, they can generate tracer filaments (*cf.* Fig. 3.17a), which favor the tracer diffusion and therefore mixing. The tracer used in this study can represent materials such as salinity, temperature, dissolved gases, and nitrates; thus, I expect that SIWs can also benefit the mixing of these materials by creating filaments.

According to Fig. 3.17a, SIWs organize the tracer into spiral streaks, which are similar to some spiral features observed in the ocean and atmosphere, such as spiral sea eddies (*e.g.* Munk *et al.* 2000; Ivanov and Ginzburg 2002) and spiral hurricane rainbands (*e.g.* Willoughby 1978; Gall, Tuttle and Hildebrand 1998). However, the formation mechanisms of these spiral features are controversial. For example, it was argued that the baroclinic or frontal instability is responsible for the development of spiral eddies (Munk *et al.* 2000; Eldevik and Dysthe 2002); nevertheless, Shen and Evans (2002) interpreted the spiral eddies using inertial instability without density anomaly, which is crucial for the frontal or baroclinic instability. Similar for spiral rainbands, there are also debates on the formation mechanism, like the inertia-gravity wave (*e.g.* Kurihara 1976; Willoughby 1978) and vortex Rossby wave (*e.g.* Guinn and Schubert 1993; Montgomery and Kallenbach 1997; Chen and Yau 2001). In this study, based on the similarity between the spirals of SIWs and the observed spiral features, I suggest that SIWs offer another way to generate these spiral eddies and rainbands. However, our experiments exclude the density anomaly, which may cause gaps between numerical experiments and the reality. On the other hand, our results imply that the density anomaly is not necessary to generate spiral features; further,

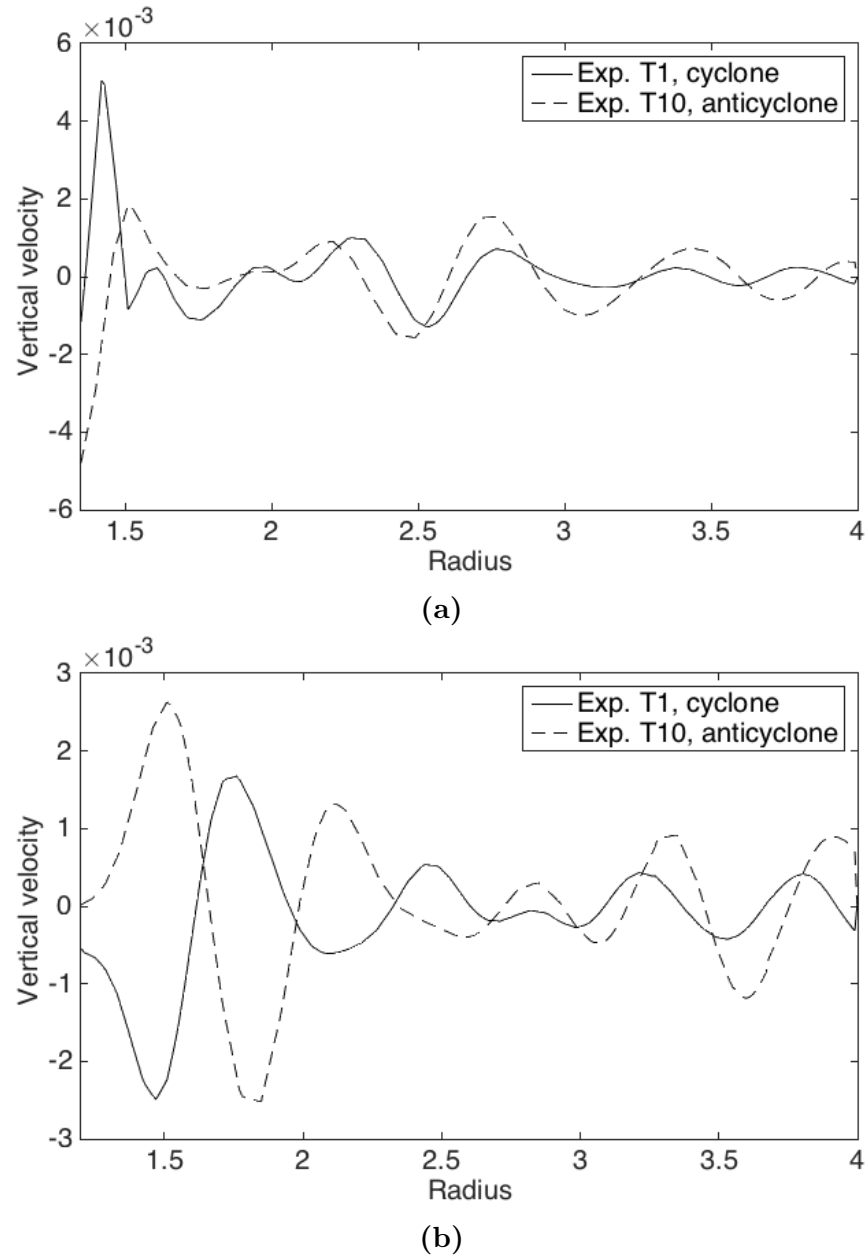


Figure 3.21: Vertical velocity in the wave field on the (a) $\theta = 0$ and (b) $\theta = \pi/2$ section (θ is the angle coordinate of the cylindrical frame) at mid-depth in Exps. T1 and T10, at the final stage of vortex evolution.

I infer that the baroclinic or frontal instability is unlikely to play a key role in the formation of spiral features.

Last, I argue that the parameterization of inertial waves need to be considered in general circulation models, particularly in modelling well-mixed flows. As the parameter regimes (Ro, Re) used in our numerical experiments are relevant to real geophysical flows, the indicator S for the emission of inertial waves can be applied into the general circulation models. A possible procedures is as follows. Compute the wave source at each time step, and check whether the magnitude of wave source is beyond the threshold and whether the peak frequency of wave source is below the cut-off frequency. Then activate the parameterization only in regions where all the aforementioned conditions are satisfied.

Chapter 4

Lagrangian dispersion by ocean internal gravity waves

4.1 Overview

In this chapter, using numerical simulations, I investigate the material dispersion by ocean internal gravity waves. First, I initialize a 3D internal wave field with the Garrett-Munk spectrum (Garrett and Munk 1975), which is the universal spectrum of internal waves observed in the open ocean; then, I let the internal waves evolve without inputting any wave source, and release particles to identify the dispersion regimes. These numerical experiments can represent the scenario that internal waves with GM spectrum from open ocean propagate into an area away from the wave sources, producing material dispersion there. Also, I explore whether the internal waves below an upper mixed layer can cause the material dispersion in mixed layers, and which kind of dispersion regime can be generated under both internal waves and mixed layer eddies.

This chapter is organized as follows. Section 4.2 describes the numerical model and the method of initializing an internal gravity wave field with the Garrett-Munk spectrum; the results are analyzed in Section 4.3.

4.2 Method

4.2.1 Numerical model

Our numerical experiments are conducted with NEK5000, which is a numerical solver for Navier-Stokes equations using the spectral element method (*e.g.* Patera 1984; Fischer 1997). NEK5000 has been adopted to study geophysical fluid dynamics, including submesoscale instabilities (*e.g.* Özgökmen *et al.* 2012), chaotic advection inside an ocean eddy (Pratt *et al.* 2014; Rypina *et al.* 2015), hydrodynamic instabilities of a geophysical vortex (Wang and Özgökmen 2015) and spiral inertial waves (Wang and Özgökmen 2016).

NEK5000 is configured to integrate the dimensionless Boussinesq equations:

$$\frac{\partial \mathbf{u}}{\partial t} + (\mathbf{u} \cdot \nabla) \mathbf{u} = -\nabla p - \frac{1}{Ro} \hat{\mathbf{z}} \times \mathbf{u} - \frac{1}{Fr^2} \rho' z \hat{\mathbf{z}} + \frac{1}{Re} \nabla^2 \mathbf{u}, \quad (4.1a)$$

$$\nabla \cdot \mathbf{u} = 0, \quad (4.1b)$$

$$\frac{\partial \rho'}{\partial t} + (\mathbf{u} \cdot \nabla) \rho' = \frac{1}{Pe} \nabla^2 \rho'. \quad (4.1c)$$

The Rossby number is given by $Ro = U/(fL)$, where U and L are the characteristic scales of horizontal velocity and horizontal length; here I choose the maximum horizontal velocity of internal waves as the U , and use the maximum horizontal wavelength as the L . $f = 2\Omega$ is the Coriolis parameter, with Ω being the angular velocity of the background rotation. The Froude number is defined as $Fr = U/NH$, where N is the buoyancy frequency and H is the maximum vertical wavelength. The Reynolds number is given by $Re = UL/\nu$, where ν is the kinematic viscosity.

$Pe = UL/\kappa$ is the Péclet number and κ is the molecular diffusivity of density. $\mathbf{u} = (u, v, w)$ is the velocity in the x, y, z direction, p is the pressure, and ρ' is the density anomaly. $\hat{\mathbf{z}}$ is the unit vector in the vertical direction, and operator $\nabla = (\frac{\partial}{\partial x}, \frac{\partial}{\partial y}, \frac{\partial}{\partial z})$.

In addition to Eq. (4.1), other two equations for passive tracer and Lagrangian particles are solved by NEK5000; that is, the advection-diffusion equation (4.2) for the passive tracer:

$$\frac{\partial C}{\partial t} + (\mathbf{u} \cdot \nabla)C = \frac{1}{Pe} \nabla^2 C , \quad (4.2)$$

and the Lagrangian advection equation (4.3) for passive, neutrally buoyant particles:

$$\frac{d\mathbf{x}}{dt} = \mathbf{u} , \quad (4.3)$$

where \mathbf{x} is the particle position.

The numerical domain (Fig. 4.1) is a cylinder with diameter $D_c = 52$ km and height $H_c = 2.6$ km. The domain is discretized into $K = 2560$ quadrilateral elements; on each element, the solutions are approximated by Legendre polynomials with order $N_p = 17$, which generates $K(N_p + 1)^3 = 14,929,920$ grid points. The grid spacing is uneven, ranging from 0.39 m to 459 m; denser grid points locate at boundaries to resolve fine scale motions due to potentially high flow shears there. The boundary conditions are free-slip on the top and bottom, and no-slip on the sidewall.

4.2.2 Initialization of Garrett-Munk internal waves

Internal waves observed in the open ocean have a much universal spectrum, unless the observations are made close to a strong source of internal waves (Gill 1982). This spectrum, now known as Garrett-Munk (GM) spectrum, provides a good basis for

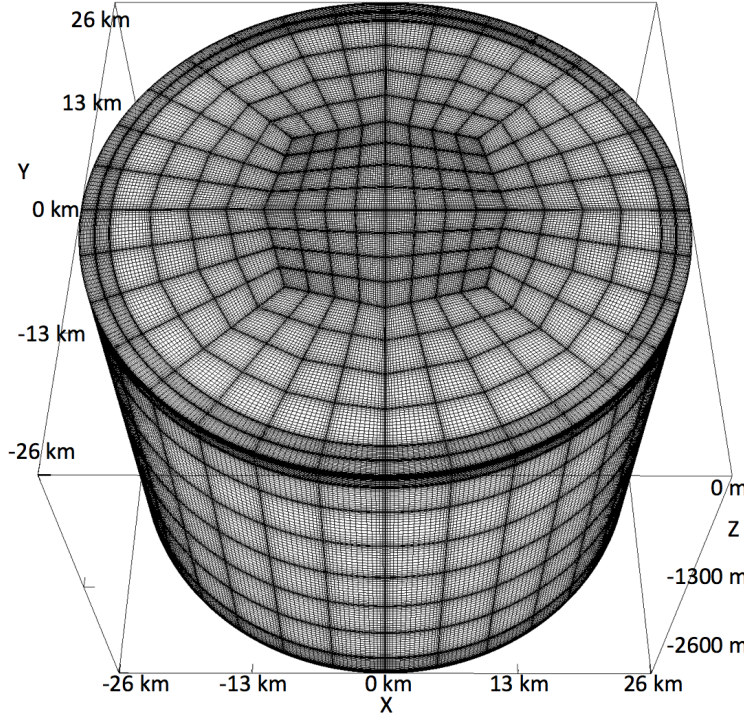


Figure 4.1: The cylindrical domain used in the numerical experiments. (Vertically stretched image)

internal wave studies; therefore, I initialize an internal wave field that has a GM-like frequency spectrum.

The Munk (1981) version of GM spectrum is chosen as the reference, describing the frequency spectrum of horizontal velocity as:

$$E(\omega, j) = \frac{2b^2 f N_0 N E_{GM}}{\pi} \frac{\omega^2 + f^2}{\omega^3 \sqrt{\omega^2 - f^2}} \sum_{j=1}^{\infty} \frac{(j^2 + j_*^2)^{-1}}{(j^2 + j_*^2)^{-1}}, \quad (4.4)$$

where ω is the internal wave frequency and j is the vertical mode number; other parameters are listed in Table 4.1. As $f \ll \omega \ll N$, the spectrum $E \propto \omega^{-2}$.

Table 4.1:
Parameters used in the GM spectrum.

$f = 7.3 \times 10^{-5}$ rad s $^{-1}$	Coriolis frequency at 30° N
$N_0 = 50$, $f = 3.7 \times 10^{-3}$ rad s $^{-1}$	reference buoyancy frequency
$N(z) = N_0 e^{z/b}$	depth-dependent buoyancy frequency
$b = 1300$ m	stratification depth scale
$E_{GM} = 6.3 \times 10^{-5}$	dimensionless spectral energy level
$j_* = 3$	peak vertical mode number
$K_{zc} = \frac{1}{3Ri_c j_* b E_{GM}}$	cutoff vertical wavenumber
$Ri_c = 2$	Richardson number at K_{zc}

I initialize a GM internal wave field using the method proposed by Sun and Kunze (1999), called Monte-Carlo simulation of a GM internal wave field. The procedure is as follows: Treating the spectrum in Eq. (4.4) as a probability density function, I use the Monte-Carlo method to find the random sampling schemes for intenal wave frequency ω , vertical mode number j , and wave amplitude. For example, to sample wave frequency ω , I extract the term, $(\omega^2 + f^2)/(\omega^3 \sqrt{\omega^2 - f^2})$, from Eq. (4.4) to construct a random sampling scheme. Rewrite this term as

$$\frac{\omega^2 + f^2}{\omega^3 \sqrt{\omega^2 - f^2}} = (1 + \frac{f^2}{\omega^2}) \frac{1}{\omega \sqrt{\omega^2 - f^2}} ; \quad (4.5)$$

the term, $(1 + \frac{f^2}{\omega^2})$, will be used to constrain the wave amplitude. Now, I integrate and normalize the other term, $\frac{1}{\omega \sqrt{\omega^2 - f^2}}$, yielding

$$\frac{\int_f^\omega \frac{1}{\omega \sqrt{\omega^2 - f^2}} d\omega}{\int_f^{N_0} \frac{1}{\omega \sqrt{\omega^2 - f^2}} d\omega} = \frac{\arccos(f/\omega)}{\arccos(f/N_0)} = \text{rand}(e) , \quad (4.6)$$

where $\text{rand}(e)$ represents a random number in $[0, 1]$. Inverting Eq. (4.6) for ω , I obtain the random sampling scheme for the wave frequency

$$\omega = \frac{f}{\cos[\arccos(f/N_0)\text{rand}(e)]} . \quad (4.7)$$

Using similar procedures, I can find random sampling schemes for the vertical mode number j , and wave amplitude. Then, I sample 10,000 wave frequencies ω , vertical mode numbers j , and wave amplitudes; after having the wave frequency and vertical mode number, I determine the horizontal wavenumber based on the dispersion relation of inertia inertial gravity waves, with the direction of horizontal wave vector $\theta = \arctan(K_y/K_x)$ randomly chosen from $[0, 2\pi]$ to ensure the horizontal isotropy, where (K_x, K_y) are the horizontal wavenumber in (x, y) direction. With 10,000 sets of wave frequency, wavenumber and wave amplitude, I construct 10,000 waves that are summed up to generate a 3D internal wave field. For more details of the initialization of a Garrett-Munk internal wave field, readers may refer to the paper by Sun and Kunze (1999).

As shown in Fig. 4.2, the frequency spectrum of the initialized internal wave field displays a spectral slope of -2 between $f < \omega < N$, which is consistent with GM spectrum (Garrett and Munk 1975), including the steep change within the near-inertial frequency range ($\omega \sim f$). Besides, in this spectrum, the energy peaks at the inertial frequency f , and sharply cuts off at the buoyancy frequency N (Garrett and Munk 1979).

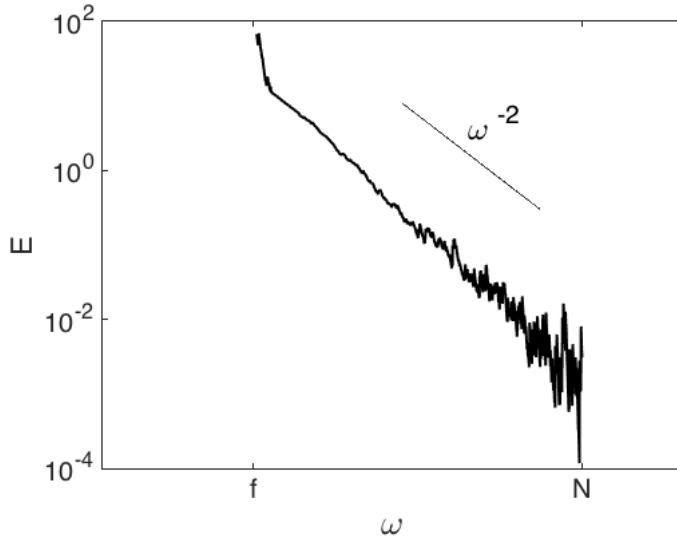


Figure 4.2: The frequency spectrum of the initial internal waves.

4.3 Analysis of material dispersion

I design three numerical experiments that are distinct by the initial density field. In the Exp.-1 (Fig. 4.3b), the density field is linearly stratified; in the Exp.-2 (Fig. 4.3c), the density field has a upper mixed layer with a depth of 140 m, and a pycnocline below the mixed layer; in the Exp.-3 (Fig. 4.3d), the density field has the mixed layer with that of the Exp.-2, but also possess a circular front, which later will generate a cyclonic eddy in the mixed layer. Exp.-1 is designed to investigate which kind of dispersion regimes can be produced by pure internal waves, in the absence of other flow features such as currents and eddies; Exp.-2 is used to explore whether the internal waves below a mixed layer can cause material dispersion in the mixed layer, which is initially in rest; Exp.-3 is adopted to study the dispersion regime under the occurrence of both internal waves and mixed layer eddies.

Next, I input the GM internal wave field initialized by the method stated in Section 4.2.2, and let the waves evolve without adding any wave source. This kind of internal wave simulations represents the scenario that internal waves with GM

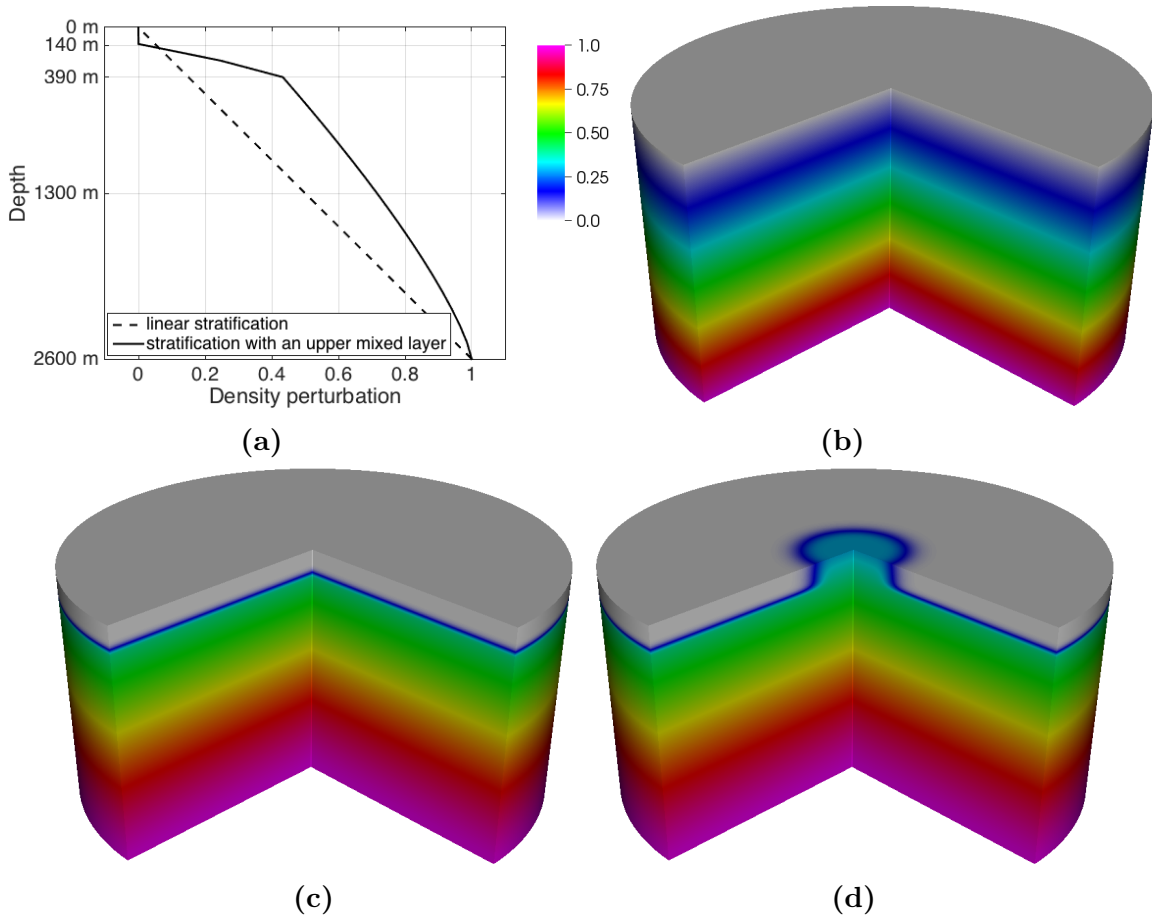


Figure 4.3: (a) Vertical profiles of the initial density field in Exp.-1 and Exp.-2. The 3D distribution of initial density field in (b) Exp.-1 with a linear stratification, (c) Exp.-2 with an upper mixed layer, and (d) Exp.-3 with a circular front inside the upper mixed layer.

spectrum, say from open ocean, propagate into a region away from the wave sources. As for Exp.-2, I only input the internal waves below the mixed layer; later, these waves will create motions in the mixed layer, which is in rest initially. Exp.-2 is used to explore how the internal waves affect the material dispersion in upper mixed layer.

I visualize the waves using the isosurface of density; as is shown in Fig. 4.4, two density isosurfaces are displayed: the lower isosurface is around the mid-depth of the entire fluid, and the upper one is inside the pycnocline (near the base of mixed layer); in Exp.-1, the upper isosurface simply represents the sub-surface. It seems that the ups and downs of density isosurface have similar amplitude at the middle fluid depth for all three experiments; while inside the pycnocline of Exp.-2, the ups and downs of density isosurface are weaker than that at the sub-surface of Exp.-1, due to strong stratification of the pycnocline, which suppresses the vertical movement of density isosurface. In addition, the wave kinetic energy is calculated at different depths for each experiment (Table 4.2), and agrees with the aforementioned statement made in terms of the visual ups and downs of density isosurface. Physically, internal waves in the upper layer or pycnocline are close to the rigid-lid boundary, and therefore they are suppressed.

Table 4.2:

(Dimensionless) Internal wave kinetic energy at different depths, one day after initialization.

Experiment number	Mid-depth	Depth within the pycnocline (upper layer)
Exp.-1	1.8	0.82
Exp.-2	1.3	0.48
Exp.-3	1.4	0.49

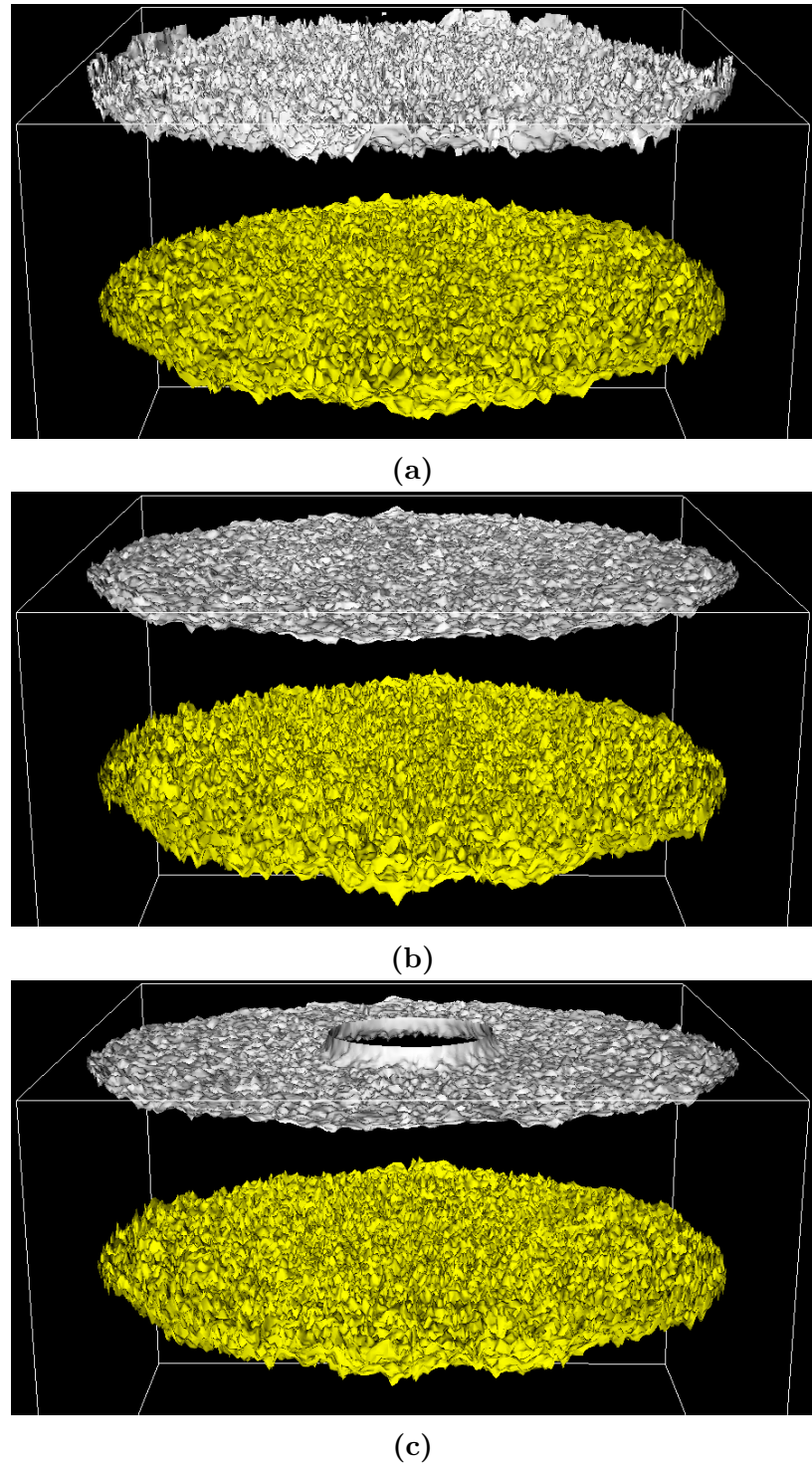


Figure 4.4: Isosurface of density in (a) Exp.-1, (b) Exp.-2 and (c) Exp.-3 at one day after initialization.

After the initialization of internal gravity waves, material dispersion is investigated based on two metrics, which are the relative dispersion and FSLE. Both metrics use trajectories of particle pairs for analysis; thus, I release 19,845 particles into the internal waves in the form of particle triplets; each triplet consists of two particle pairs with an initial separation of 117 m. Particles are released at three representative depths: $D1 = 65$ m inside the mixed layer (or sub-surface), $D2 = 208$ m inside the pycnocline layer (or upper layer), and $D3 = 1300$ m at the mid-depth of entire fluid (Fig. 4.5a). At each depth, particles are divided into five groups (Fig. 4.5b); particularly in Exp.-3, the central particle group A released in the mixed layer well locates inside the circular front (*cf.* Fig. 4.3d).

4.3.1 Experiment with linear stratification (Exp.-1)

4.3.1.1 Relative dispersion analysis

I use Exp.-1 to investigate the dispersion regime produced by only internal waves, without any other features such as currents and eddies. Particles are advected by the fully 3D velocity of internal waves; note that without specific statement, all particles are advected by 3D full velocity. Take the particles released at the mid-depth as an example; in comparison with Fig. 4.5b, Fig. 4.6 shows that these particles are remarkably dispersed by internal waves. In the horizontal plane (*cf.* Fig. 4.6a), particles expand in all directions; for some groups like the group D (colored purple), particles experiences a stretching in a preferable direction, forming a “tail” as observed in the lower part of group D. In the vertical direction (*cf.* Fig. 4.6b), particles are pushed upwards and downwards, up to several hundreds of meters. In addition, particles released at other two depths exhibit visually similar patterns of dispersion as that at the mid-depth (Figs. 4.6c and 4.6d).

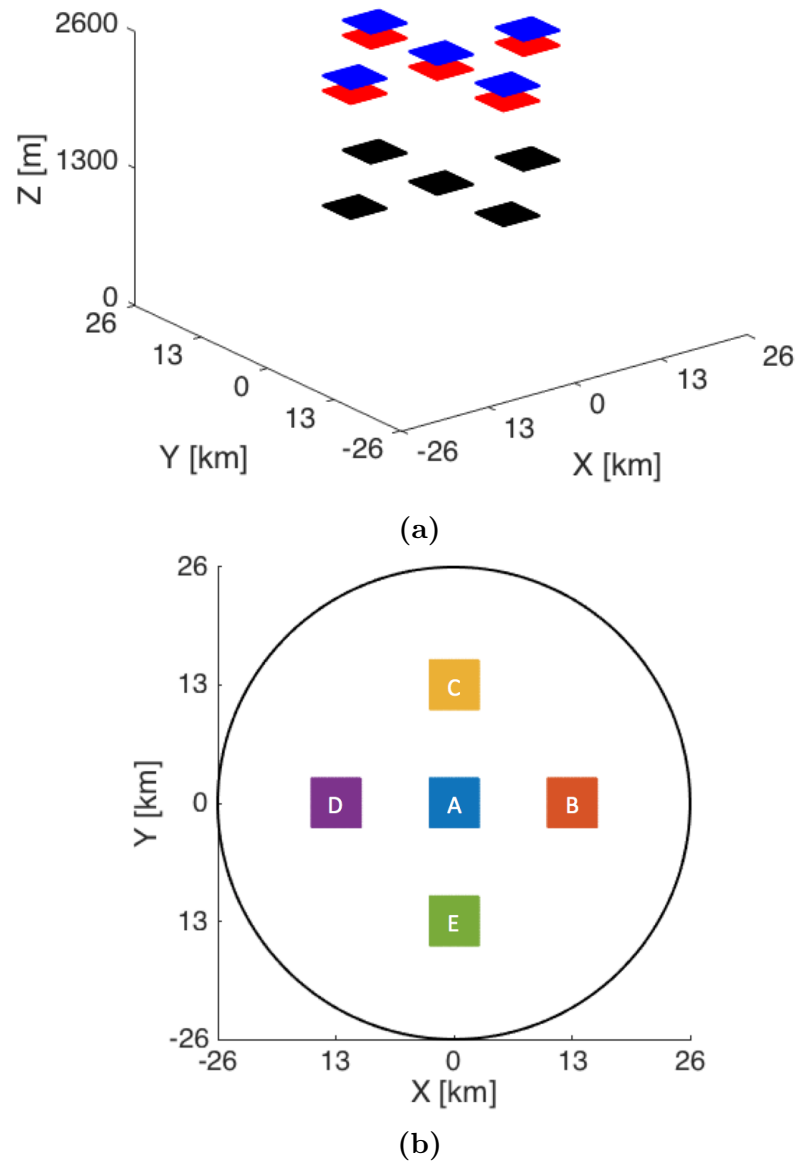


Figure 4.5: (a) Particles released at three depths. (b) Particle distribution at each depth; the circle represents the domain boundary.

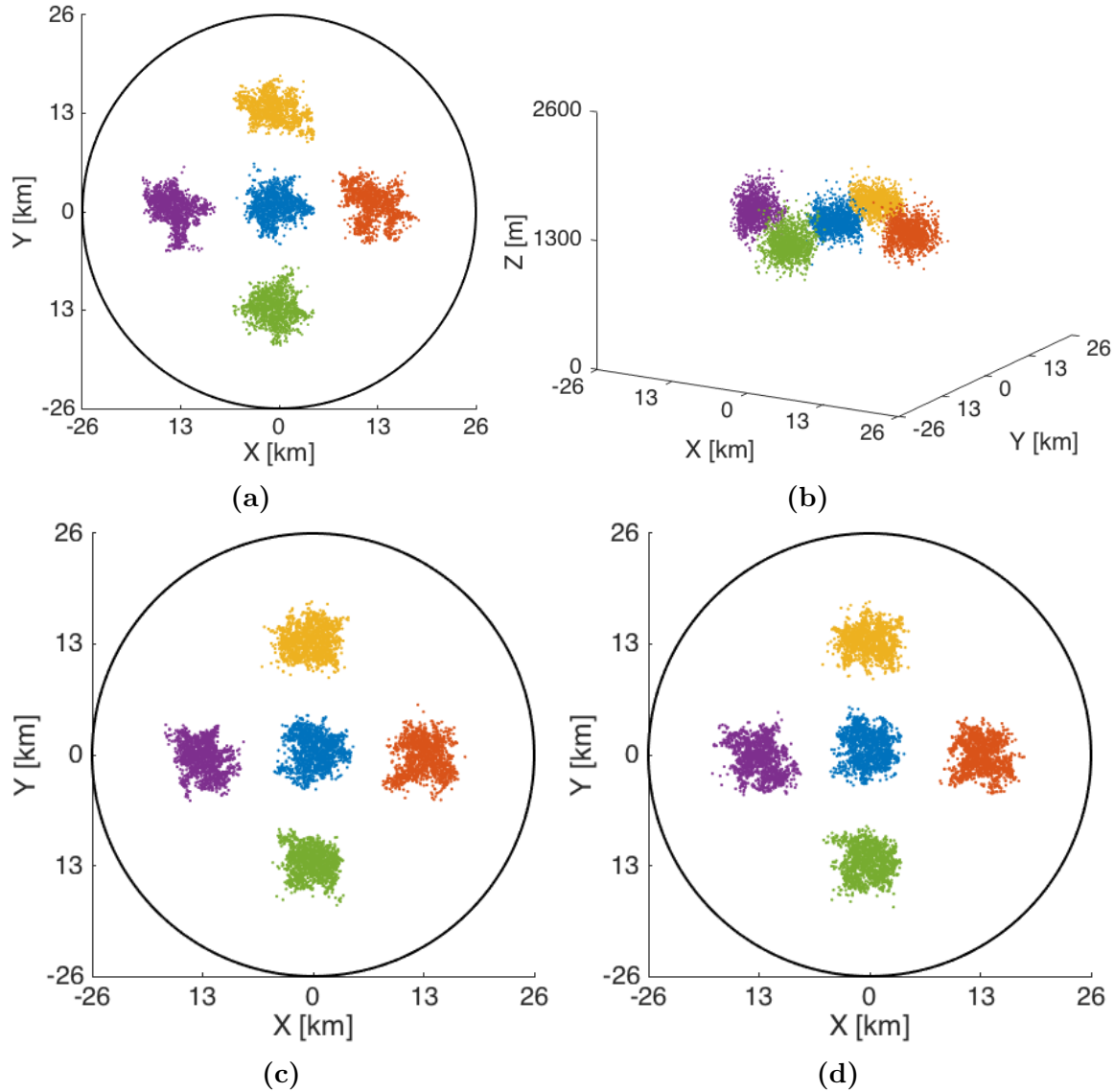


Figure 4.6: Positions of particles in Exp.-1 at 6.3 days after the release at mid-depth (1300 m), with (a) 2D view and (b) 3D view; also, positions of particles released at (c) upper layer (208 m) and (d) sub-surface (65 m) in 2D view.

Quantitatively, I use the metric of relative dispersion to identify the dispersion regime. As shown in Fig. 4.7a, the five curves of relative dispersion, which is computed from five particle groups released at the mid-depth, show nearly the same dependence on time, for instance $D^2 \propto t^{1.5}$ and $D^2 \propto t$. Thus the five particle groups experience the same dispersion regimes, and further I infer that the dispersion regimes at this mid-depth are independent of the release location of particles. However, the value of relative dispersion at the same temporal scale varies with different particle group, implying that the dispersion rate relies on where particles are released. Moreover, the analysis of relative dispersion at other two depths reveals the same results as that at the mid-depth.

The average relative dispersion that is computed based on all particle pairs released at the same depth (*cf.* Fig. 4.7a), sufficiently represents the dispersion behavior of five particle groups; hereafter, the average relative dispersion is adopted for Exp.-1 analysis. According to Figs. 4.7b and 4.7c, the three curves of average relative dispersion at three depths behave similar: The relative dispersion grows exponentially in time (exponential regime with $D \propto e^{6t}$), lasting about 0.1 days after the release of particles (Fig. 4.7b); then, it transits to a regime scaling as $D^2 \propto t^{1.5}$ (Fig. 4.7c), which is between the ballistic regime and diffusive regime. After about 1 day, the relative dispersion enters into the diffusive regime, scaling as $D^2 \propto t$ (Fig. 4.7c).

4.3.1.2 FSLE analysis

In addition to the metric of relative dispersion that separates dispersion regimes in terms of temporal scales, I adopt the FSLE metric, which interprets dispersion regimes based on spatial scales. As shown in Fig. 4.8a, for each of the five particle groups, FSLE is calculated using the 3D-advection trajectories of particles that are released at the middle fluid depth. The FSLE curves $\lambda(\delta)$ calculated from each group have almost the same slope of -1 , though the values of λ at the same δ change

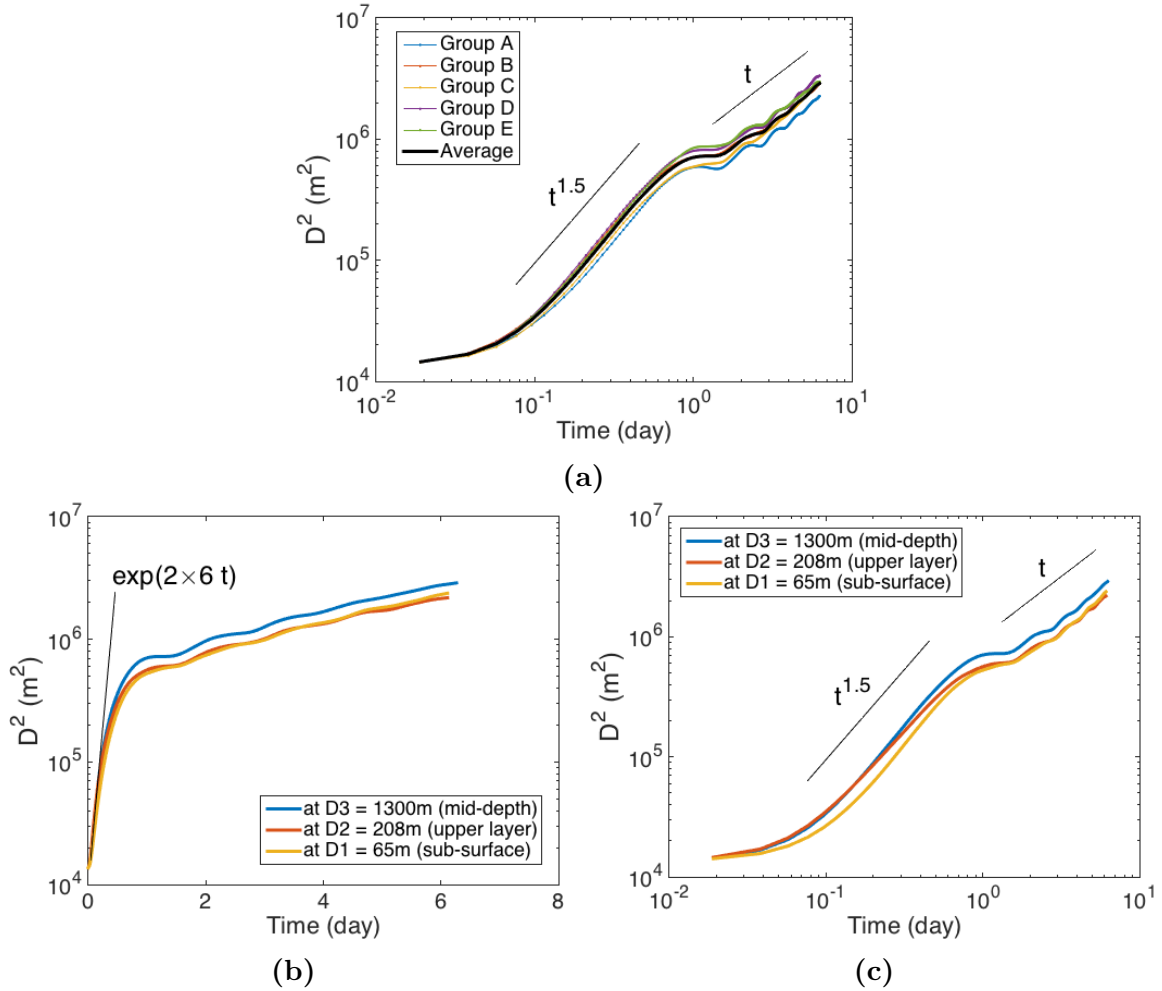


Figure 4.7: Relative dispersion for Exp.-1: (a) at the middle fluid depth (log-log frame), five curves of relative dispersion is computed from five particle groups; the thick black curve is the average relative dispersion over all particle pairs of five groups. Average relative dispersion for each of three depths is shown in (b) semi-log frame and (c) log-log frame. The black thin line in (b) indicates the exponential regime of $D^2 \propto e^{12t}$.

with different particle groups. The same slope of FSLE curves means that the five particle groups experience the same dispersion regimes, and further indicates that the dispersion regime at the mid-depth does not rely on the release locations of particles. However, the different values of λ in different particle groups imply that the dispersion rate depends on where particles are released. Besides, the analysis of particles released at other two depths shows the same results as particles released at the mid-depth.

The average FSLE curve that is calculated based on all particle pairs released at the same depth (*cf.* Fig. 4.8a), well represents all the FSLE curves from the five particle groups; hereafter, the average FSLE is used for the Exp.-1 analysis. Three average FSLE curves computed from 3D-advection trajectories at three depths are displayed in Fig. 4.8b; the FSLE curves at all three depths (*i.e.* mid-depth, upper layer and sub-surface) exhibit the same scale dependence of δ^{-1} , *i.e.* the ballistic regime.

In addition to the 3D advection, particles are also advected by 2D horizontal velocity and 1D vertical velocity, respectively; as displayed in Fig. 4.8c, the FSLE curves are calculated based on the 2D-advection and 1D-advection trajectories. The values of FSLE from 2D and 1D trajectories are smaller than that from 3D trajectories; that is, in this internal waves, the dispersion rate by 2D horizontal velocity or 1D vertical velocity is smaller than that by 3D full velocity. Because the dispersion in 3D advection consists of both horizontal dispersion and vertical dispersion, after the same amount of advection time, the dispersion in 3D advection is larger, and thereby larger dispersion rate or FSLE.

According to Fig. 4.8c, the 1D vertical velocity can separate particles up to the distance of $\delta = 450$ m. At separation distances beyond 450 m, the dispersion is driven by the 2D horizontal velocity. The FSLE curve from 2D advection does not converge with that from 3D advection at large distance scales is due to the reason mentioned

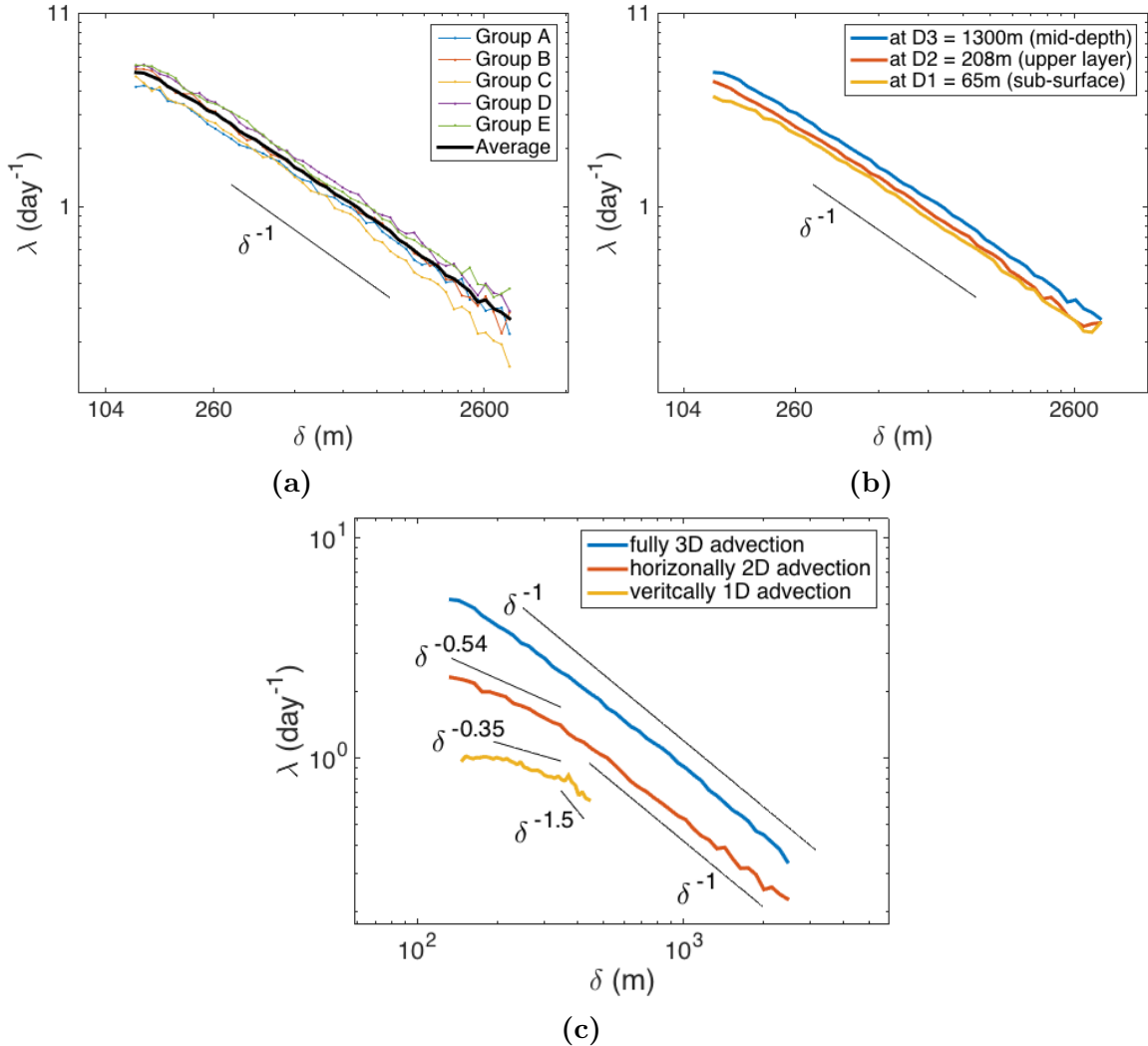


Figure 4.8: FSLE curves in Exp.-1: (a) FSLE calculated using 3D-advection trajectories of the five particle groups at the middle fluid depth; the thick black curve is the average FSLE over the five groups. (b) Average FSLE at three depths, from 3D-advection particles trajectories. (c) Average FSLE at middle fluid depth, from particles trajectories advected by 3D full velocity, 2D horizontal velocity, and 1D vertical velocity.

earlier; that is, 3D dispersion also contains the dispersion by vertical velocity, thus larger FSLE.

Moreover in terms of Fig. 4.8c, the FSLE computed based on 3D-advection particles trajectories indicates a nearly identical ballistic regime ($\lambda \propto \delta^{-1}$) for separation distances in the range of $120 \leq \delta \leq 2800$ m. However, FSLE from 2D- and 1D-advection trajectories shows a transition of dispersion regime at separation distance around $\delta = 350$ m: In 2D advection, the dispersion regime transits from $\lambda \propto \delta^{-0.54}$ to ballistic regime ($\lambda \propto \delta^{-1}$); in 1D advection, the dispersion regime transits from $\lambda \propto \delta^{-0.35}$ to the regime of $\lambda \propto \delta^{-1.5}$.

4.3.2 Experiment with mixed layer (Exp.-2)

4.3.2.1 Relative dispersion analysis

An upper mixed layer, along with a pycnocline below the mixed layer, is initialized in Exp.-2 (*cf.* Fig. 4.3c). The mixed layer is motionless initially; later, weak fluid motions are generated by the below internal waves continuously hitting the base of the mixed layer, leading to dispersion there.

As shown in Fig. 4.9, particles released at different depths exhibit quite different dispersion patterns. Clearly, particles released at the mid-depth have the largest expansion (Fig. 4.9a), while particles released at the mixed layer show the smallest dispersion (Fig. 4.9c). Interestingly, the dispersion at the mid-depth in Exp.-2 displays similar patterns as that in Exp.-1 mid-depth (*cf.* Fig. 4.6a), including the vertical dispersion; this results implies that the dispersion at mid-depth is barely affected by the added upper mixed layer. As for the dispersion in the mixed layer, though very weak, it demonstrates that the below internal waves can cause dispersion in the mixed layer. In the vertical direction, the dispersion at the pycnocline and mixed layer is greatly depressed, due to the strong stratification of the pycnocline.

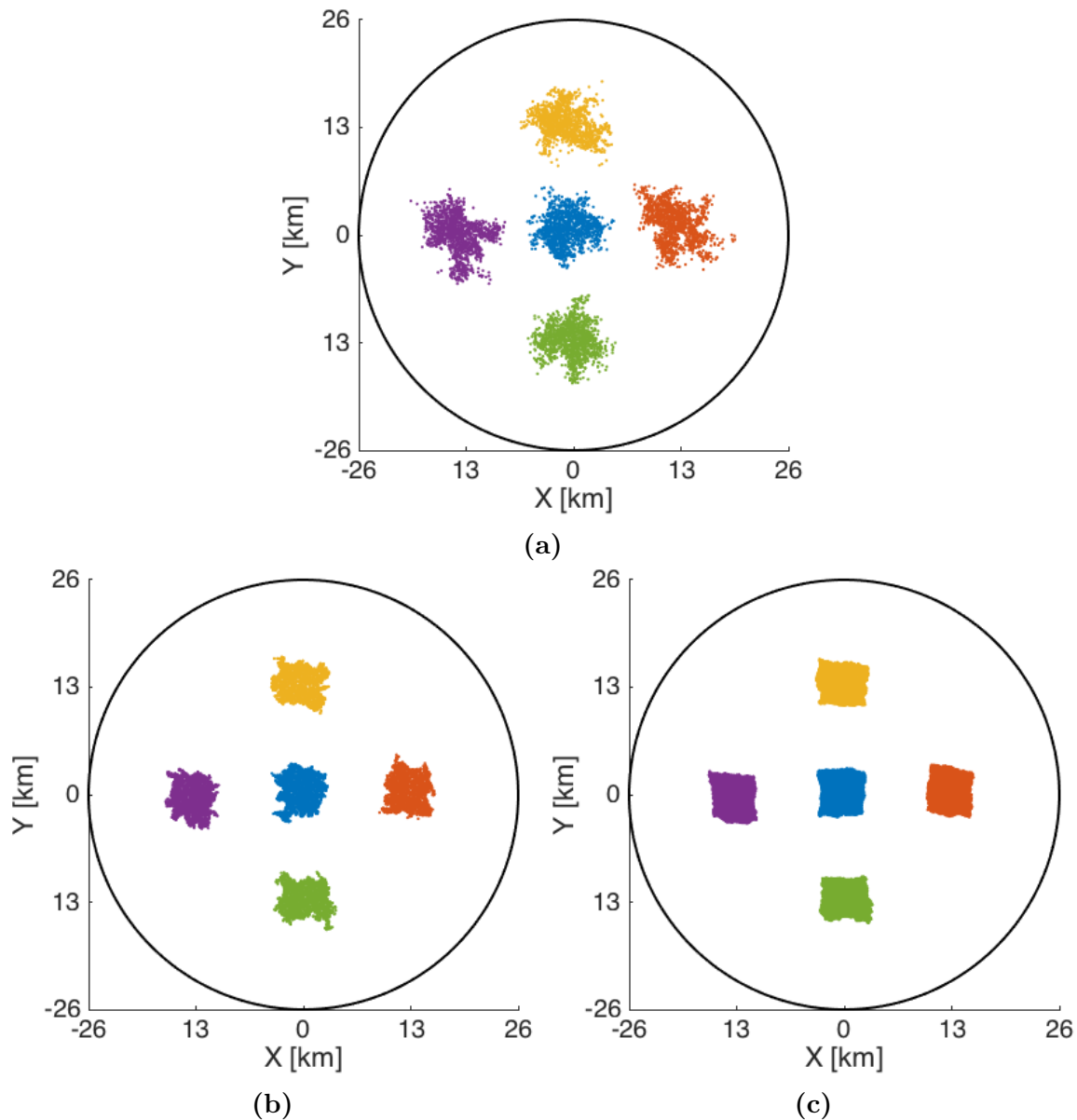


Figure 4.9: Positions of particles in Exp.-2 at 7.4 days after the release at (a) mid-depth (1300 m), (b) pycnocline (208 m) and (c) mixed layer (65 m) in 2D view.

Then I use the relative dispersion to separate dispersion regimes. Like the Exp.-1, the relative dispersion, as well as FSLE, calculated from each of the five particle groups have the similar behaviors; thus, the following analysis of Exp.-2 is also based on the average over the five particle groups. As shown in Figs. 4.10a and 4.10b, the dispersion at mid-depth have the same transitions of dispersion regimes as that in Exp.-1 (*cf.* Figs. 4.7b and 4.7c), from exponential regime ($D \propto e^{6t}$) to the regime of $D^2 \propto t^{1.5}$, then to diffusive regime ($D^2 \propto t$). The relative dispersion at the pycnocline also experiences an exponential regime ($D \propto e^{0.15t}$) first but with a much smaller dispersion rate than that at the mid-depth; at 3 days after release, it transits to a diffusive regime. At the mixed layer, the weak flow generated by the below internal waves produces a small relative dispersion: At first, the dispersion fits an exponential regime with a very low dispersion rate of 0.018 day^{-1} ; then at about 7 days after release, it gradually transits to the regime of $D^2 \propto t^{0.3}$.

4.3.2.2 FSLE analysis

According to Fig. 4.10c, the FSLE curves at three depths have different spans of spatial scale. The FSLE curve at the mid-depth owns the longest spatial span, whereas the curve at mixed layer has the shortest spatial span. This result is consistent with the relative dispersion shown in Figs. 4.10a and 4.10b. Since particle pairs at the mid-depth have the largest relative dispersion, they can separate to a larger distance, leading to their FSLE curve occupying a longer spatial span.

Unlike the Exp.-1 where the FSLE curves at all three depths have the same slope (*cf.* Fig. 4.8b); in Exp.-2, the FSLE curves at each depth have different slopes, indicating different dispersion regimes (*cf.* Fig. 4.10c). In the middle depth, the FSLE has the scale dependence of $\lambda \propto \delta^{-1}$, indicating the ballistic dispersion regime in terms of spatial scales; in the pycnocline, the dispersion regime transits from $\lambda \propto \delta^{-0.45}$ to

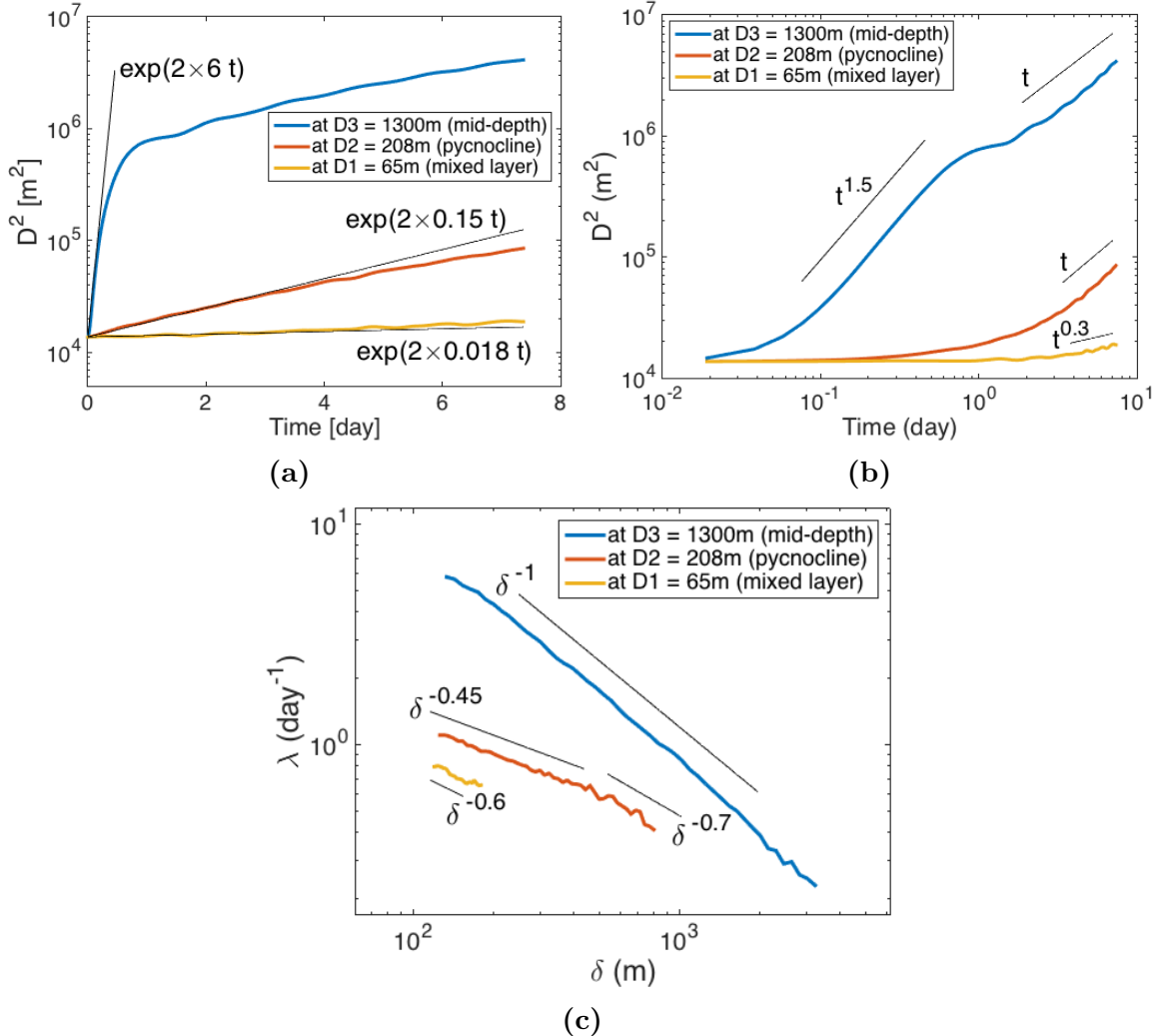


Figure 4.10: Relative dispersion in Exp.-2 at three depths in the (a) semi-log frame and (b) log-log frame, along with (c) FSLE curves at three depths in Exp.-2. Each curve in (a,b,c) represent the average over all the five particle groups released at the same depth.

$\lambda \propto \delta^{-0.7}$ at separation distance $\delta > 500$ m; in mixed layer, the FSLE indicates the dispersion regime of $\lambda \propto \delta^{-0.6}$, which is close to the Richardson regime ($\lambda \propto \delta^{-2/3}$).

In addition, the magnitudes of FSLE change a lot with different depths; for example, around separation distance $\delta = 100$ m, the FSLE at mid-depth is about one order of magnitude larger than that at the mixed layer and pycnocline (*cf.* Fig. 4.10c). This result agrees with the relative dispersion, whose magnitudes also change a lot with different depths during the same amount of advection time (*cf.* Figs. 4.10a and 4.10b), implying a large difference in dispersion rate (*e.g.* FSLE). Further, the magnitude of FSLE in the mixed layer is comparable with that in pycnocline, suggesting that the internal waves have a noticeable effect on material dispersion in the mixed layer.

4.3.3 Experiment with front in mixed layer (Exp.-3)

4.3.3.1 Relative dispersion analysis

In Exp.-3, the initialized circular front (*cf.* Fig. 4.3d) in the mixed layer drives a cyclonic eddy (Figs. 4.11a and 4.11c). At the early period of the eddy evolution, its shape is nearly circular, symmetric; as the eddy is interacting the internal waves, the baroclinic instability is triggered, reshaping the circular eddy (Figs. 4.11b and 4.11d).

The central particle group A (*cf.* Fig. 4.5b) is released inside the eddy (*cf.* Fig. 4.11a); hence, influenced by both the mixed layer eddy and internal waves, this particle group exhibits a very different dispersion pattern (Figs. 4.12b and 4.12c) than that in Exp.-2 (*cf.* Figs. 4.9b and 4.9c). While, the four surrounding particle groups display a similar dispersion pattern to that in Exp.-2, for they are away from the central eddy. Particularly at the mid-depth, the dispersion pattern (Fig. 4.12a) looks similar to that in Exp.-2 (*cf.* Fig. 4.9a); this result implies that the mixed layer eddy has little effect on the dispersion at the mid-depth.

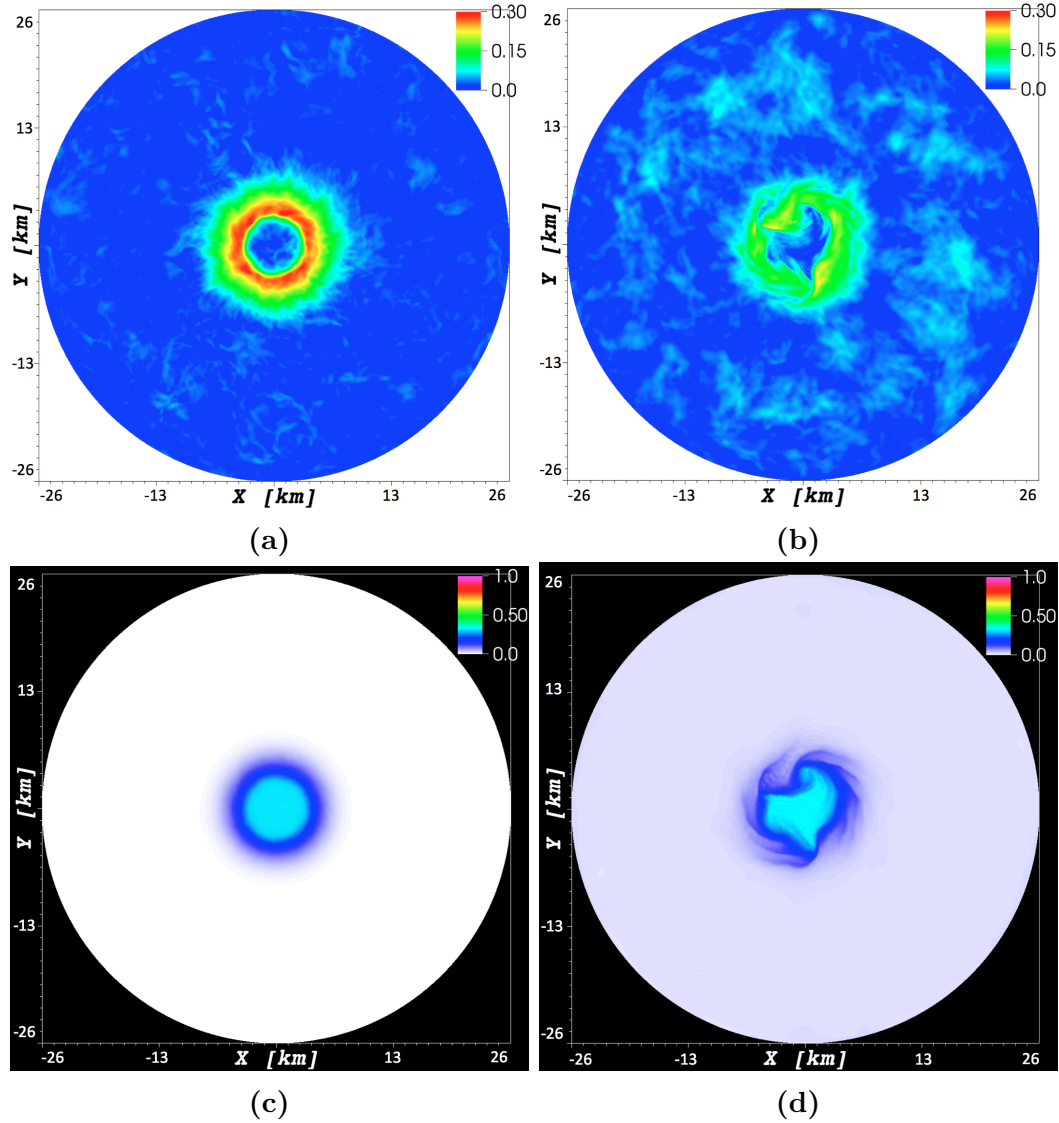


Figure 4.11: Velocity magnitude at the surface in Exp.-3 at (a) 0.5 days and (b) 7.4 days. Density field at the surface at (c) 0.5 days and (d) 7.4 days.

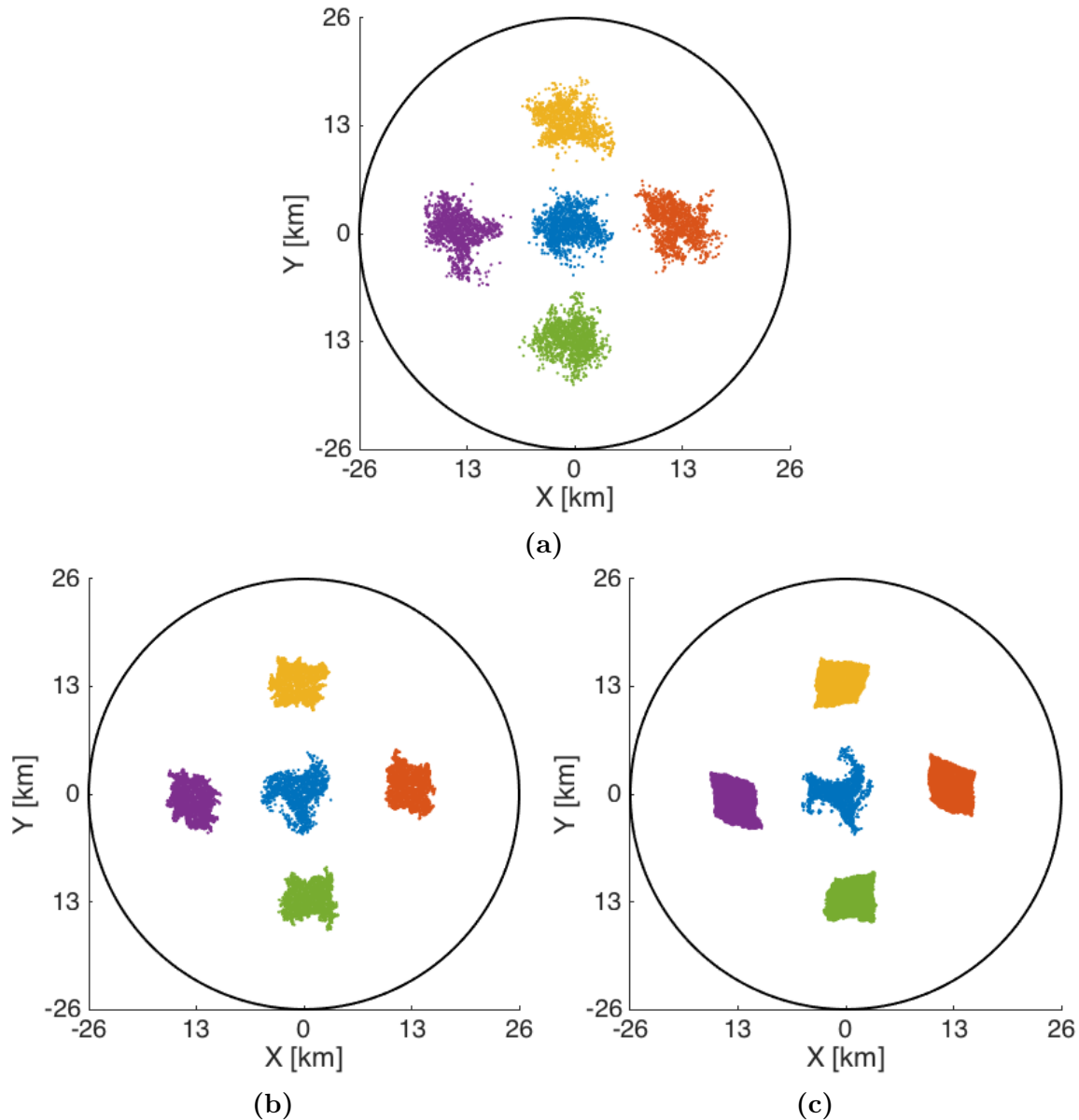


Figure 4.12: Positions of particles in Exp.-3 at 7.4 days after the release at (a) mid-depth (1300 m), (b) pycnocline (208 m) and (c) mixed layer (65 m) in 2D view.

Likewise, I use the relative dispersion to identify the dispersion regime. As shown in Fig. 4.13a, the relative dispersion at mid-depth behaves similar to that in Exp.-2 mid-depth (*cf.* Fig. 4.10b) and in Exp.-1 mid-depth (*cf.* Fig. 4.7a); in particular, the dispersion of central particle group (A) behaves similar to its four surrounding groups (B-E). This result further demonstrates that the relative dispersion at mid-depth is hardly affected by the mixed layer eddy. However, at the pycnocline, the central group (A) has a much stronger relative dispersion than its surround groups (B-E) according to Fig. 4.13b. As the four surrounding particle groups (B-E) have similar dispersion, hereafter I use their average relative dispersion (and FSLE) for the dispersion analysis at pycnocline and mixed layer in Exp.-3.

At the pycnocline (Figs. 4.13c and 4.13d), the dispersion regimes that the four surrounding particle groups (B-E) go through are nearly the same with that in Exp.-2 (*cf.* Figs. 4.10a and 4.10b), such as the exponential regime ($D \propto e^{0.15t}$) at the beginning and the later diffusive regime ($D^2 \propto t$). Nevertheless, the central group (A) greatly affected by the mixed layer eddy undergoes different dispersion regimes. Initially, the regime is also an exponential one but with a much larger dispersion rate ($D \propto e^{1.5t}$), for a duration about 0.5 days; then, it gradually transits to the ballistic regime ($D^2 \propto t^2$).

Similarly at the mixed layer (Figs. 4.13e and 4.13f), the four surrounding particle groups also have almost the same relative dispersion as that in Exp.-2 (*cf.* Figs. 4.10a and 4.10b), for instance, the exponential regime ($D \propto e^{0.018t}$) and the regime of $D^2 \propto t^{0.3}$. However, the central group (A) have a very different dispersion. The relative dispersion decreases first; afterwards, it increases in time, close to an exponential dispersion regime ($D \propto e^{0.018t}$); around 6 days, the dispersion transits to the Richardson regime ($D^2 \propto t^3$).

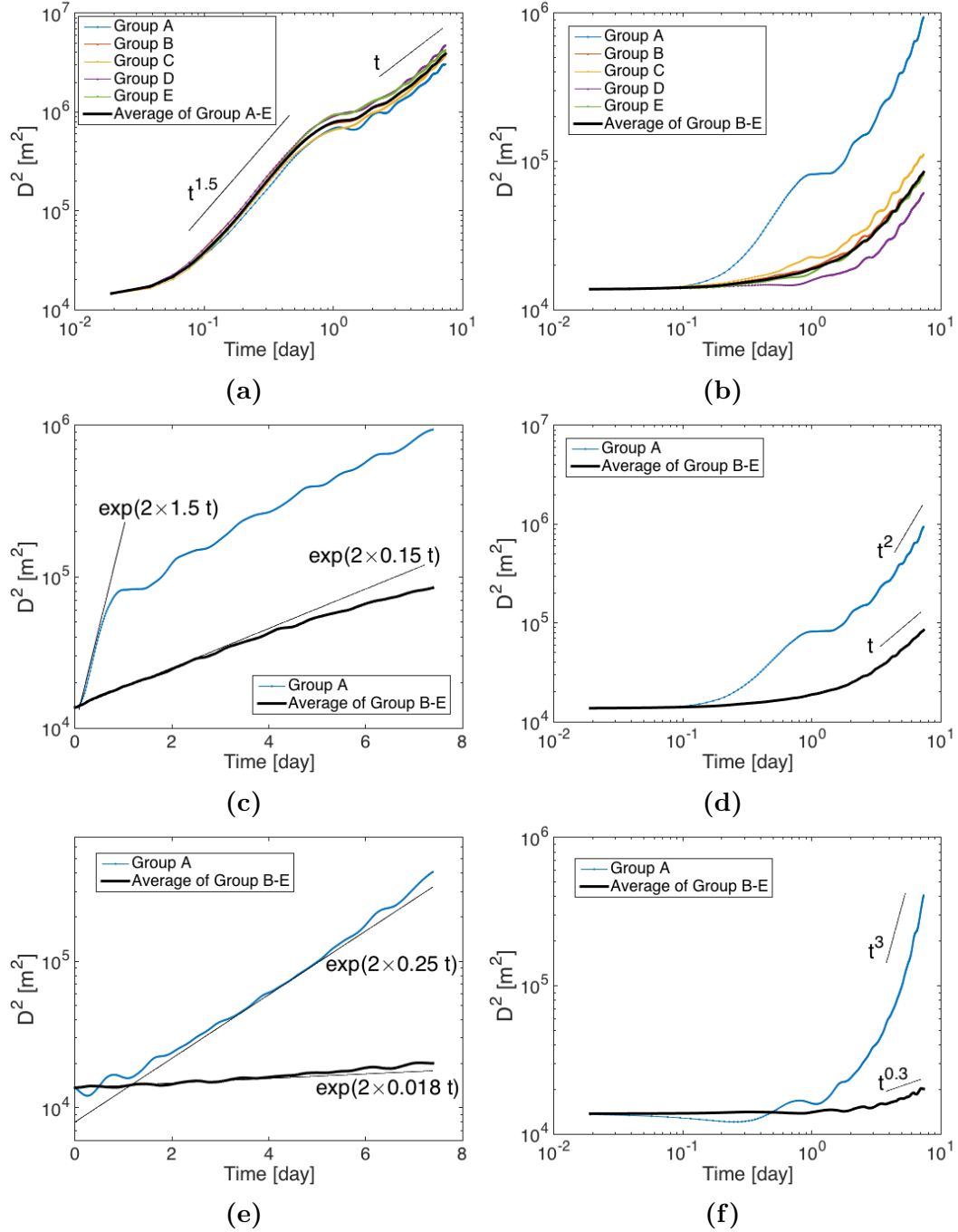


Figure 4.13: Relative dispersion from each particle group released (a) at the middle depth, with the black curve indicating the average over all the five groups (A-E), and (b) at the pycnocline, with the black curve representing the average over the four surrounding groups (B-E). Relative dispersion at the pycnocline in (c) semi-log frame and (d) log-log frame. Relative dispersion at the mixed layer in (e) semi-log frame and (f) log-log frame. In (c,d,e,f), the black thick curves represent the average of the four surrounding groups (B-E).

The relative dispersion at the pycnocline and mixed layer reveals that the mixed layer eddy remarkably increases the dispersion of particles released inside the eddy, whereas barely affects the dispersion of particles released outside away from the eddy, during the period of numerical simulation.

4.3.3.2 FSLE analysis

As shown in Fig. 4.14a, the FSLE curves at the mid-depth share the same slope (-1) as that in Exp.-2 mid-depth (*cf.* Fig. 4.10c) and in Exp.-1 mid-depth (*cf.* Fig. 4.8a), including almost the same magnitudes of FSLE and the spatial spans in δ . This result further confirms that the mixed layer eddy hardly affects the dispersion at the middle depth.

However, at the pycnocline and mixed layer (Figs. 4.14b and 4.14c), in comparison with the average FSLE curve over the four surrounding particle groups (B-E), the FSLE curve of the central group (A) shows different characteristics, such as the larger spatial span and larger magnitude of FSLE, manifesting the effects of the mixed layer eddy on the dispersion. The eddy greatly increase the dispersion of the central group, making particle pairs separate a larger distance; accordingly, the FSLE curve of the central group occupies a larger spatial span. Also, within the same advection time, larger dispersion means a higher dispersion rate, which yields a larger magnitude of FSLE.

Moreover, at the pycnocline and mixed layer (*cf.* Figs. 4.14b and 4.14c), the FSLE averaged over the four surrounding groups indicates nearly the same dispersion regime as that in Exp.-2 corresponding depths (*cf.* Fig. 4.10c). This result also implies that the mixed layer eddy has little effect on the dispersion of the four surrounding particle groups that are released outside away from the eddy.

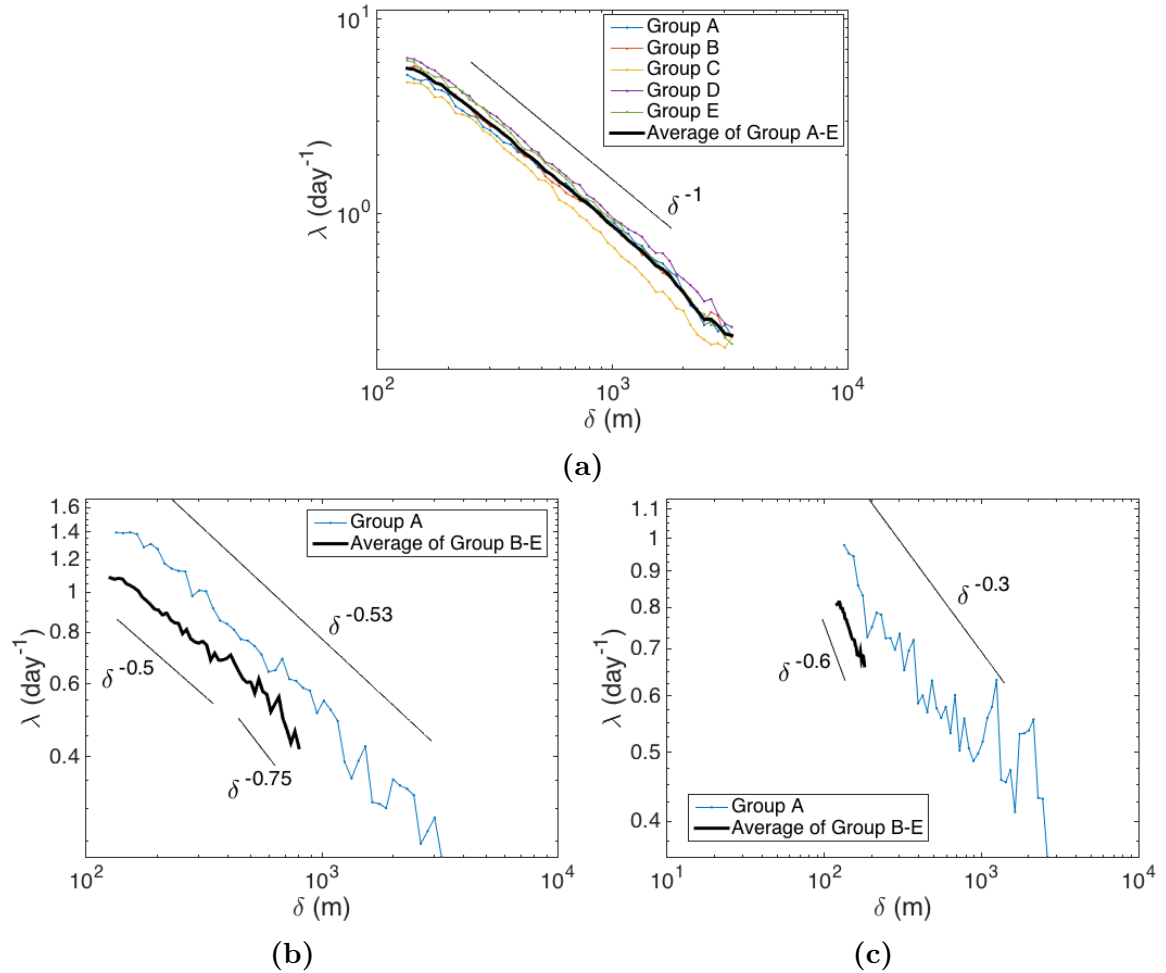


Figure 4.14: FSLE curves in Exp.-3: (a) At the mid-depth; the black curve represents the average over all the five groups (A-E). (b) At the pycnocline, and (c) at the mixed layer; the black curves in (b,c) represent the average over the four surrounding groups (B-E).

Chapter 5

Conclusions

In the present work, I investigate the material dispersion by ocean eddies, inertial waves and internal gravity waves, using both analytical methods and numerical simulations. I conclude my work in this chapter, and extend the conclusions further to connect with the real ocean flows.

On the material dispersion by ocean eddies, I focus on the unstable eddies; using the normal-mode analysis, I derive formulas of the growth rate of barotropic, inertial and 3D instabilities in geophysical vortices. Based on these formulas, some questions can be (partially) answered, such as the exponential growth of the wavenumber-1 barotropic instability, vorticity skewness of oceanic submesoscale turbulences, and growth rate of non-axisymmetric/asymmetric perturbations in 3D instability. Through numerical simulations, I investigate the joint impacts of hydrodynamic instabilities on 3D material dispersion in ocean eddies. I discover for the first time that material circulates within a family of vortices created by instabilities of a single, initially unstable vortex. This material circulation is accomplished by 3D pathways that connect the central and satellite vortices as a united system. The finding implies the trap of biogeochemical tracers (*e.g.* nutrients) inside the ocean

eddies in close proximity. Additionally, I propose a new kinetic energy wavenumber spectrum to interpret the non-classic power-law regimes (such as k^{-2} , $k^{-7/3}$ and $k^{-8/3}$), by introducing a parameter that bridges the gap between fully 3D turbulence and purely 2D turbulence. In other words, the energy spectrum can represent the 3D-2D transition in rotating turbulence.

On the material dispersion by inertial waves, I conclude that SIWs do not produce a net vertical material transport, based on the absolute dispersion of particles released in the SIWs field; on the other hand, in terms of the passive tracer experiment, SIWs can generate spiral tracer filaments, which increase the overall tracer gradients, enhancing mixing. Besides, the spiral filaments are resemble to some spiral features observed in the ocean and atmosphere, such as spiral ocean eddies and spiral hurricane rainbands; the formation mechanism of these spiral features are still on debate. According to the similarity of spiral patterns, the SIWs may provide another formation mechanism for these spiral features; further, since no density anomaly is required to generate the spirals of SIWs, I infer that the density anomaly and thereby baroclinic or frontal instability is unlikely to be the key factor in the formation of these spiral features.

On the material dispersion by internal gravity waves, I examine the dispersion regimes produced by ocean internal waves, using three numerical experiments. According to Exp.-1, internal waves generate similar dispersion regimes at depths of sub-surface, upper layer and mid-depth. Based on Exp.-2, I find that internal waves that are initially below an upper mixed layer can produce flows in the mixed layer, causing dispersion. Exp.-3 is used to investigate the dispersion under both internal waves and mixed layer eddies. The major dispersion regimes observed in three experiments are summarized in Table 5.1 (in terms of relative dispersion) and Table 5.2 (in terms of FSLE).

Table 5.1:

List of the major dispersion regimes in terms of relative dispersion ($D \propto e^{\gamma t}$ and $D^2 \propto t^\alpha$) for all the experiments. The stack of dispersion regimes indicates the regime transition from the top to bottom.

Depth	Exp.-1	Exp.-2	Exp.-3	
			Outside the eddy	Inside the eddy
Mid-depth	e^{6t}	e^{6t}	e^{6t}	e^{6t}
	$t^{1.5}$	$t^{1.5}$	$t^{1.5}$	$t^{1.5}$
	t	t	t	t
Pycnocline (Upper layer)	e^{6t}	$e^{0.15t}$	$e^{0.15t}$	$e^{1.5t}$
	$t^{1.5}$	t	t	t^2
	t			
Mixed layer (Sub-surface)	e^{6t}	$e^{0.018t}$	$e^{0.018t}$	$e^{0.25t}$
	$t^{1.5}$	$t^{0.3}$	$t^{0.3}$	t^3
	t			

Table 5.2:

List of the major dispersion regimes in terms of FSLE ($\lambda \propto \delta^\beta$) for all the experiments. The stack of dispersion regimes indicates the regime transition from the top to bottom.

Depth	Exp.-1	Exp.-2	Exp.-3	
			Outside the eddy	Inside the eddy
Mid-depth	δ^{-1}	δ^{-1}	δ^{-1}	δ^{-1}
Pycnocline (Upper layer)	δ^{-1}	$\delta^{-0.45}$	$\delta^{-0.5}$	$\delta^{-0.53}$
		$\delta^{-0.7}$	$\delta^{-0.75}$	
Mixed layer (Sub-surface)	δ^{-1}	$\delta^{-0.6}$	$\delta^{-0.6}$	$\delta^{-0.3}$

In this dissertation, all the numerical experiments are idealized and are performed in a cylindrical domain using NEK5000; however, the results from these experiments can be applied into the real ocean, guiding the study of real ocean.

In the real ocean, the family of unstable eddies like the tripolar eddies in Chapter 2, may not maintain together for a long time; therefore, I do not expect a complete overturning circulation. Nevertheless, the result shows that when an unstable eddy generates satellite eddies, the material is exchanged between the central eddy and satellite eddies. This kind of eddies has spatial sizes ranging from submesoscales to mesoscales; thus the remote sensing technology with current resolution is enough to observe these eddies. In the future, I expect that remote sensing technology with higher resolution would capture more of this kind of eddies.

The oceanography community does not pay much attention to inertial waves, which have already been observed in various laboratory experiments and numerical experiments. The less attention is probably due to the very small amplitude of inertial waves, making them difficult be observed by current technology. However, one of the characteristics of inertial waves is that their frequency is always less than the local inertial frequency; that is, they contribute to the sub-inertial signals. Hence, if a series of signals recorded by moorings in the ocean contains sub-inertial frequencies, the inertial wave is a potential candidate to explain the sub-inertial signals.

Ocean internal waves below an upper mixed layer can produce dispersion in the mixed layer; however, if the mixed layer contains strong flows like currents and eddies, the dispersion produced by the below internal waves can be neglected, since the dispersion rate due to internal waves is much smaller than that produced by currents and eddies. On the other hand, if the mixed layer is relatively calm, the dispersion by internal waves needs to be counted.

In the end of this dissertation, I want to point out that the cylindrical domain with background rotation is a great model to explore geophysical fluid dynamics. In the literature, plenty of results on fluid dynamics are discovered using this model. I believe that more and more interesting geophysical fluid dynamics will be unveiled with the help from this model in the near future!

References

- Afanasyev, Y. D., Peltier, W. R., 1998. Three-dimensional instability of anticyclonic swirling flow in rotating fluid: laboratory experiments and related theoretical predictions. *Phys. Fluids* **10**(12), 3194–3202.
- Afanasyev, Y. D., Rhines, P. B., Lindahl, E. G., 2008. Emission of inertial waves by baroclinically unstable flows: laboratory experiments with altimetric imaging velocimetry. *J. Atmos. Sci.* **65**, 250–262.
- Aldridge, K. D., Lumb, L. I., 1987. Inertial waves identified in the Earth's fluid outer core. *Nature* **325**, 421–423.
- Aref, H., 1984. Stirring by chaotic advection. *J. Fluid Mech.* **143**, 1–21.
- Aref, H., Blake, J. R., Budisić, M., Cartwright, J. H., Clercx, H.J., Feudel, U., Golestanian, R., Gouillart, E., Le Guer, Y., van Heijst, G.F., Krasnopol'skaya, T.S., MacKay, R.S., Meleshko, V.V., Metcalfe, G., Mezić, I., de Moura, A.P.S., Omari, K.E., Piro, O., Speetjens, M.F.M., Sturman, R., Thiffeault, J.-L., Tuval, I., 2014. Frontiers of chaotic advection. *arXiv preprint arXiv:1403.2953 [nlin.CD]*.
- Artale, V., Boffetta, G., Celani, A., Cencini, M., Vulpiani, A., 1997. Dispersion of passive tracers in closed basins: beyond the diffusion coefficient. *Phys. Fluids*, **9**, 3162–3171.
- Aurell, E., Boffetta, G., Crisanti, A., Paladin, G., Vulpiani, A., 1997. Predictability in the large: an extension of the concept of Lyapunov exponent. *J. Physics A: Math. General*, **30**, 1–26.
- Babiano, A., Basdevant, C., Le Roy, P., Sadourny, R., 1990. Relative dispersion in two-dimensional turbulence. *J. Fluid Mech.*, **214**, 535–557.
- Baroud, C.N., Plapp, B.B., She, Z-S., Swinney, H.L., 2002. Anomalous self-similarity in a turbulent rapidly rotating fluid. *Phys. Rev. Lett.* **88**(11), 114501.
- Batchelor, G. K., 1950. The application of the similarity theory of turbulence to atmospheric diffusion. *Q. J. R. Meteor. Soc.*, **76**, 133–146.

- Benitez-Nelson, C.R., Bidigare, R.R., Dickey, T.D., Landry, M.R., Leonard, C.L., Brown, S.L., Nencioli, F., Rii, Y. M., Maiti, K., Becker, J.W., Bibby, T.S., Black, W., Cai, W., Carlson, C.A., Chen, F., Kuwahra, V.S., Mahaffey, C., McAndrew, P., Quay, P.D. Rappé, M.S., Selph, K. E., Simmons, M.P., Yang, E.J., 2007. Mesoscale eddies drive increased silica export in the subtropical Pacific Ocean. *Science* **316**, 1017–1021.
- Bennett, A. F., 1984. Relative dispersion: local and nonlocal dynamics. *J. Atmos. Sci.*, **41**, 1881–1886.
- Benney, D. J., 1977. A general theory for interactions between short and long waves. *Stud. Appl. Maths.* **56**, 81–94.
- Bershadskii, A., Kit, E., Tsinober, A., 1993. Spontaneous breaking of reflexional symmetry in real quasi-two-dimensional turbulence: stochastic travelling waves and helical solitons in atmosphere and laboratory. *Proc. R. Soc. Lond. A* **441**, 147–155.
- Billant, P., Gallaire, F., 2005. Generalized Rayleigh criterion for non-axisymmetric centrifugal instabilities. *J. Fluid Mech.* **542**, 365–379.
- Boffetta, G., Celani, A., Cencini, M., Lacorata, G., Vulpiani, A., 2000. Nonasymptotic properties of transport and mixing. *Chaos: An Interdisciplinary J. Non. Sci.*, **10**, 50–60.
- Boffetta, G., Ecke, R. E., 2012. Two-dimensional turbulence. *Annu. Rev. Fluid Mech.* **44**, 427–451.
- Boisson, J., Lamriben, C., Maas, L. R. M., Cortet, P., Moisy, F., 2012. Inertial waves and modes excited by the libration of a rotating cube. *Phys. Fluids* **24**, 076602.
- Bordes, G. Moisy, F., Dauxois, T., Cortet, P., 2012. Experimental evidence of a triadic resonance of plane inertial waves in a rotating fluid. *Phys. Fluids* **24**, 014105.
- Bouchut, F., Ribstein, B., Zeitlin, V., 2011. Inertial, barotropic, and baroclinic instabilities of the Bickley jet in two-layer rotating shallow water model. *Phys. Fluids* **23**, 126601.
- Bourlès, B., Andrié, C., Gouriou, Y., Eldin, G., Du Penhoat, Y., Freudenthal, S., Dewitte, B., Gallois, F., Chuchla, R., Baurand, F., Aman, A., Kouadio, G., 2003. The deep currents in the eastern equatorial Atlantic ocean. *Geophys. Res. Lett.* **30(5)**, 8002.
- Branicki, M., Kirwan Jr., A. D., 2010. Stirring: the Eckart paradigm revisited. *Int. J. Eng. Sci.* **48**, 1027–1042.

- Brissaud, A., Frisch, U., Leorat, J., Lesieur, M., Mazure, A., 1973. Helicity cascades in fully developed isotropic turbulence. *Phys. Fluids* **16**, 1366–1367.
- Bühler, O., McIntyre, M. E., 2005. Wave capture and wave-vortex duality. *J. Fluid Mech.* **534**, 67–95.
- Capet, X., McWilliams, J. C., Molemaker, M. J., Shchepetkin, A. F., 2008a. Mesoscale to submesoscale transition in the California current system. Part II: Frontal processes. *J. Phys. Oceanogr.* **38**, 44–64.
- Capet, X., McWilliams, J. C., Molemaker, M. J., Shchepetkin, A. F., 2008b. Mesoscale to submesoscale transition in the California current system. Part III: Energy balance and flux. *J. Phys. Oceanogr.* **38**, 2256–2269.
- Carnevale, G. F., Kloosterziel, R. C., 1994. Emergence and evolution of triangular vortices. *J. Fluid Mech.* **259**, 305–331.
- Carnevale, G. F., Kloosterziel, R. C., Orlandi, P., 2013. Inertial and barotropic instabilities of a free current in three-dimensional rotating flow. *J. Fluid Mech.* **725**, 117–151.
- Carton, X.J., Flierl, G.R., Polvani, L.M., 1989. The generation of tripoles from unstable axisymmetric isolated vortex structures. *Europhys. Lett.* **9**(4), 339 - 344.
- Carton, X.J., McWilliams, J.C., 1989. Barotropic and baroclinic instabilities of axisymmetric vortices in a quasigeostrophic model, in: Nihoul, J.C.J., Jamart, B.M. (Eds.), *Mesoscale/Synoptic Coherent Structures in Geophysical Turbulence*. Elsevier, pp.225–244.
- Chabreyrie, R., Llewellyn Smith, S. G., 2014. Short- and long-time transport structures in a three dimensional time dependent flow. *arXiv:1405.2022*.
- Chakrabortty, S., 2007. Signatures of two-dimensionalisation of 3D turbulence in the presence of rotation. *EPL* **79**(1), 14002.
- Chassignet, E. P., Hurlburt, H. E., Smedstad, O. M., Halliwell, G. R., Hogan, P. J., Wallcraft, A. J., Bleck, R., 2006. Ocean prediction with the hybrid coordinate ocean model (HYCOM). *Ocean Wea. Fore.* **5**, 413–426. Springer Netherlands.
- Chelton, D. B., Schlax, M. G., Samelson, R. M., De Szoeke, R. A., 2007. Global observations of large oceanic eddies. *Geophys. Res. Lett.* **34**, L15606.
- Chen, Y., Yau, M. K., 2001. Spiral bands in a simulated hurricane. Part I: vortex Rossby wave verification. *J. Atmos. Sci.* **58**, 2128–2145.
- Cortet, P., Lamriben, C., Moisy, F., 2010. Viscous spreading of an inertial wave beam in a rotating fluid. *Phys. Fluids* **22**, 086603.

- d'Orgeville, M., Hua, B. L., Schopp, R., Bunge, L., 2004. Extended deep equatorial layering as a possible imprint of inertial instability. *Geophys. Res. Lett.* **31**, L22303.
- Drazin, P. G., Reid, W. H., 2004. *Hydrodynamic Stability*, second ed. Cambridge University Press.
- Dunkerton, T. J., 1982. On the inertial stability of the equatorial middle atmosphere. *J. Atmos. Sci.* **38**, 2354–2364.
- Eldevik, T., Dysthe, K. B., 2002. Spiral eddies. *J. Phys. Oceano.* **32**, 851–869.
- Fischer, P. F., 1997. An overlapping Schwarz method for spectral element solution of the incompressible Navier-Stokes equations. *J. Comput. Phys.* **133**, 84–101.
- Fjørtoft, R., 1950. Application of integral theorems in deriving criteria of stability for laminar flows and for the baroclinic circular vortex. *Geof. Publ.* **17**(6), 5–52.
- Flierl, G.R., 1988. On the instability of geostrophic vortices. *J. Fluid Mech.* **197**, 349–388.
- Flór, J. B., van Heijst, G. J. F., 1996. Stable and unstable monopolar vortices in a stratified fluid. *J. Fluid Mech.* **311**, 257–287.
- Ford, R., 1994a. Gravity wave radiation from vortex trains in rotating shallow water. *J. Fluid Mech.* **281**, 81–118.
- Ford, R., 1994b. The response of a rotating ellipse of uniform potential vorticity to gravity wave radiation. *Phys. Fluids* **6**, 3694.
- Ford, R., McIntyre, M. E., Norton, W. A., 2000. Balance and the slow quasimaniifold: some explicit results. *J. Atmos. Sci.* **57**, 1236–1254.
- Ford, R., McIntyre, M. E., Norton, W. A., 2002. Reply. *J. Atmos. Sci.* **59**, 2878–2882.
- Fountain, G. O., Khakhar, D. V., Mezić, I., Ottino, J. M., 2000. Chaotic mixing in a bounded three-dimensional flow. *J. Fluid Mech.* **417**, 265–301.
- Fournier, J. D., Frisch, U., 1983. Remarks on the renormalization group in statistical fluid dynamics. *Phys. Rev. A* **28**(2), 1000–1002.
- Fultz, D., 1959. A note on overstability and the elastoid-inertia oscillations of Kelvin, Solberg, and Bjerknes. *J. Meteor.* **16**, 199–208.
- Gall, R., Tuttle, J., Hildebrand, P., 1998. Small-scale spiral bands observed in hurricanes Andrew, Hugo, and Erin. *Mon. Wea. Rev.* **126**, 1749–1766.

- Gallaire, F., Chomaz, J.M., 2003. Three-dimensional instability of isolated vortices. *Phys. Fluids* **15**, 2113–2126.
- Garrett, C., Munk, W., 1975. Space-time scales of internal waves: A progress report. *J. Geophys. Res.*, **80(3)**, 291–297.
- Gill, A. E., 1982. *Atmosphere-Ocean Dynamics*. Academic Press.
- Greenspan, H. P., 1969. *The Theory of Rotating Fluids*. Cambridge University Press.
- Griffiths, S. D., 2003a. Nonlinear vertical scale selection in equatorial inertial instability. *J. Atmos. Sci.* **60**, 977–990.
- Griffiths, S. D., 2003b. The nonlinear evolution of zonally symmetric equatorial inertial instability. *J. Fluid Mech.* **474**, 245–273.
- Griffiths, S. D., 2008. The limiting form of inertial instability in geophysical flows. *J. Fluid Mech.* **605**, 115–143.
- Griffiths, R. W., Killworth, P. D., Stern, M. E., 1982. Ageostrophic instability of ocean currents. *Journal of Fluid Mechanics*, **117**, 343C–377.
- Guinn, T. A., Schubert, W. H., 1993. Hurricane spiral bands. *J. Atmos. Sci.* **50**, 3380–3403.
- Gula, J., Plougonven, R., Zeitlin, V., 2009. Ageostrophic instabilities of fronts in a channel in a stratified rotating fluid. *J. Fluid Mech.* **627**, 485–507.
- Haller, G., 2001. Distinguished material surfaces and coherent structures in three-dimensional fluid flows. *Physica D* **149**, 248–277.
- Haller, G., Beron-Vera, F. J., 2013. Coherent Lagrangian vortices: the black holes of turbulence. *J. Fluid Mech.* **731**, R4.
- Haller, G., Yuan, G., 2000. Lagrangian coherent structures and mixing in two-dimensional turbulence. *Physica D* **147**, 352–370.
- Haza, A. C., Poje, A. C., Özgökmen, T. M., Martin, P., 2008. Relative dispersion from a high-resolution coastal model of the Adriatic Sea. *Ocean Model.*, **22**, 48–65.
- Hua, B. L., Moore, D. W., Le Gentil, S., 1997. Inertial nonlinear equilibration of equatorial flows. *J. Fluid Mech.* **331**, 345–371.
- Ivanov, A. Y., Ginzburg, A. I., 2002. Oceanic eddies in synthetic aperture radar images. *Proc. Indian Acad. Sci.* **111**, 281–295.
- Kelley, D. H., Triana, S. A., Zimmerman, D. S., Tilgner, A., Lathrop, D. P., 2007. Inertial waves driven by differential rotation in a planetary geometry. *Geophys. Astrophys. Fluid Dyn.* **101**, 469–487.

- Kelvin, L., 1880. Vibrations of a columnar vortex. *Phil. Mag.* **10**, 155–168.
- Klein, P., Lapeyre, G., 2009. The oceanic vertical pump induced by mesoscale and submesoscale turbulence. *Annu. Rev. Mar. Sci.* **1**, 351–375.
- Kloosterziel, R. C., Carnevale, G. F., 1999. On the evolution and saturation of instabilities of two-dimensional isolated circular vortices. *J. Fluid Mech.* **388**, 217–257.
- Kloosterziel, R. C., Carnevale, G. F., 2008. Vertical scale selection in inertial instability. *J. Fluid Mech.* **594**, 249–269.
- Kloosterziel, R. C., Carnevale, G. F., Orlandi, P., 2007. Inertial instability in rotating and stratified fluids: barotropic vortices. *J. Fluid Mech.* **583**, 379–412.
- Kloosterziel, R. C., Orlandi, P., Carnevale, G. F., 2007. Saturation of inertial instability in rotating planar shear flows. *J. Fluid Mech.* **583**, 413–422.
- Kloosterziel, R. C., van Heijst, G. J. F., 1991. An experimental study of unstable barotropic vortices in a rotating fluid. *J. Fluid Mech.* **223**, 1–24.
- Knox, J. A., McCann, D. W., Williams, P. D., 2008. Application of the Lighthill-Ford theory of spontaneous imbalance to clear-air turbulence forecasting. *J. Atmos. Sci.* **65**, 3292–3304.
- Kolmogorov, A. N., 1941. The local structure of turbulence in incompressible viscous fluid for very large Reynolds numbers. *Dokl. Akad. Nauk SSSR* **30**, 299–303.
- Kossin, J. P., Schubert, W. H., 2004. Mesovortices in Hurricane Isabel. *Bull. Amer. Meteor. Soc.* **85**, 151–153.
- Kraichnan, R. H., 1967. Inertial ranges in two-dimensional turbulence. *Phys. Fluids* **10**(7), 1417–1423.
- Kuo, H., 1949. Dynamic instability of two-dimensional non divergent flow in a barotropic atmosphere. *J. Meteor.* **6**, 105–122.
- Kuo, A. C., Polvani, L. M., 2000. Nonlinear geostrophic adjustment, cyclone/anticyclone asymmetry, and potential vorticity rearrangement. *Phys. Fluids* **12**(5), 1087–1100.
- Kurihara, Y., 1976. On the development of spiral bands in a tropical cyclone. *J. Atmos. Sci.* **33**, 940–958.
- LaCasce, J. H., 2008. Statistics from Lagrangian observations. *Prog. Oceanogr.* **77**, 1–29.
- LaCasce, J. H., Bower, A., 2000. Relative dispersion in the subsurface North Atlantic. *J. Mar. Res.*, **58**, 863–894.

- Lapeyre, G., Klein, P., 2006. Impact of the small-scale elongated filaments on the oceanic vertical pump. *J. Mar. Res.* **64**, 835–851.
- Large, W. G., McWilliams, J. C., Doney, S. C., 1994. Oceanic vertical mixing: a review and a model with a nonlocal boundary layer parameterization. *Rev. Geophys.* **32**(4), 363–403.
- Ledwell, J. R., McGillicuddy, D. J., Anderson, L. A., 2008. Nutrient flux into an intense deep chlorophyll layer in a mode-water eddy. *Deep-Sea Res. II* **55**, 1139–1160.
- Lesieur, M., Yanase, S., Métais, O., 1991. Stabilizing and destabilizing effects of a solid-body rotation on quasi-two-dimensional shear layers. *Phys. Fluids* **3**(3), 403–407.
- Lévy, M., Ferrari, R., Franks, P. J. S., Martin, A. P., Rivière, P., 2012. Bringing physics to life at the submesoscale. *Geophys. Res. Lett.* **39**, L14602.
- Lighthill, M. J., 1952. On sound generated aerodynamically. I. General theory. *Proc. R. Soc. Lond.* **211**, 564–587.
- Lima, I. D., Olson, D. B., Doney, S. C., 2002. Biological response to frontal dynamics and mesoscale variability in oligotrophic environments: biological production and community structure. *J. Geophys. Res.* **107**(C8), 3111.
- Lipphardt Jr., B. L., Poje, A. C., Kirwan Jr., A. D., Kantha, L., Zweng, M., 2008. Death of three Loop Current rings. *J. Mar. Res.* **66**, 25–60.
- Lopez, J. M., Marques, F., 2011. Instabilities and inertial waves generated in a librating cylinder. *J. Fluid Mech.* **687**, 171–193.
- Lumpkin, R., Elipot, S., 2010. Surface drifter pair spreading in the North Atlantic. *Journal of Geophysical Research: Oceans*, **115**, C12017.
- Maday, Y., Patera, A. T., Rønquist, E. M., 1990. An operator-integration-factor splitting method for time-dependent problems: application to incompressible fluid flow. *J. Sci. Comput.* **5**(4), 263–292.
- Mahadevan, A., D'Asaro, E., Lee, C., Perry, M. J., 2012. Eddy-driven stratification initiates north atlantic spring phytoplankton blooms. *Science* **337**, 54–58.
- Manasseh, R., 1992. Breakdown regimes of inertia waves in a precessing cylinder. *J. Fluid Mech.* **243**, 261–296.
- McEwan, A. D., 1970. Inertial oscillations in a rotating fluid cylinder. *J. Fluid Mech.* **40**, 603–640.

- McGillicuddy, D. J., Anderson, L. A., Bates, N. R., Bibby, T., Buesseler, K. O., Carlson, C. A., Davis, C. S., Ewart, C., Falkowski, P. G., Goldthwait, S. A., Hansell, D. A., Jenkins, W. J., Johnson, R., Kosnyrev, V. K., Ledwell, J. R., Li, Q. P., Siegel, D. A., Steinberg, D. K., 2007. Eddy/Wind interactions stimulate extraordinary mid-ocean plankton blooms. *Science* **316**, 1021–1026.
- McIntyre, M. E., 2009. Spontaneous imbalance and hybrid vortex-gravity structures. *J. Atmos. Sci.* **66**, 1315–1326.
- McWilliams, J. C., 1985. Submesoscale, coherent vortices in the ocean. *Rev. Geophys.*, **23**(2), 165–182.
- Melander, M. V., Zabusky, N. J., McWilliams, J. C., 1987. Axisymmetrization and vorticity-gradient intensification of an isolated two-dimensional vortex through filamentation. *J. Fluid Mech.* **178**, 137–159.
- Melander, M. V., McWilliams, J. C., Zabusky, N. J., 1988. Symmetric vortex merger in two dimensions: causes and conditions. *J. Fluid Mech.* **195**, 303–340.
- Mensa, J. A., Özgökmen, T. M., Poje, A. C., Imberger, J., 2015. Material transport in a convective surface mixed layer under weak wind forcing. *Ocean Model.*, **96**, 226–242.
- Messio, L., Morize, C., Rabaud, M., Moisy, F., 2008. Experimental observation using particle image velocimetry of inertial waves in a rotating fluid. *Exp. Fluids* **44**, 519–528.
- Mezić, I., 2001. Chaotic advection in bounded Navier-Stokes flows. *J. Fluid Mech.* **431**, 347–370.
- Michalke, A., Timme, A., 1967. On the inviscid instability of certain two-dimensional vortex-type flows. *J. Fluid Mech.* **29**(4), 647–666.
- Miller, P. D., Pratt, L. J., Helfrich, K. R., Jones, C. K., 2002. Chaotic transport of mass and potential vorticity for an island recirculation. *J. Phys. Oceanogr.*, **32**(1), 80C-102.
- Mininni, P. D., Pouquet, A., 2009. Helicity cascades in rotating turbulence. *Phys. Rev. E* **79**, 026304.
- Mizobata, K., Saitoh, S. I., Shiomoto, A., Miyamura, T., Shiga, N., Imai, K., Toratani, M., Kajiwara, Y., Sasaoka, K., 2002. Bering Sea cyclonic and anticyclonic eddies observed during summer 2000 and 2001. *Prog. Oceanogr.* **55**, 65–75.
- Molemaker, M. J., McWilliams, J. C., Yavneh, I., 2005. Baroclinic instability and loss of balance. *J. Phys. Oceanogr.* **35**, 1505–1517.

- Montgomery, M. T., Bell, M. M., Aberson, S. D., Black, M. L., 2006. Hurricane Isabel (2003): new insights into the physics of intense storms. Part I. *Bull. Amer. Meteor. Soc.* **87**, 1335–1347.
- Montgomery, M. T., Kallenbach, R. J., 1997. A theory for vortex Rossby-waves and its application to spiral bands and intensity changes in hurricanes. *Quart. J. Roy. Meteor. Soc.* **123**, 435–465.
- Moon, Y., Nolan, D. S., 2010. Do gravity waves transport angular momentum away from tropical cyclones? *J. Atmos. Sci.* **67**, 117–135.
- Munk, W., 1981. Internal waves and small-scale processes. *Evo. Phys. Oceanogr.*, 264–291.
- Munk, W., Armi, L., Fischer, K., Zachariasen, F., 2000. Spirals on the sea. *Proc. R. Soc. Lond. A* **456**, 1217–1280.
- Noir, J., Hemmerlin, F., Wicht, J., Baca, S. M., Aurnou, J. M., 2009. An experimental and numerical study of vibrationally driven flow in planetary cores and subsurface oceans. *Phys. Earth Planet. In.* **173**, 141–152.
- Nolan, D. S., Montgomery, M. T., 2000. The algebraic growth rate of wavenumber one disturbances in hurricane-like vortices. *J. Atmos. Sci.* **57**, 3514–3538.
- Nolan, D. S., Montgomery, M. T., 2001. The wavenumber-one instability and trochoidal motion of hurricane-like vortices. *J. Atmos. Sci.* **58**, 3234–3270.
- Ohlmann, J. C., LaCasce, J. H., Washburn, L., Mariano, A. J., Emery, B., 2012. Relative dispersion observations and trajectory modeling in the Santa Barbara Channel. *J. Geophys. Res.* **117**, C05040.
- Orlandi, P., Carnevale, G. F., 1999. Evolution of isolated vortices in a rotating fluid of finite depth. *J. Fluid Mech.* **381**, 239–269.
- Orlandi, P., van Heijst, G. F., 1992. Numerical simulation of tripolar vortices in 2D flow. *Fluid Dyn. Res.* **9**, 179–206.
- O’Sullivan, D., Dunkerton, T. J., 1995. Generation of inertia-gravity waves in a simulated life cycle of baroclinic instability. *J. Atmos. Sci.* **52**, 3695–3716.
- Ottino, J. M., 1989. *The Kinematics of Mixing: Stretching, Chaos and Transport*. Cambridge University Press.
- Özgökmen, T. M., Iliescu, T., Fischer, P.F., Srinivasan, A., Duan J., 2007. Large eddy simulation of stratified mixing in two-dimensional dam-break problem in a rectangular enclosed domain. *Ocean Model.* **16**, 106–140.

- Özgökmen, T. M., Poje, A. C., Fischer, P. F., Haza, A.C., 2011. Large eddy simulations of mixed layer instabilities and sampling strategies. *Ocean Model.* **39**, 311–331.
- Özgökmen, T. M., Poje, A. C., Fischer, P. F., Childs, H., Krishnan, H., Garth, C., Haza, A. C., Ryan, E., 2012. On multi-scale dispersion under the influence of surface mixed layer instabilities and deep flows. *Ocean Model.* **56**, 16–30.
- Patera, A. T., 1984. A spectral element method for fluid dynamics: laminar flow in a channel expansion. *J. Comput. Phys.* **54**, 468–488.
- Pedlosky, J., 1987. *Geophysical Fluid Dynamics*. 2nd ed. Springer-Verlag.
- Pingree, R. D., Le Cann, B., 1992. Anticyclonic Eddy X91 in the southern Bay of Biscay, May 1991 to Febuary 1992. *J. Geophys. Res.* **97**, 14353–14367.
- Plougonven, R., Muraki, D. J., Snyder, C., 2005. A baroclinic instability that couples balanced motions and gravity waves. *J. Atmos. Sci.* **62**, 1545–1559.
- Plougonven, R., Zhang, F., 2014. Internal gravity waves from atmospheric jets and fronts. *Rev. Geophys.* **52**, 33–76.
- Pratt, L. J., Helfrich, K. R., Leen, D., 2008. On the stability of ocean overflows. *J. Fluid Mech.*, **602**, 241C-266.
- Pratt, L. J., Rypina, I. I., Özgökmen, T. M., Wang, P., Childs, H., Bebieva, Y., 2013. Chaotic advection in a steady, three-dimensional, Ekman-driven eddy. *J. Fluid Mech.* **738**, 143–183.
- Rayleigh, L., 1880. On the stability, or instability, of certain fluid motions. *Proc. London Math. Soc.* **11**, 57–70.
- Rayleigh, L., 1917. On the dynamics of revolving fluids. *Proc. R. Soc. Lond. A* **93**, 148–154.
- Reasor, P. D., Montogmery, M. T., Marks Jr., F. D., Gamache, J. F., 2000. Low-wavenumber structure and evolution of the hurricane inner core observed by airborne dual-doppler radar. *Mon. Wea. Rev.* **128**, 1653–1680.
- Ribstein, B., Plougonven, R., Zeitlin, V., 2014. Inertial versus baroclinic instability of the Bickley jet in continuously stratified rotating fluid. *J. Fluid Mech.* **743**, 1–31.
- Richards, K., Banks, H., 2002. Characteristics of interleaving in the western equatorial Pacific. *J. Geophys. Res.* **107**(C12), 3231.
- Richards, K. J., Edwards, N. R., 2003. Lateral mixing in the equatorial Pacific: the importance of inertial instability. *Geophys. Res. Lett.* **30**(17), 1888.

- Richardson, L. F., 1926. Atmospheric diffusion shown on a distance-neighbor graph. *Proc. Roy. Soc. Lond.*, **110**, 709–737.
- Rogerson, A. M., Miller, P. D., Pratt, L. J., Jones, C. K. R. T., 1999. Lagrangian Motion and Fluid Exchange in a Barotropic Meandering Jet. *J. Phys. Oceanogr.*, **29(10)**, 2635–2655.
- Rossby, C. G., 1938. On the mutual adjustment of pressure and velocity distributions in certain simple current systems, II. *J. Mar. Res.* **2**, 239–263.
- Rypina, I. I., Llopiz, J. K. Pratt, L. J., Lozier, M. S., 2014. Dispersal pathways of American eel larvae from the Sargasso Sea. *Limnol. Oceanogr.* **59(5)**, 1704–1714.
- Rypina, I. I., Pratt, L. J., Wang, P., Özgökmen, T. M., Mezić, I., 2015. Resonance phenomena in a time-dependent, three-dimensional model of an idealized eddy. *Chaos: An Interdisciplinary J. Non. Sci.* **25**, 087401.
- Samelson, R., Wiggins, S., 2006. *Lagrangian Transport in Geophysical Jets and Waves*. Springer New York.
- Schecter, D. A., 2008. The spontaneous imbalance of an atmospheric vortex at high Rossby number,” *J. Atmos. Sci.* **65**, 2498–2521.
- Schecter, D. A., Montgomery, M. T., 2004. Damping and pumping of a vortex Rossby wave in a monotonic cyclone: Critical layer stirring versus inertia-buoyancy wave emission. *Phys. Fluids* **16**, 1334.
- Schecter, D. A., Montgomery, M. T., 2006. Conditions that inhibit the spontaneous radiation of spiral inertia-gravity waves from an intense mesoscale cyclone. *J. Atmos. Sci.* **63**, 435–456.
- Schroeder, K., Haza, A. C., Griffa, A., Özgökmen, T. M., Poulain, P. M., Gerin, R., Rixen, M., 2011. Relative dispersion in the Liguro-Proven04al basin: From sub-mesoscale to mesoscale. *Deep Sea Research Part I: Oceanographic Research Papers*, **58(3)**, 209–228.
- Schubert, W. H., Montgomery, T., Taft, R. K., Guinn, T. A., Fulton, S. R., Kossin, J. P., Edwards, J. P., 1999. Polygonal eyewalls, asymmetric eye contraction, and potential vorticity mixing in hurricanes. *J. Atmos. Sci.* **56**, 1197–1223.
- Shadden, S. C., Lekien, F., Marsden, J. E., 2005. Definition and properties of Lagrangian coherent structures form finite-time Lyapunov exponents in two-dimensional aperiodic flows. *Physica D* **212**, 271–304.
- Shcherbina, A. Y., D’Asaro, E. A., Lee, C. M., Klymak, J. M., Molemaker, M. J., McWilliams, J. C., 2013. Statistics of vertical velocity, divergence, and strain in a developed submesoscale turbulence field. *Geophys. Res. Lett.* **40**, 4706–4711.

- Shen, C. Y., Evans, T. E., 2002. Inertial instability and sea spirals. *Geophys. Res. Lett.* **29**, 2124.
- Siegel, D. A., Peterson, P., McGillicuddy, D. J., Maritorena, S., Nelson, N. B., 2011. Bio-optical footprints created by mesoscale eddies in the sargasso sea. *Geophys. Res. Lett.* **38**, L13608.
- Small, R. J., Deszoeke, S. P., Xie, S. P., O'Neill, L., Seo, H., Song, Q., Cornillon, P., Spall, M., Minobe, S., 2008. Air-sea interaction over ocean fronts and eddies. *Dyn. Atmos. Oceans* **45**, 274–319.
- Smith, R. A., Rosenbluth, M. N., 1990. Algebraic instability of hollow electron columns and cylindrical vortices. *Phys. Rev. Lett.* **64**(6), 649–652.
- Smith, L. M., Woodruff, S. L., 1998. Renormalization-group analysis of turbulence. *Annu. Rev. Fluid Mech.* **30**, 275–310.
- Smyth, W. D., McWilliams, J. C., 1998. Instability of an axisymmetric vortex in a stably stratified, rotating environment. *Theoret. Comput. Fluid Dyn.* **11**, 305–332.
- Snyder, C., Muraki, D. J., Plougonven, R., Zhang, F., 2007. Inertia-gravity waves generated within a dipole vortex. *J. Atmos. Sci.* **64**, 4417–4431.
- Snyder, C., Plougonven, R., Muraki, D. J., 2009. Mechanisms for spontaneous gravity wave generation within a dipole vortex. *J. Atmos. Sci.* **66**, 3464–3478.
- Stapleton, N. R., Aicken, W. T., Dovey, P. R., Scott, J. C., 2002. The use radar altimeter data in combination with other satellite sensors for routine monitoring of the ocean: case study of the northern Arabian Sea and Gulf of Oman. *Can. J. Remote Sensing* **28**(4), 567–572.
- Strass, V. H., 1992. Chlorophyll patchiness caused by mesoscale upwelling at fronts. *Deep-Sea Res.* **39**, 75–96.
- Sturman, R., Ottino, J. M., Wiggins, S., 2006. *The Mathematical Foundations of Mixing: The Linked Twist Map as a Paradigm in Applications: Micro to Macro, Fluids to Solids*. Cambridge University Press.
- Sugimoto, N., Ishii, K., 2012. Spontaneous gravity wave radiation in a shallow water system on a rotating sphere. *J. Meteor. Soc. Japan* **90**(1), 101–125.
- Sugimoto, N., Ishioka, K., Kobayashi, H., Shimomura, Y., 2015. Cyclone-anticyclone asymmetry in gravity wave radiation from a co-rotating vortex pair in rotating shallow water. *J. Fluid Mech.* **722**, 80–106.
- Sugimoto, N., Ishioka, K., Ishii, K., 2008. Parameter sweep experiments on spontaneous gravity wave radiation form unsteady rotational flow in an f-plane shallow water system. *J. Atmos. Sci.* **65**, 235–249.

- Sugimoto, N., Ishioka, K., Yoden, S., 2007. Gravity wave radiation from unsteady rotational flow in an f-plane shallow water system. *Fluid Dyn. Res.* **39**, 731–754.
- Sun, H., Kunze, E., 1999. Internal wave-wave interactions. Part I: The role of internal wave vertical divergence. *Journal of physical oceanography*, **29(11)**, 2886–2904.
- Synge, J. L., 1933. The stability of heterogeneous liquids. *Trans. Roy. Soc. Can.* **27(3)**, 1–18.
- Terwey, W. D., Montgomery, M. T., 2002. Wavenumber-2 and wavenumber-m vortex Rossby wave instabilities in a generalized three-region model. *J. Atoms. Sci.* **59**, 2421–2427.
- Tilgner, A., 2007. Zonal wind driven by inertial modes. *Phys. Rev. Lett.* **99**, 194501.
- Vallis, G. K., 2006. *Atmospheric and Oceanic Fluid Dynamics*. Cambridge University Press.
- van de Konijnengerg, J. A., Nielsen, A. H., Rasmussen, J. J., Stenum, B., 1999. Shear-flow instability in a rotating fluid. *J. Fluid Mech.* **387**, 177–204.
- van Sebille, E., Waterman, S., Barthel, A., Lumpkin, R., Keating, S. R., Fogwill, C., Turney, C., 2015. Pairwise surface drifter separation in the western Pacific sector of the Southern Ocean. *Journal of Geophysical Research: Oceans*, **120**, 6769–6781.
- Vanneste, J., Yavneh, I., 2004. Exponentially small inertia-gravity waves and the breakdown of quasigeostrophic balance. *J. Atmos. Sci.* **61**, 211–223.
- Vanneste, J., 2013. Balance and spontaneous wave generation in geophysical flows. *Annu. Rev. Fluid Mech.* **45**, 147–172.
- Viebahn, J., Eden, C., 2010. Towards the impact of eddies on the response of the Southern Ocean to climate change. *Ocean Modell.* **34**, 150–165.
- Viúdez, Á., 2006. Spiral patterns of inertia-gravity waves in geophysical flows. *J. Fluid Mech.* **562**, 73–82.
- Viúdez, Á., 2007. The origin of the stationary frontal wave packet spontaneously generated in rotating stratified vortex dipoles. *J. Fluid Mech.* **593**, 359–383.
- Viúdez, Á., 2008. The stationary frontal wave packet spontaneously generated in mesoscale dipoles. *J. Phys. Oceano.* **38**, 243–256.
- Wang, S., Zhang, F., Snyder, C., 2009. Generation and propagation of inertia-gravity waves from vortex dipoles and jets. *J. Atmos. Sci.* **66**, 1294–1314.
- Wang, S., Zhang, F., 2010. Source of gravity waves within a vortex-dipole jet revealed by a linear model. *J. Atmos. Sci.* **67**, 1438–1455.

- Wang, P., Özgökmen, T. M., 2015. How do hydrodynamic instabilities affect 3D transport in geophysical vortices? *Ocean Model.* **87**, 48–66.
- Wang, P., Özgökmen, T.M., 2016. Spiral inertial waves emitted from geophysical vortices. *Ocean Model.*, **99**, 22–42.
- Wiggins, S., 2005. The dynamical systems approach to Lagrangian transport in oceanic flows. *Annu. Rev. Fluid Mech.* **37**, 295–328.
- Williams, P. D., Haine, T. W. N., Read, P. L., 2005. On the generation mechanisms of short-scale unbalanced modes in rotating two-layer flows with vertical shear. *J. Fluid Mech.* **528**, 1–22.
- Williams, P. D., Haine, T. W. N., Read, P. L., 2008. Inertia-gravity waves emitted from balanced flow: observations, properties, consequences. *J. Atmos. Sci.* **65**, 3543–3556.
- Willoughby, H. E., 1978. A possible mechanism for the formation of hurricane rainbands. *J. Atmos. Sci.* **35**, 838–848.
- Yakhot, V., Orszag, S. A., 1986. Renormalization group analysis of turbulence. I. Basic theory. *J. Sci. Comput.* **1**, 3–51.
- Zhang, F., Koch, S. E., Davis, C. A., Kaplan, M. L., 2000. A survey of unbalanced flow diagnostics and their application. *Adv. Atmos. Sci.* **17**, 165–183.
- Zhang, F., Koch, S. E., Davis, C. A., Kaplan, M. L., 2001. Wavelet analysis and the governing dynamics of a large-amplitude mesoscale gravity-wave event along the East Coast of the United States. *Quart. J. Roy. Meteor. Soc.* **127**, 2209–2245.
- Zhang, F., 2004. Generation of mesoscale gravity waves in upper-tropospheric jet-front systems. *J. Atmos. Sci.* **61**, 440–457.